Error-robust quantum signal processing using Rydberg atoms

Sina Zeytinoğlu*
Physics and Informatics Laboratory, NTT Research, Inc., Sunnyvale, California 94085, USA and Department of Physics, Harvard University, Cambridge, Massachusetts 02138, USA

Sho Sugiura
Physics and Informatics Laboratory, NTT Research, Inc., Sunnyvale, California 94085, USA and Laboratory for Nuclear Science, Massachusetts Institute of Technology, Cambridge, Massachusetts 02139, USA

(Received 3 December 2022; accepted 15 November 2023; published 3 January 2024)

Rydberg atom arrays have recently emerged as one of the most promising platforms for quantum simulation and quantum information processing. However, as is the case for other experimental platforms, the longer-term success of the Rydberg atom arrays in implementing quantum algorithms depends crucially on their robustness to gate-induced errors. Here we show that, for an idealized biased-error model based on Rydberg atom dynamics, the implementation of quantum signal processing (QSP) protocols can be made error robust, in the sense that the asymptotic scaling of the gate-induced error probability is slower than that of gate complexity. Moreover, our numerical results that use experimentally accessible parameters indicate that QSP iterates made out of more than 100 gates can be implemented with constant error probability. To showcase our approach, we provide a concrete blueprint to implement QSP-based near-optimal Hamiltonian simulation on the Rydberg atom platform. The proposed protocol substantially improves both the scaling and the overhead of gate-induced errors in comparison to those protocols that implement a fourth-order product formula.

DOI: 10.1103/PhysRevResearch.6.013003

I. INTRODUCTION

Neutral atoms have become a leading experimental platform for accomplishing useful quantum information processing tasks [1–9], as well as emulating a variety of nontrivial Hamiltonian dynamics [10] and correlated states [11–15]. In this success, the rich physics of neutral atoms has played an essential role. On the one hand, the tightly confined hyperfine states of the atoms interact very weakly with the environment [7], making these states ideal for storing quantum information [16–19]. On the other hand, the extended Rydberg states enable strong interactions between the atoms [20], allowing fast and high-fidelity multiqubit gates to be realized [1,3,21]. Moreover, the advances in trapping and manipulating alkali-earth atoms resulted in drastic improvements in the error characteristics of the one- and two-qubit gates on the neutral atom platform [22–24], making it an important contender to other leading platforms based on trapped ions [25,26] and circuit quantum electrodynamics [27,28]. A distinctive advantage of neutral atoms compared to the other platforms is that they can be trapped close to one another, resulting in a scalable and dynamically reconfigurable [7,29] architecture. Similarly, the rich internal structure of neutral atoms results in a uniquely versatile setup where both the unitary and dissipative dynamics of the system can be tailored for the specific quantum information task at hand [23,24,30–32].

Yet, as is the case with all current experimental platforms for realizing quantum computation, Rydberg atoms cannot be controlled without inducing significant unwanted dynamics. Consequently, the protocols implemented for processing quantum information involve errors and the resulting computation is unreliable [33–35]. While fault-tolerant error-corrected quantum computation is in principle possible [36–38], the resources necessary for reaching the error-correction threshold with the error rates achieved in current experiments is daunting [39], despite promising developments [32]. A direct way to reduce this resource cost is to increase the robustness of the system against errors [39]. Therefore, whether the rich physics of the Rydberg atoms can be leveraged to realize error-robust implementations of a broad class of algorithms is crucial for the success of the platform.

The term error robust has been used colloquially in the optimal control theory literature [40–42]. However, here we use *error-robust* implementations of quantum algorithms as a narrower and more powerful notion. By error-robust implementations, we mean that the error probability associated with the implementation of an algorithm scales slower than the gate complexity of the corresponding circuit. Our first contribution is a tool set to effectively demonstrate whether a proposed implementation is indeed error robust. Specifically, we introduce a definition of gate-induced error probability that is dependent on the properties of the input quantum state, in

*sina_zeytinoglu@fas.harvard.edu

contrast to conventional definitions based on average or worst-case error probability [43,44]. This *input-conditional* error probability, unlike its conventional counterparts, allows the total error probability associated with an implementation of a quantum algorithm to scale slower than the gate complexity of the corresponding circuit.

As our main contribution, we utilize the mathematical properties of the input-conditional error probability together with the physical properties of the Rydberg atom platform to design error-robust implementations of a wide range of quantum algorithms. Specifically, we design error-robust implementations of algorithms that can be expressed in an iterative manner using quantum signal processing (QSP) [45,46], a framework which unifies Hamiltonian simulation, unstructured search, as well as phase estimation [47]. We demonstrate that, assuming an idealized incoherent error model based on the physics of Rydberg atoms, each iterate of a QSP protocol can be implemented with constant error probability with respect to the gate complexity of the corresponding circuit. Moreover, we show that in an experimentally accessible parameter regime [12,48], it is possible to realize a more than 100-fold reduction of the error probability. Finally, we demonstrate that the error probability associated with a QSP-based error-robust implementation of the Hamiltonian simulation algorithm is more than an order of magnitude smaller than that of a state-of-the-art product-formula implementation, in the case of the one-dimensional disordered Heisenberg model [49,50]. Our work is primarily concerned with incoherent error processes, which are dominant in the current Rydberg atom platform [48,51,52] and leaves the investigation of the interplay between coherent errors and QSP protocols for future studies.

Our approach consists of two steps. First, we identify an incoherent error model which allows one to implement each QSP iterate, given by the linear combinations of unitaries (LCU) [53], with only constant input-conditional error probability. The main assumption of this error model is that multiqubit controlled unitaries can be implemented with perfectly *error biased* so that no errors occur when the control condition is not satisfied (i.e., the control qubit occupies a state that results in the trivial evolution of the target qubits). While such an error model is conceptually interesting, it can only serve as a guideline for designing error-robust implementations of quantum algorithms because it is unlikely to be valid for error processes in real quantum systems. Hence, as the second step of our approach, we design Rydberg atom implementations of strongly error-biased single-qubit controlled unitaries and show that they can be used for error-robust implementations of QSP iterates. In doing so, we utilize the rich physics offered by the Rydberg atom platform, including multiple Rydberg and hyperfine states, long-range Rydberg blockade interactions, and electromagnetically induced transparency (EIT). We emphasize that although this work focuses on the Rydberg platform, the strategies developed in this work are likely applicable to the broader range of physical platforms for quantum information processing and pave the way to improvements in the capabilities of quantum devices in the near future.

The paper is organized as follows. We provide a summary of the main results and insights in Sec. II. We begin the main text with the introduction to the input-conditional error probability in Sec. II B, and discuss how our method takes into account incoherent error processes, including those resulting in correlated errors. In Sec. IV, we introduce QSP based on a block-encoding unitary [54] implemented with LCU [53]. We also show that the structure of the LCU protocol can be leveraged to drastically reduce the effects of errors with error-biased controlled unitaries. In Sec. V, we design Rydberg atom gates that have strongly biased-error characteristics. We then provide concrete error-robust implementations of QSP protocols on the Rydberg atom platform in Sec. VI. We showcase our approach in Sec. VII by benchmarking the error bound of QSP-based Hamiltonian simulation against two other state-of-the-art Hamiltonian simulation algorithms. We conclude with a discussion of our results and provide an outlook for error-robust implementations using Rydberg atoms in Sec. VIII.

II. MAIN RESULTS AND IDEAS

The main object of study of our work is the error probability associated with implementations of quantum algorithms. We demonstrate that it is possible to study the interplay between the error mechanisms and the circuit that implements the quantum algorithm using an error measure that depends on the input state. We refer to such an error measure as input-conditional error probability.

We consider error-robust implementations that arise from the aforementioned interplay on two levels of abstraction. At the higher level, we show that if any concrete experimental platform provides perfectly error-biased multiqubit controlled unitaries, then it is suitable for the error-robust implementation of a wide range of QSP protocols. Then, we take this observation as a guiding principle to design concrete and detailed error-robust implementations of QSP protocols on the Rydberg atom platform. In particular, we design Rydberg atom gates which are strongly error biased in an experimentally feasible parameter regime and construct a circuit which results in an error-robust implementation of a QSP protocol. In the rest of the section, we provide an informal discussion of the main insights and results pertaining to each level.

A. Input-conditional error probability

The conventional approach to determining the upper bound for the error probability associated with an implementation of a generic quantum algorithm is to specify a universal gate set and count the number of gates required for the implementation. However, this approach does not have the flexibility to utilize any prior knowledge of the structure of the implementation, as it is based on the average or the worst-case error probability of each gate that makes up the algorithm [39,44]. In this work, we show that when partial knowledge of the implementation is available, the upper bound on the total error probability resulting from this conventional approach can be extremely loose, even when we restrict ourselves to only incoherent error processes. To demonstrate this point, we use a definition of error probability that is conditional on the input state of each gate. Moreover, we show that the definition of such an input-conditional error probability fulfills

important desiderata including the existence of a clear physical interpretation and an algorithm for efficient numerical computation [44]. Surprisingly, for certain implementations, the upper bound of the total input-conditional error probability can in principle scale much slower than the gate complexity for a wide range of algorithms. Here, we refer to such implementations as error-robust implementations.

B. Error-robust implementations of quantum signal processing

A great variety of quantum protocols are described as functional transforms $f(A)$ of high-dimensional linear operators A. The well-known examples include Hamiltonian simulation, where $f(H) = e^{-iHt}$ [55] and HHL algorithm for solving linear equations, where $f(A) = A^+$ with $+$ denoting the Moore-Penrose pseudoinverse [56].[1] The naive *expectation* is that the compilation of such algorithms is simple when $f(\cdot)$ and the input A have simple classical descriptions.

Quantum signal processing (QSP) is an *iterative* compilation method that formally fulfills this naive expectation when $f(\cdot)$ is approximated by a low-order polynomial, and A is sparse or approximated by a linear combination of a small number of Pauli strings.[2] Each iteration step of the QSP protocol has two components, called the block-encoding walk operator W_A [54], which encodes the linear operator A (i.e., there exists a projector Π such that $\Pi W_A \Pi = A$), and the processing unitary [45] which encodes a single rotation angle ϕ_i. For a QSP protocol that terminates after l iterations, a list of $l+1$ angles $\{\phi_i\}$ determines the lth-order polynomial approximation of the functional transform $f(\cdot)$. Importantly, in many instances, the QSP protocols were shown to be near optimal in terms of the number of iterations [57–59].

The QSP protocols can be simplified drastically when the controlled version of W_A (denoted $\mathrm{C}W_A$) is available. Then, the processing unitary is a single-qubit rotation of the control qubit. This is an important simplification from the perspective of error-robust implementations since the single-qubit rotation only contributes a constant to the error probability *per* iteration. Consequently, the scaling of the error probability associated with each iteration step of the QSP protocol is the same as the scaling of errors for $\mathrm{C}W_A$. *Given that many QSP protocols are optimal in the number of iterations, whether we can achieve an error-robust implementation of the QSP protocol hinges on an error-robust implementation of* $\mathrm{C}W_A$.

We find that the linear combination of unitaries (LCU) method [46,58] is an especially well-suited compilation method for an error-robust implementation of W_A and $\mathrm{C}W_A$. To implement the LCU protocol, A is decomposed as a linear combination of N unitary Pauli strings $\{P_i\}$, with the associated coefficients $\{\alpha_i\}$. Then the *classical data*, consisting of $\{\alpha_i\}$ and $\{P_i\}$, are encoded by two separate unitaries V and $\bar{U}$, which describe the *evolution of the quantum* system. On the one hand, the state preparation unitary V acts on an ancillary register of size n_a to prepare an amplitude encoding state $V|0\rangle^{\otimes n_a} = \sum_i^N \alpha_i |x_i\rangle$ for the coefficients $\{\alpha_i\}$. On the other hand, $\bar{U}$ takes the different components $\{|x_i\rangle\}$ of the ancillary state as *control conditions* for applying $\{P_i\}$ to the system register. Formally, $\bar{U}$ can be expressed as a product of controlled Pauli operations $\bar{U} \equiv \prod_i^N C_{x_i} P_i$. The walk operator is given by $W_A \equiv (2\Pi_0 - \mathbf{I}) V^\dagger \bar{U} V$, where $\Pi_0 = (|0\rangle\langle 0|)^{\otimes n_a} \otimes \mathbf{I}_{\mathrm{sys}}$ [58]. In this work, we assume that the control conditions $\{|x_i\rangle\}$ are bit strings in the computational bases.

We show that the following condition is sufficient for a near-constant input-conditional error probability implementation of W_A and its controlled version:

Condition 1: The required controlled unitaries are implemented in a way that the errors are induced only when the control condition is satisfied.

Although the implementation of $\mathrm{C}W_A$ with constant error probability is conceptually interesting, it is extremely unlikely that any physical system satisfies Condition 1, especially for large n_a. Instead, Condition 1 is a guideline for the Rydberg atom gates we design for error-robust implementations of QSP protocols. We call controlled unitary implementations that approximately satisfy Condition 1 *error-biased* unitaries. Error-biased unitaries are characterized by an error-bias parameter η_ϵ which is the ratio of the error probability when the control condition is not satisfied to that when it is satisfied. We call a unitary *perfectly error biased* when $\eta_\epsilon = 0$. In the following two subsections, we give a summary of the main ideas behind the proposed Rydberg atom gates which approximately satisfy Condition 1 for single-qubit controlled unitaries. In the implementation of $\bar{U}$ the unitaries that act on the target register are multiqubit Pauli operations, while for the state preparation unitary V, we utilize an efficient multiqubit unitary which takes advantage of the long-range interactions between the Rydberg atoms. In addition, we show that perfectly error-biased single-qubit controlled unitaries can be used to design an error-robust implementation of W_A when applied in a particular order.

Finally, the single-qubit controlled unitary $\mathrm{C}W_A$ can be implemented while retaining the near-constant error probability if the following condition is satisfied:

Condition 2: The system consists of subsystems 2 additional long-lived auxiliary states.

Note that the neutral atoms already satisfy Condition 2 as they have multiple long-lived hyperfine states. In the following, we denote the walk operator as W and drop the subscript for simplicity.

C. Designing error-biased Rydberg atom gates

We show that a single-qubit-controlled unitary that was proposed in Ref. [60] has strongly biased-error characteristics. The gate uses the Rydberg-blockade effect in combination with electromagnetically induced transparency (EIT) [61,62], and leverages the rich internal structure of the Rydberg atoms. While the gate was proposed more than a decade ago our work emphasizes its biased-error characteristics and use it to achieve error-robust implementations of quantum algorithms.

We demonstrate that the single-qubit controlled gate introduced in Ref. [60] drastically reduces the error-bias parameter η_ϵ by lowering the probability of errors in both the *control* and *target* registers when the control condition is not satisfied. On

[1] See Refs. [46,47] for further examples.

[2] In contrast, compiling time-dependent Hamiltonian simulation is difficult because then multiple functional transformations $f_t(\cdot)$ and their inputs A_t need to be explicitly specified.

the one hand, the probability of errors in the control register is reduced when the control condition is not satisfied because the EIT-based gate protocol starts by exciting the control atom to the Rydberg state only if it is in the $|0_c\rangle$ state. During this step, for low enough drive powers, the control atom in state $|1_c\rangle$ evolves almost trivially and the evolution results in negligible errors. As a result, the error probability due to the *control* atom is negligible when the control condition is not satisfied. On the other hand, the error probability resulting from the dynamics of the *target* atom is reduced when the control condition is not satisfied, thanks to the EIT mechanism. In particular, when the control atom is not excited to the Rydberg state, the EIT mechanism ensures that the laser field that couples the hyperfine states to shorter-lived excited states is not absorbed (hence the name "transparency"). Consequently, when the control condition is not satisfied, the evolution of the target atoms is also nearly trivial. In contrast, when the control condition *is* satisfied, the Rydberg excitation of the control atom disturbs the EIT mechanism, and the target qubit goes under a nontrivial and error-inducing evolution. We use the decay rates of experimentally accessible Rydberg levels to numerically calculate $\eta_\epsilon < \frac{1}{150}$ even when the error probability conditional on the control condition being satisfied is only 1% and the dipolar interaction strength is a few tens of MHz. Our results should be considered as a first demonstration of strongly error-biased controlled unitaries on a physical platform. Reducing η_ϵ further in any platform increases the platform's potential for error-robust implementations of QSP protocols.

Unfortunately, the single-qubit controlled unitaries discussed above do not have a straightforward generalization to error-robust multiqubit controlled unitaries. However, we demonstrate that an efficient and error-robust implementation of $\bar{U}$ is still possible with only single-qubit controlled unitaries if we use an appropriate choice of the control conditions $|x_i\rangle$ together with a particular order with which the single-qubit controlled unitaries are applied. Incidentally, the choice of control conditions $|x_i\rangle$ has the additional advantage of allowing for an error-robust implementation of the state preparation unitary V, as we discuss in the next subsection.

D. Designing the ancillary control register for error-robust implementations

Central to our design of the ancillary control register for error-robust implementations of QSP protocol is a multiqubit Rydberg blockage gate, referred to as the one-hot amplitude-encoding gate, or V_{1HE}. V_{1HE} prepares one-hot amplitude encoding states which are superpositions of bit strings where all but one of the qubits is in the zero logical state.

We consider the preparation of a tensor product of k one-hot encoding address states where each register is of size n_j with $j = (1, \ldots, k)$. We show that such a state can be prepared using $\prod_{j=1}^{k-1} n_j$ EIT-based single-qubit controlled V_{1HE} (denoted $\mathrm{C}V_{\mathrm{1HE}}$) gates, with a total input-conditional error probability of $O(k)$, assuming that Condition 1 is perfectly satisfied. Moreover, given the tensor product of k one-hot encoding states as the input state of the ancillary control register, the associated $\bar{U}$ consisting of $\prod_{j-1}^{k} n_j$ control conditions can be implemented with an input-conditional error probability of $O(k)$.

We emphasize that the tensor product of k one-hot encoding states allows us to encode N amplitudes in a small ancillary register of size $O(kN^{1/k})$. While the size of the ancillary register does not satisfy the theoretical lower bound $\Omega(\log N)$, given a system register of n_{site} atoms, as many as n_{site}^k control conditions can be stored in an ancillary register of size only $O(kn_{\mathrm{site}})$.

The implementation of $\mathrm{C}V_{\mathrm{1HE}}$ gates fully utilizes the rich physics of the Rydberg atoms, including the long-range dipolar interactions, availability of Rydberg states with different symmetries, as well as EIT. Our results thus highlight the importance of concrete physical processes for realizing error-robust implementations.

E. Proposal for Hamiltonian simulation

Finally, we showcase our approach in the context of Hamiltonian simulation algorithms. The first interesting observation is that given that conditions 1 and 2 are perfectly satisfied, the scaling of the input-conditional error probability for the QSP-based Hamiltonian simulation is the same as the optimal gate complexity, given by the simulated space-time volume [50,63]. We emphasize that this is despite the fact that the number of gates required to implement QSP-based local Hamiltonian simulation scales at least quadratically with the system size.

Next, we compare the error robustness of the Rydberg implementation of the QSP-based Hamiltonian simulation for the disordered Heisenberg chain to that of a simulation algorithm based on the fourth-order product formula. For a fair comparison, we implement the product formula algorithm using the error-biased Rydberg atom gate set designed for QSP protocols. Hence, both implementations of the algorithm enjoy increased robustness against errors. Still, assuming the controlled unitaries are perfectly error biased, the QSP-based implementation has better asymptotic scaling of error probability. Moreover, we find that the QSP-based implementation has an overhead of the error probability that is reduced by more than an order of magnitude with respect to the fourth-order product formula.

The proposed implementation of the QSP-based Hamiltonian simulation algorithm has a few attractive features in the context of near-term implementation. First, thanks to the efficient design of the control conditions $|x_i\rangle$, the number of neutral atoms required to simulate a system of size $\leqslant 200$ can be as small as 250 atoms, which is small enough to ensure the near-term feasibility. Another factor that determines the near-term feasibility of the proposed implementation is the depth of the protocol, which is especially relevant for determining the influence of the adverse effects of errors that are *not* gate induced (i.e., errors affecting the hyperfine states of the neutral atoms). Our estimations indicate that, for intermediate-scale systems, the proposed Hamiltonian simulation algorithm can be implemented in a time that does not exceed the lifetime of the logical hyperfine states. However, given the current parameter regime describing the neutral atom experiments, the total error probability is not small enough to implement a Hamiltonian simulation of the disordered Heisenberg chain with less

than unity total error probability, except for small systems consisting of less than 50 atoms. Even so, we expect the concept of error-robust implementations to be advantageous for near-term demonstrations of QSP-based quantum information processing protocols when it is used in combination with error-mitigation techniques [64]. Moreover, the combination of the techniques introduced here with quantum error correction [32] promises to significantly ease realizations of fault-tolerant quantum computation in platforms where gate-induced incoherent errors dominate.

III. ERROR-ROBUST IMPLEMENTATIONS

The notion of error-robust implementations refers to methods to avoid unwanted processes that may occur during the implementation of a quantum operation by leveraging one's knowledge of (i) the computational task at hand and (ii) the dynamics of the controlled quantum system.

Error-robust implementation techniques are pervasive in quantum control theory [42,65,66], where the focus is to design control protocols for single- and two-qubit gates. Here, the impact of decoherence can be reduced by avoiding transitions to states susceptible to errors [42,67] and by designing (decoherence-free) subspaces, which are insensitive to the dominant error mechanisms [68–70]. In the context of quantum control theory, the figures of merit for error-robust implementations are the average error probability and the time duration of the implemented gates.

On the other hand, error-robust implementation of quantum protocols consisting of many gates has been, to the best of our knowledge, considered only in the context of quantum random access memories (QRAMs) with the bucket-brigade (BB) architecture [71–73]. The error-robust implementations of BB QRAMs focus solely on reducing error probability associated with each memory query because the *time* required for each query already scales logarithmically with the memory size. Unfortunately, the short time to query is a feature that comes at the cost of using as many qubits as the number of items in the memory. In this setting, the implementation of a QRAM is error robust if the probability of error scales sublinearly with respect to the memory size.

The proposals detailed in Refs. [71–73] show that the implementation of BB QRAM can be error robust, based on considerations of the interplay between the circuit structure and error processes. For instance, Ref. [72] proposes an error-robust implementation of BB QRAM on a device consisting of 2^n switches, where each switch can either be in an error-prone *active* state or an error-free *idle* state. As each memory query of a BB QRAM results in only $O(n)$ active switches, the resulting protocol is error robust. More recent results of Ref. [73] showed that the error robustness of the BB QRAM implementation does not rely on the idle states being perfectly error free, by carefully taking into account the propagation of errors amongst $O(2^n)$ qubits during the implementation of the QRAM unitary. However, it is not clear how the methods used to demonstrate the error robustness of BB QRAM can help design error-robust implementations of a wider class of quantum algorithms, and to do so without the requirement of an exponentially large system size.

Why have we not developed error-robust implementations for quantum protocols other than the BB QRAM? The core problem is the lack of a generic error measure that can separate the scaling of error probability from that of the circuit size. Conventional upper bounds for the total error measure increase linearly with both the circuit and the system size. This is because the conventional error bounds are defined on the worst- or average-case basis, assuming that we have no knowledge of the input states of the gates [39,43,44]. To see this formally, consider the worst-case error probabilities $\epsilon(\mathcal{E}_i, \mathcal{W}_i)$ defined using the trace distance between the desired output states of unitary transformations W_1 and W_2 and the respective erroneous processes $\mathcal{E}_1$ and $\mathcal{E}_2$:

$$\epsilon(\mathcal{E}_i, \mathcal{W}_i) \equiv \max_{\rho} \mathrm{tr}|\mathcal{W}_i(\rho) - \mathcal{E}_i(\rho)|, \quad i = \{1, 2\} \tag{1}$$

where $\mathcal{W}_i(\rho) \equiv W_i \rho W_i^\dagger$, and $|X| = \sqrt{X^\dagger X}$. Then the total error measure of the erroneous process $\mathcal{E}_2 \circ \mathcal{E}_1(\rho) \equiv \mathcal{E}_2[\mathcal{E}_1(\rho)]$ obeys the subadditivity bound (also called the chaining property) [39,44,74]

$$\epsilon(\mathcal{E}_2 \circ \mathcal{E}_1) \leqslant \epsilon(\mathcal{E}_1) + \epsilon(\mathcal{E}_2). \tag{2}$$

As a consequence, for a given quantum circuit $C \equiv \prod_i^{n_{\mathrm{gate}}} W_i$ compiling a desired quantum algorithm using n_{uni} perfect unitaries $\{W_i\}$, and the erroneous implementations of each unitary described by superoperators $\{\mathcal{E}_i(\cdot)\}$ which satisfy $\epsilon(\mathcal{E}_i) \leqslant \bar{\epsilon}\ \forall\ i$, the overall error measure associated with the implementation of C circuit is bounded by a linear function of gate [39,43,44]. Given this correspondence between the number of gates and the *conventional* error measures, determining whether an implementation is error robust as discussed in the Introduction requires us to define a different error measure. In particular, we need an error probability that is neither average nor worst case. In this work, we introduce such an error measure and show how it can be used to design error-robust implementations of QSP protocols.

Before defining the appropriate error probability, we emphasize that here we focus primarily on gate-induced incoherent errors, instead of the error processes which affect logical states in the absence of any external manipulation. The reason for this preference is the fact that in a wide variety of microscopic quantum systems, including the Rydberg atom arrays considered in this work, the quantum states that represent the logical qubits are extremely long lived as long as they are not manipulated. In these systems, the main error mechanisms are incoherent and induced when we want to control the dynamics of the system and implement the desired sequence of gates.

We now turn to define input-conditional error probability, which allows us to determine whether a given implementation is error robust. Our definition is inspired by previous work on Rydberg atoms that provided approximations of the error probability associated with one- and two-qubit gates for each initial state in the logical subspace [51,52]. Here, we anchor these previous results to a definition of error probability that also has attractive features from the perspective of quantum information science.

Indeed, the error probability introduced here simultaneously satisfies many of the conditions put forward in Ref. [44] for a "gold standard" in measures to compare real and ideal

quantum processes. In particular, the error probability we define here is easily related to a *distance measure* between pure states in the Hilbert space describing both the system and the environment. Importantly, when the error processes are incoherent the input-conditional error probability obeys a type of subadditivity bound, which allows us to lower bound the error probability for complex circuits. Moreover, our definition of error probability has a straightforward *physical interpretation* and is easy to estimate using the experimentally accessible properties of single atoms and simple time-dependent perturbation theory [75,76]. Finally, the proposed error probability is suitable for *efficient numerical calculation*, given an accurate model of the controlled system. We also note that our definition is an upper bound to the error probability based on the trace distance between mixed states [39] (see Appendix A).

We define error probability using the fidelity between two pure states that describe the system and the environment degrees of freedom: (i) the desired output state, simply given by $W_i|\phi_0\rangle$, and (ii) the erroneous output state $\tilde{W}_i|\phi_0\rangle$, which results from the imperfect implementation. The error probability conditioned on the input state $|\phi_0\rangle$ is defined as

$$\epsilon_{i,\phi_0} \equiv 1 - |\langle\phi_0|W_i^\dagger \tilde{W}_i|\phi_0\rangle|^2. \tag{3}$$

We emphasize again that all transformations involved in this definition are unitary, and that the input state $|\phi_0\rangle$ is taken into account explicitly. It is easy to see that the error amplitude $\sqrt{\epsilon_{i,\phi_0}}$ has the properties of a distance measure between the pure states $\tilde{W}_i|\phi_0\rangle$ and $W_i|\phi_0\rangle$ [44].

The error probability defined in Eq. (3) has an especially well-motivated physical interpretation for when the input states are error free and no quantum correlations exist between the controlled system and the environment. Formally, we define an error-free state as

$$|\phi_0\rangle \equiv |\phi_{0,\text{sys}}\rangle \otimes |\psi_{\text{env},0}\rangle, \tag{4}$$

where $|\phi_{0,\text{sys}}\rangle$ is the initial state of the system and $|\psi_{\text{env},0}\rangle$ is the initial reference state of the environment. Then we decompose $\tilde{W}_1|\phi_0\rangle$ as a linear combination of $W_1|\phi_0\rangle$ and an erroneous component

$$\tilde{W}_1|\phi_0\rangle \equiv \alpha_{1,\phi_0}|\phi_1\rangle + \sqrt{1-|\alpha_{1,\phi_0}|^2}\,\big|E_1^{\text{incoh}}\big\rangle. \tag{5}$$

Here, $|\phi_1\rangle \equiv W_1|\phi_0\rangle = |\phi_{1,\text{sys}}\rangle \otimes |\psi_{\text{env},0}\rangle$ is the desired output state, and $|E_1^{\text{incoh}}\rangle$ represents the states of the system and the environment when incoherent errors occur and the system becomes entangled to the environment in an irreversible way. Formally,

$$\big|E_1^{\text{incoh}}\big\rangle \equiv \sum_j \lambda_{\text{err},j}\big|E_{1,\text{sys,j}}^{\text{incoh}}\big\rangle \otimes |\psi_{j,\text{env,err}}\rangle, \tag{6}$$

where $\langle\psi_{\text{env},0}|\psi_{j,\text{env,err}}\rangle = 0$ and $\{\lambda_{\text{err},j}\}$ are the Schmidt values that quantify the amount of entanglement generated between the system and the environment by the erroneous unitary $\tilde{W}$ [39]. Moreover, we assume that the incoherent errors are due to a Markovian process such that the state $|E_1^{\text{incoh}}\rangle$ obeys $(\mathbf{I}_{\text{sys}} \otimes |\psi_{\text{env},0}\rangle\langle\psi_{\text{env},0}|)\tilde{U}|E_1^{\text{incoh}}\rangle = 0$ for any erroneous unitary $\tilde{U}$. From a physical point of view, $|\alpha_{1,\phi_0}|^2$ is the probability that the initial state $|\phi_0\rangle$ transitions to $W_1|\phi_0\rangle$ after it evolves under $\tilde{W}_1$.[3] The probability amplitude α_{1,ϕ_0} can be taken to be real and positive without loss of generality. Hence, the error probability ϵ_{1,ϕ_0} associated with the implemented unitary $\tilde{W}_1$ is simply given by

$$\epsilon_{1,\phi_0} = 1 - \alpha_{1,\phi_0}^2.$$

Unlike the conventional measures [43,44], ϵ_{1,ϕ_0} explicitly keeps track of the input states $|\phi_0\rangle$; and therefore, it allows us to design error-robust implementations where the error probability scales slower than the number of erroneous gates.

The following two relations are especially useful in determining whether a given implementation is error robust. The first relation allows us to estimate the error probability for any initial state given the error probabilities for a complete set of initial basis states. Given the error probabilities $\{\epsilon_{i,\phi_k}\}$ for an orthonormal basis $\{|\phi_k\rangle\}$, the error probability $\epsilon_{i,\Phi}$ associated with the unitary $\tilde{W}_i$ acting on $|\Phi\rangle \equiv \sum_k a_k|\phi_k\rangle$ is (see Appendix A for details)

$$\epsilon_{i,\Phi} \approx \sum_k |a_k|^2\epsilon_{i,\phi_k} + O\big(\max_k \epsilon_k^2\big). \tag{7}$$

The second relation is an inequality that is similar to the subadditivity property discussed above. It allows us to calculate the upper bound for the error probability for a circuit $C \equiv \prod_{j=1}^n W_j$, given the error probabilities $\epsilon_{j,\phi_{j-1}}$ for each unitary W_j acting on the error-free state $|\phi_{j-1}\rangle \equiv \prod_{l=1}^{j-1} W_l|\phi_0\rangle$. In particular, for a circuit C consisting of n unitaries, the error probability obeys (see Appendix A for details)

$$\epsilon_{C,\phi_0} \leqslant \sum_{j=1}^n \epsilon_{j,\phi_{j-1}}. \tag{8}$$

An important aspect of the error bound in Eq. (8) is that it is valid in the presence of time-correlated errors since the erroneous component of the wave function is completely discarded after each unitary $\{\tilde{W}_i\}$. This feature is especially important for errors resulting from black-body radiation in Rydberg atoms, which we further discuss in Sec. V. We also note that Ref. [50] uses a fidelity measure that shares this feature.

How can we calculate $\{\epsilon_{j,\phi_{j-1}}\}$? We show that given an input state $|\phi_0\rangle$ and a Markovian master equation describing the driven and dissipative dynamics of the system, an upper bound of error probability for each unitary W_j can be analytically calculated for time-independent or adiabatically control pulses. In particular, considering a system evolving under W_j and subject to jump operators $\{C_m\}$, the error probability in the limit $\epsilon_{j,\phi_0} \ll 1$ obeys (see Appendix A for details)

$$\epsilon_{j,\phi_0} \leqslant \tau_g \sum_\psi p_{\psi,j}^{\max}\gamma_\psi. \tag{9}$$

Here, τ_g is the time required for the implementation and $p_{\psi,j}^{\max}$ denotes the maximum occupation of $|\psi\rangle$ during the evolution described by W_j. The wave function $|\psi\rangle$ is the eigenstate

[3]We note that $|\alpha_{1,\phi_0}|^2$ is similar to the survival probability that is defined in the randomized benchmarking literature $|\alpha_{1,\phi_0}|^2$, where the target operation is identity.

of the non-Hermitian effective Hamiltonian $\frac{i}{2}\sum_m C_m^\dagger C_m$ with eigenvalue $\gamma_\psi/2$ that is half the decay rate γ_ψ [77]. As we demonstrate in the following sections, that ϵ_{j,ϕ_0} can be upper bounded using analytical methods is an important feature of the input-conditional error probability for the designing error-robust implementations.

The proof of Eq. (9) follows from the results derived using the stochastic wave-function description of dissipative dynamics [77,78]. In particular, $1-\epsilon_{j,\phi_0}$ is the probability that no quantum jumps occur during the system's evolution during $\tilde{W}_j$. Hence, we can define the input-conditional error probability as

$$\epsilon_{j,\phi_0} \equiv 1 - \left|\langle\phi_0|\mathcal{T}\exp\left(i\int_0^{\tau_g} H_{j,\mathrm{eff}}(t)\right)|\phi_0\rangle\right|^2, \tag{10}$$

where $H_{j,\mathrm{eff}}(t)$ is the time-dependent effective non-Hermitian Hamiltonian associated with the Markovian stochastic evolution, $\mathcal{T}$ is the time-ordering operator, and τ_g is the gate duration. Equation (9) results from bounding the right-hand side of Eq. (10).

On the other hand, numerical bounds on error probability are useful when predicting the performance of an implementation on a specific device. Luckily, it is also straightforward to calculate ϵ_{j,ϕ_0} using a numerical simulation of the Markovian master equation, when such a description is valid. This can be achieved through a simple modification of simulation of the Markovian master equation, where each jump operator C_m is augmented to construct a new jump operator $\tilde{C}_m \equiv C_m \otimes |e\rangle_{\mathrm{flag}}\langle g|$, where $|e/g\rangle_{\mathrm{flag}}$ are the states of an unphysical auxiliary flag qubit. For the numerical simulation, the flag qubit is initialized to the $|g\rangle_{\mathrm{flag}}$ state. During the Markovian evolution of the system, the flag qubit transitions to the $|e\rangle_{\mathrm{flag}}$ state whenever a quantum jump occurs. Hence, the error probability ϵ_{j,ϕ_0} can be numerically calculated by measuring the population in the $|e\rangle_{\mathrm{flag}}$ state at the end of the simulation. In our numerical calculations, we found that the occupation of the flag qubit perfectly matches the estimates based on the second term on the right-hand side of Eq. (9).

If we want to calculate the upper bound of the error probability for a given circuit C, we need to have at least partial knowledge of the ideal state $|\phi_i\rangle$ after the application of each unitary W_i. This is clearly not possible without prior knowledge of the initial state $|\phi_0\rangle$ and the circuit C. Indeed, the motivation behind using the worst- or average-case error probabilities comes from the fact that, in general, we do not have a concise description of each $|\phi_i\rangle$. However, because we are interested in implementing quantum signal processing (QSP) protocols where the block-encoding unitary is realized using linear combination of unitaries (LCU), we can do better. As we will elaborate in the next section, during most of the implementation of the LCU-based block-encoding unitary, the probability that each ancilla qubit is in one of the two logical states does not change. Moreover, the LCU implementation is flexible with respect to how we encode information in the ancillary degrees of freedom. Hence, we can design the encoding of the ancillary degrees of freedom such that the ancillae remain only in a restricted subspace of the total Hilbert space during the implementation of the LCU unitary. The evolution of the ancillary degrees of freedom within a carefully designed restricted subspace is at the core of our proposal for error-robust implementations of QSP protocols.

To summarize, in this section, we defined an error probability that is closely related to the fidelity on the joint Hilbert space of the system and the environment. The defined error probability satisfies most of the conditions put forward in Ref. [44] for a successful error measure, including a clear physical interpretation and ease of computation. In addition, the error probability that we defined here allows one to keep track of the error conditional on the input state of each unitary that makes up the quantum protocol using Eqs. (7) and (8). In the next section, we describe the LCU method for compiling the block-encoding unitary and clearly state the requirements for achieving an error-robust implementation (see Sec. IV C). Then, in Sec. V, we shift our focus to a detailed model of the Rydberg atom array and discuss the implementation of single-qubit and multiqubit gates which are useful for an error-robust implementation of QSP protocols. In Sec. VII, we will calculate the overall error probabilities for QSP protocols using Eq. (8) and the error model of each Rydberg gate.

IV. BLOCK ENCODING BY LINEAR COMBINATIONS OF UNITARIES (LCU)

Here we discuss the method of LCU [53], which offers a generic and constructive strategy to implement QSP iterates. In order to assess the time and space complexities of the LCU method, we introduce the scaling variable N which denotes the number of Pauli operators $\{P_i\}$ that make up the target block-encoded operator A. In particular, we consider A that can be decomposed as

$$A = \sum_{i=1}^{N} |\alpha_i|^2 P_i, \tag{11}$$

where P_i is a tensor product of single-qubit Pauli operators and $\sum_{i=1}^{N}|\alpha_i|^2 = 1$. It is conventional to restrict the *weight* of each P_i, which is given by the number of its nonidentity factors. In the context of Hamiltonian simulation, the number of coefficients required to implement a k-local Hamiltonian (i.e., each P_i has a weight at most k) on a system consisting of n_{site} qubits is $N = O(n_{\mathrm{site}}^k)$, while for geometrically local Hamiltonians where the number of atoms within an interaction range is N_I, we have $N = O(N_I^k n_{\mathrm{site}})$. It is important to note that in this decomposition we assume that the coefficients $\{\alpha_i\}$ are given and cannot be further compressed into a smaller set.

In the following, we first review the LCU method formally, and describe how quantum signal processing can be used to implement approximate functional transformations of the block-encoded operator A. Then in Sec. IV C, we demonstrate that the LCU-based QSP iterates can be implemented with constant input-conditional error probability when one has access to perfectly error-biased multicontrol unitaries.

A. Algorithm

The LCU decomposition of the block-encoding unitary in Eq. (16) consists of three unitaries [53]:

$$U = V^\dagger \bar{U} V. \tag{12}$$

The block-encoding unitary acts on n_a ancilla qubits and n_{site} system qubits. The unitary V rotates the n_a-qubit initial ancilla state $|0\rangle^{\otimes n_a}$ to a linear combination of computational basis states $\{|x_i\rangle\}$ which encodes the precomputed classical coefficients α_i:

$$|\Psi\rangle_a \equiv V|0\rangle^{\otimes n_a} = \sum_{i=1}^{N} \alpha_i |x_i\rangle. \tag{13}$$

The operator V can be understood as an amplitude-encoding state-preparation unitary [79]. We note that the number of ancilla qubits $n_a \leqslant \lceil \log N \rceil$ depends on the choice of the basis $\{|x_i\rangle\}$.

Then, we apply the following conditional unitary operation:

$$\bar{U} \equiv \sum_{i}^{N} |x_i\rangle\langle x_i| \otimes P_i \equiv \sum_{i=1}^{N} C_{x_i} P_i. \tag{14}$$

In the following, we refer to $\{|x_i\rangle\}$ address states or control conditions. When the control register is in $|x_i\rangle$, it satisfies the control condition of the controlled unitary $C_{x_i}P_i$. The action of $\bar{U}$ entangles each Pauli operator with an orthogonal *address* state of the ancilla register

$$\sum_{i=1}^{N} \alpha_i |x_i\rangle \otimes |\Psi_{\text{sys}}\rangle \xrightarrow{\bar{U}} \sum_{i=1}^{N} |x_i\rangle \otimes (\alpha_i P_i)|\Psi_{\text{sys}}\rangle. \tag{15}$$

A unitary that block encodes a superposition of multiqubit Paulis $\{P_i\}$ is obtained by rotating the address space by an application of $V^\dagger$,

$$\begin{aligned} V^\dagger \bar{U} |\Psi\rangle_a \otimes |\Psi_{\text{sys}}\rangle &= \sum_{i}^{N} |\alpha_i|^2 |0\rangle^{\otimes n_a} \otimes P_i |\Psi_{\text{sys}}\rangle + |\Psi^\perp\rangle \\ &= |0\rangle^{\otimes n_a} \otimes [A|\Psi_{\text{sys}}\rangle] + |\Psi^\perp\rangle, \end{aligned} \tag{16}$$

where the unnormalized wave vector $|\Psi^\perp\rangle$ satisfies $((|0\rangle\langle 0|)^{\otimes n_a} \otimes \mathbf{1})|\Psi^\perp\rangle \equiv \Pi_0|\Psi^\perp\rangle = 0$. Consequently, $\Pi_0 U \Pi_0 = A$, and the block-encoding unitary has the form

$$U \doteq \begin{pmatrix} A & * \\ * & * \end{pmatrix}. \tag{17}$$

We remind the reader that the unitarity of U implies that the Hermitian operator block encoded in this way satisfies $||A|| \leqslant 1$. Moreover, the block-encoding unitary implemented through LCU is Hermitian (i.e., $U^\dagger = U$).

An aspect of the LCU protocol that is especially important for error-robust implementations is that we are free to choose the relevant subspace of the ancillary degrees of freedom. The original discussion of block-encoding unitary sets $n_a = \lceil \log(N) \rceil$ [54] such that the relevant subspace is the whole Hilbert space of the ancillary address register. Here, we show that the implementations of the block-encoding unitary can be made efficient if we use an address register that is constrained to states with only a small number of qubits in the $|1\rangle$ state.

B. Processing of block-encoded matrices by QSP

Next, we review the QSP framework introduced in Refs. [45,58]. From the perspective of compiling quantum subroutines and algorithms. QSP can be understood as an efficient way of manipulating a block-encoded operator A to realize the block encoding of a polynomial functional $P(A)$. The polynomial $P(\cdot)$ is defined through an ordered list of $n+1$ angles $\{\phi_i\}$, whose size determines the order of the polynomial as well as the query complexity of QSP. Here, we give only a brief discussion of the QSP protocol such that the requirements for its error-robust implementation become evident. For an introduction to QSP, see Appendix C.

The QSP protocols proceed by iterating between a controlled oracular unitary CW derived from the block-encoding unitary U in Eq. (12), and a signal processing step, which consists of a single-qubit rotation on the additional ancilla (referred to as the exit ancilla) that controls the application of W (see Fig. 1). Formally, the QSP protocol has the form

$$\mathcal{U} = \left[\prod_{i=1}^{n} e^{i\phi_i \sigma_x^{(e)}} \mathrm{C}_e W \right] e^{i\phi_0 \sigma_x^{(e)}}, \tag{18}$$

where $\sigma_x^{(e)}$ acts on the exit ancilla. In the case of a qubitized block-encoding unitary $U = U^\dagger$, oracular unitary W is simply expressed as

$$W = (2\Pi_0 - \mathbf{I})U, \tag{19}$$

where Π_0 is the projector to the all-zeros address state. As emphasized in the Introduction, the iterative form of the QSP protocols allows for error-robust implementations given that the implementation of CW is error robust.

C. A sufficient condition for an error-robust implementation of the QSP protocols

Here, we identify a condition, when satisfied, that allows one to design error-robust implementations of LCU-based QSP protocols with near-constant input-conditional error probability. The condition we put forward is chosen to illustrate the possibility of error-robust implementations but it is likely impossible to be perfectly satisfied in any physical realization. Given this difficulty, the rest of our work will focus on demonstrating that a more restricted and physically viable set of conditions is sufficient for error-robust implementations of LCU-based QSP protocols.

Consider an LCU-based QSP protocol implementing an order-n polynomial transformation $P(A)$ where the block-encoded signal operator A is a linear combination of N k-local Pauli operators. Then, if the required controlled unitaries are implemented in a way that incoherent errors are induced only when the control condition is satisfied (i.e., Condition 1 in Sec. II B is perfectly satisfied), then the said QSP protocol can be implemented with an $O(k + \log N)$ input-conditional error probability. We remind the reader that the control condition is satisfied when the control register occupies a state that results in a nontrivial evolution of the target qubits.

To see how this condition results in such a drastic reduction of the input-conditional error probability let us first calculate the error probability in Sec. V E on the unitaries $\bar{U}$ in Eq. (12) and $2\Pi_0 - \mathbf{I}$. The total error probability $\epsilon_{\bar{U},\psi}$ for implementing $\bar{U}$ is upper bounded by the sum of input-conditional error probabilities for implementing each multicontrol Pauli

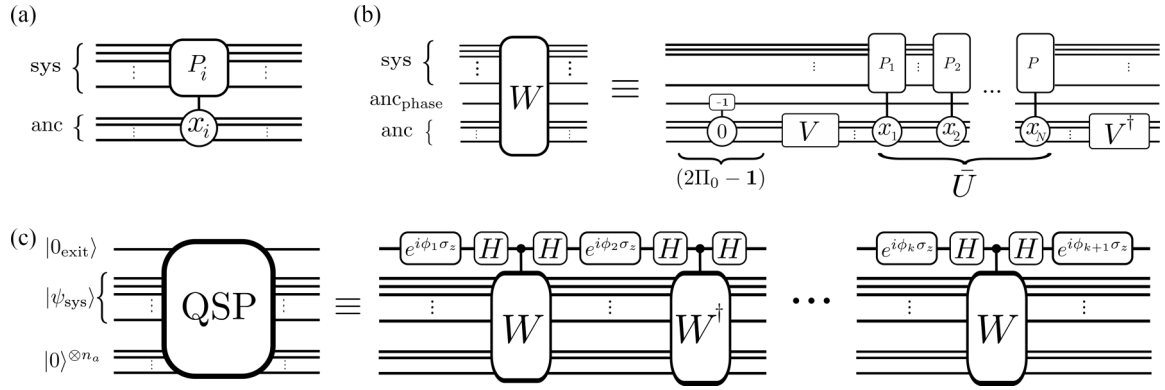

FIG. 1. The circuit diagrams for the QSP protocols discussed in this work. (a) The multiqubit controlled Pauli operation $C_{x_i}P_i$ where the control register is ancillary and the target register is the system that is controlled. (b) The decomposition of the QSP iterate W (notice the factor of i difference with the definition in Ref. [45]), consisting of a multiqubit controlled phase gate where the target register is a single-"phase" ancilla and the LCU-based block-encoding protocol. (c) The circuit decomposition of the QSP method for producing polynomials of block-encoded matrices, which consists of controlled versions of the walk operator W conditioned on the state of an additional "exit ancilla." In this work, we show how to realize error-robust implementations of these circuits on the Rydberg atom platform.

operator. That is, considering $\bar{U}$ that consists of N multicontrol Pauli operators (see Sec. II B)

$$\epsilon_{\bar{U},\psi} \leqslant \sum_{j=1}^{N} \epsilon_{C_{x_j}P_j,\psi_{j-1}}, \tag{20}$$

where $|\psi_j\rangle$ stands for the error-free state at the end of the jth controlled Pauli operation. If $C_{x_j}P_j$ results in errors only for the component of $|\psi_{j-1}\rangle$ along $|x_j\rangle$, then defining

$$\alpha_j \equiv \text{Tr}[(\langle x_j| \otimes \mathbf{I})|\psi_{j-1}\rangle]/2^{n_{\text{site}}},$$

we find

$$\epsilon_{C_{x_j}P_j,\psi_{j-1}} = \epsilon_0 |\alpha_j|^2 k_j, \tag{21}$$

where ϵ_0 is a constant describing the overall error probability scale, and $k_j \leqslant n_{\text{site}}$ is the weight of the Pauli operator P_j acting on a system of size n_{site}. Therefore, using the normalization condition $\sum_{j=1}^{N} |\alpha_j|^2 = 1$, we obtain

$$\epsilon_{\bar{U},\psi} \leqslant \epsilon_0 \max_j k_j = O(k). \tag{22}$$

The proposed implementation of $\bar{U}$ is error robust since the number of gates that need to be implemented scales with N. Similarly, because the reflection operator $2\Pi_0 - \mathbf{I}$ can be expressed as a multiqubit controlled Z operation, the input conditional error probability associated with its implementation is $<\epsilon_0$ and does not scale with N. Finally, we note that single-qubit controlled versions of both $\bar{U}$ and $\mathbf{I} - 2\Pi_0$ can be implemented without changing the bound on the input-conditional error probability, as long as Condition 1 is satisfied. As a result, given multiqubit Pauli operations that satisfy Condition 1, CW can be implemented with $O(k)$ error probability if the state preparation unitary V can be implemented with $O(k)$ error probability.

Surprisingly, the state preparation unitary V can be implemented with only $O(\log N)$ error probability if Condition 1 is satisfied. Consider a state preparation unitary V acting on $n_a \equiv \lceil \log N \rceil$ qubits. Then the unitary V can be expressed as a sequence of $\tilde{O}(N)$ multiqubit controlled single-qubit rotation operations [80]. To see this, first order the qubits q_j from 1 to n_a and initialize each qubit in the $|0\rangle$ state. Then for each qubit q_j with $j \in (0, \ldots, n_a)$ apply 2^{j-1} multiqubit controlled single-qubit rotations, where the control atoms are chosen from the set $\{q_l\}$ with $l < j$. It is then possible to prepare any state that encodes a set of $N \leqslant 2^{n_a}$ precomputed probability amplitudes (as in Sec. IV) using an appropriate choice of the single-qubit rotation angles [80]. Now consider an implementation of the circuit described above where Condition 1 is satisfied. Although for each qubit q_j, we apply a large number of controlled single-qubit rotations, the probabilities that the control conditions of each multiqubit controlled single-qubit rotation is satisfied sum up to 1 in the same way that resulted in Eq. (22). Hence, given Condition 1 is satisfied, the total input-conditional error probability is $O(\log N)$. Moreover, a controlled version of this unitary can be implemented without changing the error probability. As a result, the implementation of CW has an input-conditional error probability $O[k + \log(N)]$.

The above arguments show that near-constant error implementations of LCU-based QSP protocols are possible given perfectly error-biased multiqubit controlled unitaries. However, it is clear that, in any physical setting, the gate implementation will also result in errors when the control condition is not satisfied, and Condition 1 cannot be perfectly satisfied. That is, the condition of having the perfectly error-biased multiqubit controlled unitaries can only serve as a guideline in the discussion of designing gates for error-robust implementations of algorithms. In particular, the argument presented in this subsection highlights the error-bias parameter η_ϵ, given by the ratio between the error probabilities when the control condition *is not* satisfied over that when the control condition *is* satisfied, as a key quantity of interest. Broadly speaking, the constant scaling of the input-conditional error probability holds for $N < \eta_\epsilon^{-1}$. The calculation of the error-bias parameter η_ϵ for realistic gate implementations using Rydberg atoms is the focus of the next section. Specifically, we use analytical and numerical methods discussed in Sec. II E to estimate η_ϵ for two types of multiqubit gates that can be implemented using Rydberg atoms. As we

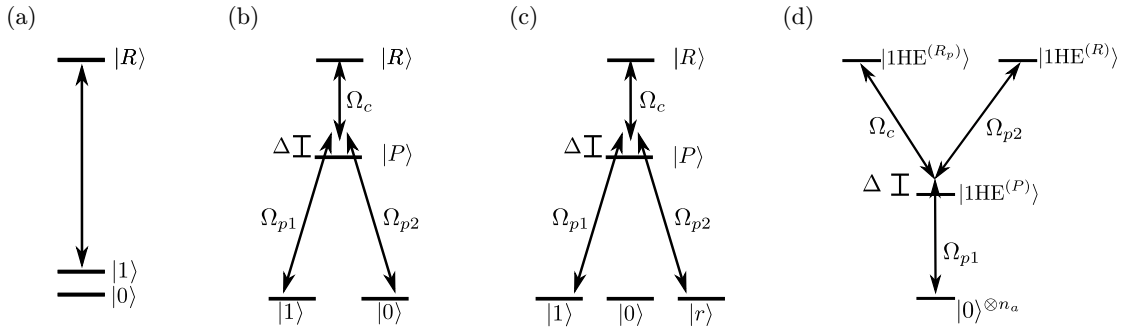

FIG. 2. The level diagrams used in the proposed protocols in the laboratory frame. (a) The level diagram for the Rydberg atoms in the control registers, where a hyperfine state is excited to the Rydberg manifold. (b)–(d) Three different level diagrams for the Rydberg atoms in the target registers, each using the EIT mechanism [see (b)] to introduce biased errors that conditionally are on the state of the control register. (c) The level diagram for the target atom of the $CX^{(R)}$ gate. The transfer between $|1\rangle$ and $|r\rangle$ is controlled by the energy shift of state $|R\rangle$, followed by an excitation to the Rydberg state. (d) The level scheme of the multiqubit target register for the CV_{1HE} gate. The state $|1\mathrm{HE}^{(\psi)}\rangle$ is a one-hot encoding state where the atoms not in the $|0\rangle$ state occupy the single-qubit state $|\psi\rangle$. Here, the pairs of hyperfine states in (b) and (c) are replaced by the multiqubit states $|0\rangle^{\otimes n_a}$ and $|1\mathrm{HE}^{(R)}\rangle$.

conclude this general discussion of error-robust implementations of QSP protocols, we remind the reader that implementing controlled unitaries with small η_ϵ on *any* platform will lead the way to the realization of error-robust protocols.

V. RYDBERG ATOM GATES

In this section, we introduce the building blocks for error-robust implementation of QSP protocols on the Rydberg atom platform. We briefly review the relevant atomic level diagrams and discuss the associated dipolar interactions and decoherence mechanisms in Sec. V A. The implementation of single-qubit rotations is discussed in Sec. V B.

In Secs. V C and V D, we introduce two multiqubit gates that utilize the Rydberg blockade mechanism. Each multiqubit gate serves a different function in the error-robust implementation of the LCU-based block-encoding unitary. In Sec. V C, we introduce a single-qubit controlled Pauli operation based on electromagnetically induced transparency (EIT). We show that in the parameter regime that is accessible to current experiments, the error probability can be reduced by more than a 100-fold when the control condition is not satisfied ($\eta_\epsilon < \frac{1}{200}$). The second multiqubit gate, which we refer to as the one-hot encoding gate (see Sec. V D), allows us to load the classically stored coefficient data $\{\alpha_i\}$ efficiently to orthogonal ancillary address states. The one-hot encoding gate and its single-qubit controlled version are the building blocks of the state preparation unitary V in the LCU protocol [see Eq. (12)]. Surprisingly, when the Rydberg blockade radius is larger than the system size, the one-hot encoding gate can be implemented in constant time and with constant error probability. Moreover, our simulations for the controlled one-hot encoding gate with two-target qubits show that $\eta_\epsilon < \frac{1}{150}$ is achievable. For both gates introduced here, we comment on how the error characteristics will change as we increase the number of target qubits, when appropriate.

However, because η_ϵ can in principle be reduced, we continue the discussion of error-robust implementations in Secs. VI and VII assuming that Condition 1 is perfectly satisfied. Moreover, we introduce what we call an error bounded gate count (EBGC), which codifies the error characteristics of the Rydberg atom gates under simplifying assumptions such that we can evaluate the error robustness of a protocol without referring to the exact lifetimes of different atomic states. To this end, EBGC expresses the associated error probabilities as simple fractions of the maximum error probability of a single CNOT (controlled NOT) gate. EBGC allows us to clearly demonstrate the error robustness of the proposed implementation of QSP protocols, in a similar fashion as in Sec. II E.

Using the EBGC, we construct a concrete error-robust implementation of the QSP iterate in Sec. VI. In Sec. VII, we benchmark the input-conditional error probability for a Rydberg atom implementation QSP-based Hamiltonian simulation algorithm against that of two state-of-the-art Hamiltonian simulation algorithms [49,50]. There, we also relax the assumptions of the EBGC and discuss the prospect of realizing the proposed Hamiltonian simulation algorithm on near-term devices.

A. Rydberg interactions, level diagrams, and single-qubit rotations

The four level diagrams that are relevant to our implementation are shown in Fig. 2. The diagrams consist of three types of states. Although these diagrams greatly simplify the experimental reality, the three types of states provide sufficient correspondence between our work and the experimental setup. First, we have three long-lived hyperfine states $|0\rangle$, $|1\rangle$, and $|r\rangle$. The states $|0\rangle$, $|1\rangle$ span the logical subspace of each atom, and $|r\rangle$ is a long-lived auxiliary state. Second, we have a short-lived intermediate state $|P\rangle$ that is useful for implementing rotations between hyperfine states as well as those between the hyperfine and Rydberg states. Lastly, we utilize high-energy Rydberg states $|R\rangle$ and $|R_p\rangle$, which have shorter lifetimes than the hyperfine states. In addition, the Rydberg states evolve under an interacting Hamiltonian

$$H_R = \sum_{ij} J_{ij} |R_i R_j\rangle\langle R_i R_j|, \tag{23}$$

where $|R_iR_j\rangle \equiv |R_i\rangle \otimes |R_j\rangle$ describes the state in which the ith and jth atoms located at positions r_i and r_j simultaneously occupy the Rydberg state. The interaction strength has the form $J_{ij} \propto \frac{1}{|r_i - r_j|^\nu}$ with $\nu \in \mathbf{N}$, although it is often convenient to model the spatial dependence as a step function which takes the finite value J when $|r_i - r_j| < R_b$ and vanishes otherwise. Here, the distance R_b will be referred to as the "blockade radius." We will use both descriptions of the dipolar interactions depending on the context.

Let us now turn to the characteristic values describing the strength and range of dipolar interactions as well as the strength of main decoherence processes. For our constructions in Sec. V, we need both *short*- and *long*-range dipolar interactions. While the long-range dipolar interactions between the Rydberg states are useful for the one-hot amplitude encoding gate that we discuss in Sec. V D, the possibility using short-range interactions plays an important role in implementing a parallelized version of the controlled Pauli operators required for $\bar{U}$. Fortunately, the required characteristics can be in principle realized with the current experimental setups [8,51,81,82]. The two main factors which affect the range of dipolar interaction between Rydberg atoms are (i) whether the dipolar interactions are of long-ranged resonant dipole-dipole type ($\nu = 3$) or of short-ranged van der Waals type ($\nu = 6$) and (ii) the dipole moments associated with different Rydberg states [8,51,81]. The short-range van der Waals type interactions can reach up to 30 MHz at a distance of $\simeq 6$ μm [48]. On the other hand, the resonant dipolar interactions can be much stronger at long distances compared to the van der Waals potentials. The resonant dipolar interactions can be utilized by applying an additional DC electric field on the Rydberg atoms, which can result in an interaction strength of 1 MHz at a distance of 30μm [51,83,84]. The long-range interactions come at the price of an anisotropic interaction strength that depends on the angle between the interatomic axis and the electric field. However, when the atoms are in a two-dimensional plane that is orthogonal to the direction of the external electric field, the interactions are effectively isotropic.

Next, we give a brief discussion of the decoherence mechanisms which determine the lifetime of the different energy levels of the neutral atoms. In our work, we focus only on alkaline-earth atoms. In these systems, the logical qubit degrees of freedom are encoded in hyperfine states, whose coherence times of these states can exceed 10 s [85–87]. The main decoherence mechanisms involve collisions with the background atoms, light scattering, and fluctuations in external control fields, as well as the magnetic noise, intensity noise in optical traps, and motion of the atoms within the trapping potential [6,88]. However, because the lifetime of the hyperfine states is much longer than all other states used in our protocols, we neglect the decoherence mechanisms that affect the hyperfine states to a large extent. We comment on the constraints due to the finite lifetime of the hyperfine states for Hamiltonian simulation in Sec. VII.

On the other hand, the intermediate and Rydberg states that enable quantum information processing with Rydberg atoms have drastically different coherence properties compared to those of the low-energy hyperfine states. As discussed in Sec. II E, this separation of the decoherence rates is what motivates us to study gate-induced errors. For alkali atoms, Rydberg state lifetimes exceeding 250 μs were reported in Ref. [89]. The main mechanisms for a finite lifetime are spontaneous emission which causes transitions to states with lower principal numbers and black-body radiation which causes transitions to nearby Rydberg states. Black-body radiation events have received considerable attention because they can result in correlated errors that are challenging for any fault-tolerant platform [32]: the final state of the atom upon interacting with the ambient thermal radiation is a dark Rydberg state, which continues to influence its neighbors through strong dipolar interactions. However, the subadditivity property of the input-conditional error probability in Eq. (8) implies that the effect of correlated errors such as those results from BBR do not increase with time. Hence, for the following calculations of the error probability, we use the *aggregate* decay rate given by the experimentally accessible lifetimes of the Rydberg states. We also note that the processes due to black-body radiation can be slowed down substantially by cooling the atoms down to μK temperatures [51]. Finally, the errors due to decoherence mechanisms affecting the intermediate state $|P\rangle$ result in typical lifetimes of the order of about 100 ns [48], which is primarily a result of radiative decay processes.

In the following discussion, we assume that technical errors due to laser phase and amplitude fluctuations and those due to the finite-temperature atomic motion and the associated Doppler shift can all be eliminated by improved laser systems and sideband cooling of the atomic motion [81,90–93]. However, as discussed further below, we expect that, in general, such technical errors will result in a smaller error-bias parameter η_ϵ, while increasing the overall error rate [e.g., ϵ_0 in Eq. (22)]. The reason for this expectation is that the neutral atom system is more susceptible to technical errors when the atoms interact with the laser fields that control them. However, the dynamics that we discuss below are designed to reduce the interaction between the control fields and the atoms when the control condition is not satisfied. We also assume that whenever needed, the undesired interactions between the target atoms can be substantially smaller than that between the control and target atoms, using the techniques introduced in Ref. [94], although for certain applications the desired effect can be achieved solely through a suitable geometric arrangement of the atoms.

B. Single-qubit rotations

For the implementation of single-qubit rotations, we choose to use $|P\rangle$ as the intermediate state [see Fig. 2(a)]. Specifically, we can drive transitions between the logical states $|0\rangle$ and $|1\rangle$ using a Raman scheme which virtually excites the short-lived intermediate state $|P\rangle$ [95]. As described in Sec. II E, the probability of incoherent errors due to the short lifetime of the intermediate state can be upper bounded using the duration of the gate as well as the maximum occupation probability of the $|P\rangle$ state.

C. EIT-based single-control multitarget unitary on the Rydberg platform

In Sec. IV C, we determined that error-robust implementations of QSP protocols can be realized using error-biased

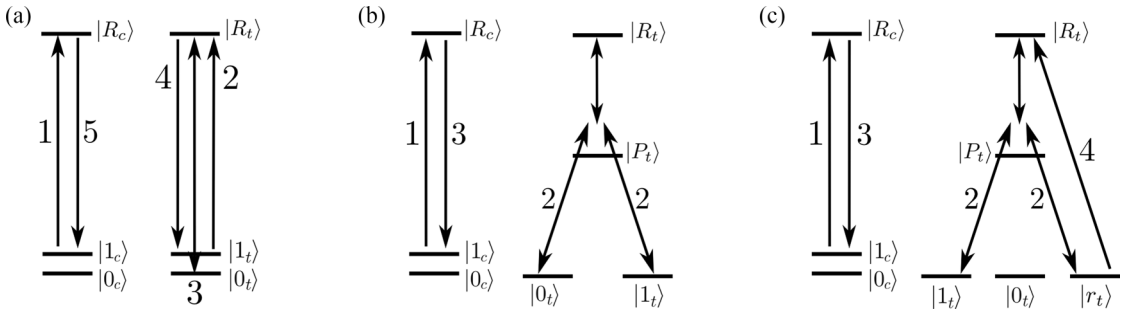

FIG. 3. The pulse sequences for implementing the three conditional unitaries that are used to implement the algorithms in the QSP framework. The strengths of each laser pulse are given in Fig. 2. (a) The pulse sequence for the conventional two-qubit conditional gate (CNOT) on the Rydberg atom platform implemented via the blockade mechanism. Notice that there is substantial error probability both when the control condition is satisfied and violated. (b) Implementation of the EIT-based blockade gate which results in an error model that is strongly biased on the state of the control atom. Notice that the control laser on the target register is always on, and hence does not have a number associated with it. (c) The laser pulse sequence for implementing the conditional excitation to the Rydberg state, denoted $CX^{(R)}$ in the main text.

multiqubit controlled Pauli operations which accumulate errors only when the control condition is satisfied.

Here, we describe the concrete protocol for error-biased *single-qubit* controlled Pauli operations. In Sec. V C, we describe how these single-qubit controlled unitaries can be used for an error-robust implementation of $\bar{U}$. We also briefly introduce a conventional multiqubit controlled gate implementation, that, despite not exhibiting strong error bias, is useful for the error-robust implementation of the reflection operation $\mathbf{I} - 2\Pi_0$.

The gate we consider was first proposed in Ref. [60], as a solution to realizing multitarget controlled gates where the gate fidelity is minimally affected by the undesired or residual dipolar interactions between the target qubits. In this context, the advantage of the proposed implementation is that it drastically reduces the excitation of atoms to the Rydberg state during the protocol, independently of whether the control condition is satisfied or not. This is in contrast to the conventional two-qubit gates using the Rydberg blockade [3,21,48], where the Rydberg state of the target atom is occupied with near unity probability when the control condition is satisfied.

Here, we argue that the single-qubit controlled Pauli operation of Ref. [60] has an additional and underappreciated feature that is a crucial resource for implementing error-robust protocols. Specifically, the EIT-based gate results in a large bias between the error probabilities conditional on the state of the control qubit. Moreover, the ratio η_ϵ between the error probabilities when the control condition *is not* over *is* satisfied can be changed using the relative ratio of the two laser intensities used for the implementation. Below, we demonstrate this claim using both analytical and numerical simulation results. We show that using experimental parameters reported in the literature, $\eta_\epsilon < 1150$ is achievable for a few tens of target atoms.

Protocol. We start the discussion of the EIT-based blockade gates with the implementation of a CNOT gate [60]. The scheme uses the level scheme in Figs. 2(a) and 2(b) for the control and target qubits, respectively. The target qubit is continuously driven by a control field Ω_c during the three-step protocol depicted in Fig. 3(b). In the first step, the control atom is excited to a Rydberg state if it satisfies the control condition (say $|1_c\rangle$). Second, lasers inducing the two time-dependent probe Rabi frequencies $|\Omega_p(t)|e^{i\theta_1}$ and $|\Omega_p(t)|e^{i\theta_2}$ are shone on for the target atom. Finally, the population in the Rydberg state of the control atom is deexcited to the $|1_c\rangle$.

The frequencies of the control and probe laser amplitudes are such that the excitation to the Rydberg state is two-photon resonant. In the following, we denote the detuning between the hyperfine and intermediate states as Δ, and define the radiative decay rates γ_R and γ_P of the states $|R\rangle$ and $|P\rangle$, respectively. We also consider an experiment satisfying a set of inequalities that define the perturbative regime

$$J > \frac{|\Omega_c|^2}{4\Delta} \gg \Omega_p^{\max} \gg \{\gamma_R, \gamma_P\},$$

where we have $\Omega_p^{\max} \equiv \max_t |\Omega_p(t)|$.

The second step of the protocol separates the EIT-based protocol from its conventional counterparts [3,21]. Two scenarios are relevant for the evolution during the second step (see Appendix B for detailed derivations):

(1) If the control atom is not in the Rydberg state, then both logical states of the target atom evolve adiabatically in a subspace spanned by

$$|\psi_d\rangle = \frac{1}{\sqrt{1-x^2}}(|\psi_l\rangle + x|R\rangle),$$
$$|\tilde{\psi}_d\rangle = \frac{1}{\sqrt{2}}\left(|0\rangle - e^{i(\theta_1-\theta_2)}|1\rangle\right),$$

and eventually, return back to the initial state [60]. In the above expression, we defined $x \equiv |\sqrt{2}\Omega_p/\Omega_c|$ as a time-dependent dimensionless quantity. The logical state $|\psi_l\rangle = \frac{1}{\sqrt{2}}(|0\rangle + e^{i(\theta_1-\theta_2)}|1\rangle)$ is orthogonal to $|\tilde{\psi}_d\rangle$. Most importantly, neither $|\psi_d\rangle$ nor $|\tilde{\psi}_d\rangle$ have a contribution from the short-lived intermediate state $|P_t\rangle$. Hence, the errors due to the occupation of the short-lived $|P_t\rangle$ state are eliminated as long as the EIT condition is satisfied.

(2) If, on the other hand, the control condition is satisfied and the control atom is excited to its Rydberg state, then

the EIT condition is strongly violated. As a result, and the transitions between the two logical states $|0_t\rangle$ and $|1_t\rangle$ are mediated by the virtual excitation of the short-lived state $|P_t\rangle$, introducing errors due to the fast decay rate γ_P. Moreover, because the control atom occupies the $|R\rangle$ state during the evolution, the overall error probability is further increased.

Consequently, the error-biased feature of the EIT-based Rydberg gate can be simply understood as a result of three factors when the control condition is not satisfied (i.e., the control atom is in initially in the $|0_c\rangle$ state): (i) the control atom is never excited to a short-lived Rydberg state, (ii) the $|P_t\rangle$ population is eliminated, and (iii) the occupation of the Rydberg state $|R_t\rangle$ can be reduced through the parameter $x^2 \ll 1$. Hence, we expect $\eta_\epsilon \propto x^2$. As indicated in Sec. V A, η_ϵ will decrease when we take into account the technical errors that are relevant when the $|P\rangle$ and $|R\rangle$ states of the target atoms are occupied. Indeed, the recent realization of the EIT-based CNOT gate in Ref. [96] demonstrated the presence of an error bias of $\eta_\epsilon^{-1} \approx 1.5$ even when the technical errors resulted in an overall gate fidelity of 0.55. While a detailed analysis of the error processes relevant for this particular experimental realization is out of the scope of our work, we suspect that both the overall error probability as well as η_ϵ^{-1} can be drastically increased by improving the quality of the laser drives and increasing Ω_p and Ω_c. Next, we support the above claims using analytical estimations as well as numerical calculations of the error probability defined in Sec. V E.

Analytic estimates of input conditional error probabilities. Let us first briefly discuss the results of a perturbative analysis of the dissipative evolution that results in the single-qubit controlled Pauli operations. Detailed derivations and analysis of the model that we used here can be found in Appendix B. Here, we focus solely on the errors that occur during the second step of the implementation.

The error probability when the control condition is not satisfied is given by the population of the target Rydberg state

$$\epsilon_v^{\rm inc} \approx \tau_g \tilde{\gamma}_R x^2, \tag{24}$$

where τ_g is the duration of the gate, which is determined by the effective Rabi frequency $\tilde{\Omega} \propto \frac{1}{\tau_g}$ of the transition between $|0_t\rangle$ and $|1_t\rangle$, given by

$$\tilde{\Omega} \approx \frac{|\Omega_p^{\max}|^2}{2\Delta}\left(1 + \frac{|\Omega_c|^2}{4\Delta J}\right), \tag{25}$$

in the case of $\Delta > 0$. We emphasize that here the decay rate $\tilde{\gamma}_R$ includes radiative decay processes including BBR-induced transitions, as well as other technical error mechanisms that become relevant when the target atom occupies the Rydberg state. In Appendix B, we consider the error probability due to the fluctuations in the energy of the target Rydberg states, which can be caused by fluctuations in the frequency of the control laser, or due to the dipolar interactions between the target qubits. We find that given a maximum energy shift δE, the error probability scales with $\tau_g \delta E x^2$, and hence can be included into $\tilde{\gamma}_R$. On the other hand, when the energy shift is caused by the dipolar interactions of strength $J_{\rm tt}$ between neighboring target atoms in their Rydberg states, then the error scales as $\tau_g J_{\rm tt} x^4$. The diabatic corrections associated with the probe pulse, which are proportional to x^6 and are neglected in the following discussion (see Ref. [60] and Appendix B for a more detailed discussion).

On the other hand, when the control condition is satisfied, there are multiple contributions to the error probability due to incoherent processes

$$\epsilon_s^{\rm inc} \approx \tau_g\left[\left(\frac{\Omega_p^{\max}}{\Delta}\right)^2 \frac{\gamma_P}{2} + \tilde{\gamma}_R + \left(\frac{|\Omega_c|^2}{4\Delta J}\right)^2 x^2 \tilde{\gamma}_R\right], \tag{26}$$

where the first term in the brackets is the radiative decay probability from the intermediate state $|P\rangle$ of the target atom, which can be approximated as $\sim\gamma_P/\Delta$. The second and the third terms in the brackets correspond to the errors due to the occupation of the Rydberg state of the control and the target atoms, respectively. Our numerical results, which use experimentally relevant parameters, show that out of the three contributions above, the error due to the decay processes affecting the Rydberg state of the control atom is dominant.

Numerical demonstration of the error bias using realistic parameters. We numerically verify the biased error characteristic of the EIT-based single-qubit controlled Pauli operation using realistic values for the relevant lifetimes and dipolar interaction strengths. To determine the maximum suppression of errors, we use the reported values for the lifetimes $\tau_R = 146$ μs for the Rydberg state $|n = 70, J = \frac{1}{2}, m_j = -\frac{1}{2}\rangle$ and $\tau_P = 115$ ns for the intermediate state $|n = 6P_{3/2}, F = 3, m = -3\rangle$ [12].

We consider a simple scenario for implementing the single-qubit controlled Pauli operation on multiple target atoms, where Ω_c, Δ, and $\Omega_p^{\max}$ are kept spatially constant, although the width of the pulse profile $\Omega_p(t)/\Omega_p^{\max}$ can be spatially dependent. We determine the maximum error ϵ_s and the error bias η_ϵ as we increase $J \geqslant J_{\min}$. Thus, it is conceivable that the numbers reported here can be further improved by allowing spatial variations in Ω_c, Δ, and $\Omega_p^{\max}$. However, such spatial control may prove challenging when the spacing between the atoms is small.

We pick the minimal dipolar interaction strength to be $J_{\min}/2\pi = 20$ MHz, which in turn determines the largest distance between the control and the target qubits. In particular, it is possible to achieve such interaction strengths at distances of about 7–8 μm using resonant dipolar interactions and Rydberg states with principal quantum numbers <100 [51,83].

Let us briefly discuss the choice of the other free parameters Ω_c, $\Omega_p^{\max}$, and Δ. The parameter $\Omega_c/2\pi = 120$ MHz is chosen as large as possible without requiring drastic improvements in the lasers conventionally used in the experiments. Given Ω_c, we choose $\Omega_p^{\max}/2\pi = 20$ MHz. While the rough discussion above suggests that this choice would only result in $\eta_\epsilon = \frac{1}{18}$, we find that η_ϵ can be up to an order of magnitude larger (see Fig. 4). The main reason for such an increase in the error-bias parameter η_ϵ is that when the control condition is satisfied, the control atom occupies the Rydberg state throughout the second step of the EIT-based gate, while the target atom is driven with an adiabatic pulse of strength $\Omega_p(t)$. Because the control atom should be in the Rydberg state during the duration of the adiabatic pulse, the errors due to the Rydberg occupation of the control atom dominate. More specifically, in our simulations, we use a Gaussian envelope of width $\sigma = 2\sqrt{\pi}\Delta/\tilde{\Omega}^2$, and pick $\tau_g = 7\sigma$ in

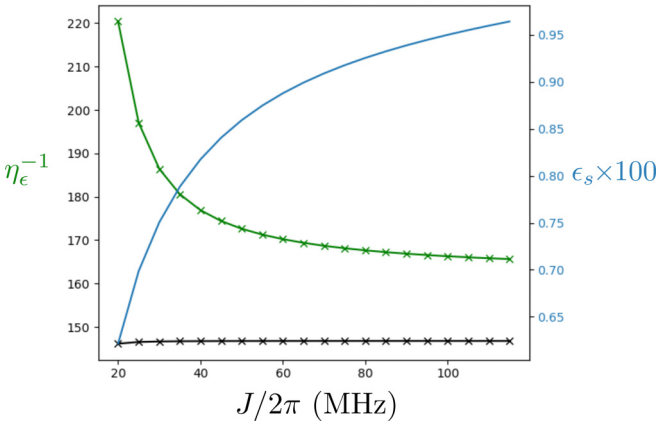

FIG. 4. The dependence of the total error-bias parameter η_ϵ (in green) and the error probability ϵ_s when the control condition is satisfied (in blue) as a function of the dipolar interaction strength. The detuning Δ is chosen to keep errors due to the fluctuations ΔJ in the strength of the dipolar interactions between the control and the target atoms below 0.1% at a distance of 8 μm. We also depict the ratio of the errors due only due to the occupation of the control and target Rydberg states in black. The pulse length is adjusted for each J according to Eq. (25). The remaining system parameters are $\Delta/2\pi = 300\,\text{MHz}$, $\Omega_c/2\pi = 120\,\text{MHz}$, and $\Omega_p^{\max}/2\pi = 20\,\text{MHz}$.

order to avoid the coherent errors in the rotation angle of the target qubit.

Finally, the detuning Δ is set such that the dipolar interaction strength $J > |\Omega_c|^2/4\Delta \equiv \Delta E_{\text{AC}}$, where ΔE_{AC} is the AC Stark shift caused by the strong drive amplitude Ω_c. Intuitively, it is desirable to operate in the regime $J \gg E_{\text{AC}}$, such that we are in the blockade regime and the Rydberg state becomes irrelevant to the evolution of the system when the control condition is satisfied. We observe this trend in Fig. 4, where as J increases, the dependence of both η_ϵ and ϵ_s on J decreases. On the other hand, as J approaches E_{AC}, we see that the EIT-based gate performs better. In particular, in the regime $J \gtrsim E_{\text{AC}}$ η_ϵ increases and ϵ_s decreases. The reason for this improvement is the increase in the effective Rabi frequency $\tilde{\Omega}$ indicated by Eq. (25), given both Δ and J have the same sign.

Yet, the apparently improved performance of the EIT-based gate comes at an important cost. Specifically, in the regime $J \gtrsim E_{\text{AC}}$ the effective Rabi frequency $\tilde{\Omega}$ becomes dependent on the strength J of the dipolar interactions. Consequently, fluctuations ΔJ in the dipolar interaction strength can potentially be detrimental to the gate fidelity. However, recent experiments have demonstrated that the main source of such fluctuations can be drastically reduced. Specifically, Ref. [93] has shown that positional uncertainties ΔR of about 10 nm are achievable on a scalable platform by combining large aperture lenses for the optical tweezer array with Raman sideband cooling [91,92]. For dipolar interactions with $J \propto 1/R^\alpha$, an uncertainty ΔR in the distance translates to $\Delta J/J = \alpha \Delta R/R$, implying that the effect of ΔJ can be drastically reduced. We emphasize that the fluctuations ΔJ would likely increase the bias parameter η_ϵ because they result in errors only when the control condition is satisfied. For the data presented in Fig. 4 we use $\Delta/2\pi = 300\,\text{MHz}$, which ensures that the maximum fluctuations in $\tilde{\Omega}$ obey $\frac{\Delta\tilde{\Omega}}{\tilde{\Omega}} < 0.5\%$ for $\Delta R = 10$ nm and $R = 8$ μm.

Generalization to multiple target and control qubits. The multitarget generalization of the EIT-based controlled unitary is obtained by simply increasing the number of target qubits within the blockade radius of the control qubit. Although in this scenario the interactions between the target atoms may result in additional errors of the gate, such errors are reduced dramatically because the probability that two target atoms simultaneously occupy the Rydberg state is proportional to x^4 [60]. Hence, given that the target atoms are tightly packed with an interatomic distance of 3 μm [93], we envision that our calculations are relevant for up to 30 target atoms, assuming that additional dressing techniques [94] can be used to ensure that the interactions between the target atoms become negligible compared to the interactions between the single-control atom and the target atoms. That said, for many applications of the QSP, and especially for the implementation of k-local Hamiltonian simulation where k is a small number, the number of target atoms is small. For instance, considering only 2-local terms, we could place the target atoms at a distance of 16 μm while keeping the target-to-control distance of 8μm. Together with the fact that the double-occupation probability scales with x^4, the errors due to the van der Waals interactions between the target atoms become negligible. In these applications, it may be more advantageous to simply transport a small number of target atoms in the close vicinity of the target atom and back [29].

In the proposed error-robust implementations of W, especially for the implementation of the reflection operator $\mathbf{I} - 2\Pi_0$, we also use multicontrol single-target unitaries, whose error characteristics have been extensively studied in Refs. [5,97]. Consider the case where the multibit control condition is given as the all-zeros state and the desired operation on the single target qubit is a NOT gate. To implement this unitary, we first simultaneously excite each control qubit in the $|1\rangle$ state to the Rydberg state. In the second step, we apply a NOT gate on the target atom following the pulse sequence in Fig. 3. When the control condition is satisfied, none of the control atoms are excited to the Rydberg manifold, and the NOT operation is applied. On the other hand, if the control condition is not satisfied, the target atom goes through a trivial evolution. Unlike the EIT-based single-qubit controlled unitary, the multiqubit controlled unitary results in a Rydberg excitation in either the control or the target register independently of the control condition. Yet, the EBGC of the protocol still depends crucially on the state $|\psi_c\rangle$ of the control qubits. In particular, when the control condition is the all-zeros state, the number of Rydberg excitations in the control register is the average number of control qubits in the $|1\rangle$ state. When multiple control qubits are excited to the Rydberg state, the residual interactions between the control qubits may result in further errors. However, we emphasize that unlike earlier studies of multiqubit controlled-NOT gates on the Rydberg atom platform [5,97], we apply multiqubit controlled unitaries only in situations where the control register has only a constant number of qubits in the $|1\rangle$ state (see Sec. VI B). Better still, such residual interactions between the control qubits can be eliminated using additional microwave pulses [94].

D. One-hot amplitude encoding gate

In the following, we introduce the one-hot amplitude encoding gate $V_{1\mathrm{HE}}$, which is at the core of the state preparation unitary of the LCU protocol described in Sec. IV. $V_{1\mathrm{HE}}$ can be thought of as a generalization of the single-qubit gate where long-range Rydberg interactions constrain the many-body Hilbert space relevant for the evolution to a *two-dimensional* subspace. Such constrained dynamics emerging from the long-range dipolar interactions has been an important focus in the literature [3,5,21,98]. For our discussion, the most important similarity between the single-qubit gate and the one-hot encoding gate is that they can both be used to store classical information that is encoded in the duration t_0 and the amplitude Ω of the laser drive in quantum-mechanical degrees of freedom. More specifically, the single-qubit rotation loads a single amplitude $\alpha \equiv \arcsin(\Omega t)$ on a single qubit. Similarly, the one-hot amplitude encoding gate $V_{1\mathrm{HE}}$ is a way of loading M amplitudes $\{\alpha_i\}$ where $\alpha_i \propto \Omega_i$ into M qubits in constant time. Because our scheme encodes each $\{\alpha_i\}$ as amplitudes of a computational basis states with only one excitation (i.e., one qubit in the $|1\rangle$ state), we refer to it as the one-hot amplitude-encoding gate. From a physical point of view, the $V_{1\mathrm{HE}}$ gate loads the information encoded in the relative local intensity of the laser field into orthogonal computational basis states of a quantum register.

To better understand how $V_{1\mathrm{HE}}$ can be implemented, consider M closely spaced atoms such that the energy of the Rydberg state of each atom is shifted by *at least* J due to the presence of the other atoms occupying their Rydberg state. If we then drive this system using M lasers whose frequency is resonant with the $|0\rangle \leftrightarrow |R\rangle$ transition and whose amplitudes $\{\Omega_0\alpha_i\}$ satisfy $(\Omega_0/J)^2 \ll 1$, the dynamics of the system results in a nontrivial transformation of only a two-dimensional subspace spanned by

$$|0\rangle^{\otimes M} \quad \text{and} \quad \sum_i \alpha_i |1\mathrm{HE}^{(R)}, i\rangle \equiv |1\mathrm{HE}^{(R)}\rangle,$$

where $\sum_i |\alpha_i|^2 = 1$ and we omit the $\{\alpha_i\}$ the definition for simplicity. Here we define the one-hot encoding basis states $|1\mathrm{HE}^{(R)}, i\rangle \equiv |0\ldots 0R_i 0\ldots 0\rangle$, each of which has only one Rydberg excitation. Under these conditions, it is convenient to project the drive Hamiltonian $H_d = \sum_{i=1}^{M} \Omega_0\alpha_i\sigma^+ + \mathrm{H.c.}$ onto subspace given above, and work with the effective Hamiltonian

$$\bar{H} \equiv P_1 H_d P_1 = \Omega_0 \left(\sum_{i=1}^{M} \alpha_i |1\mathrm{HE}^{(R)}, i\rangle \right) \langle 0^{\otimes M}| + \mathrm{H.c.}, \quad (27)$$

which is analogous to a Pauli operator in the constrained Hilbert space (notice $\bar{H}^2 = \mathbf{1}$). A schematic for the implementation of $V_{1\mathrm{HE}}$ is given in Fig. 5.

Given the initial state $|0\rangle^{\otimes M}$, evolving the system under $\bar{H}$ for time $t^* = \frac{\pi}{|\Omega_0|}$ prepares the following one-hot encoding state:

$$\begin{aligned} U_{0R}|0\rangle^{\otimes M} &= e^{-it^*\bar{H}}|0\rangle^{\otimes M} \\ &= \sum_{i=1}^{M} \alpha_i |1\mathrm{HE}^{(R)}, i\rangle \equiv |1\mathrm{HE}^{(\mathrm{R})}\rangle. \end{aligned} \quad (28)$$

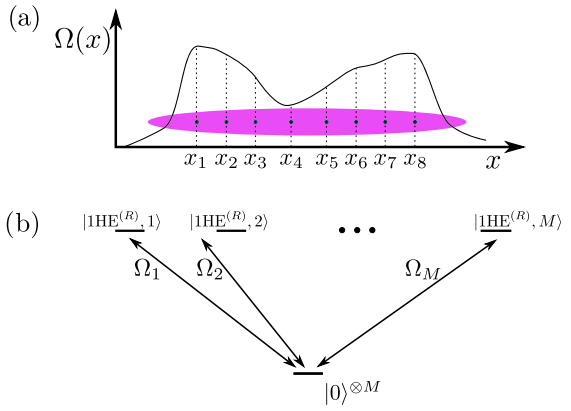

FIG. 5. (a) The experimental scheme for implementing $V_{1\mathrm{HE}}$. All atoms are within each other's blockade radii. The spatial dependence of the drive amplitude is utilized to encode complex-valued classical data stored in the laser amplitudes $\Omega_i \equiv \Omega(x_i)$ into a quantum register. (b) The relevant level diagram of M Rydberg atoms for the configuration in (a). The one-hot encoding computational basis states $|1\mathrm{HE}^{(R)}, i\rangle$ have a single Rydberg excitation on the ith atom.

Notice that when each atom is driven by an independent laser of fixed amplitude, the time to implement U_{0R} scales as $O(1/\sqrt{M})$ due to collective enhancement [21]. Yet, for our constructions, the run time of the one-hot encoding gate remains constant if we require that $V_{1\mathrm{HE}}$ maps the states in the long-lived logical subspace back to the same subspace. This requirement can be fulfilled by simply conjugating U_{1R} by a π pulse between the $|1\rangle$ and $|R\rangle$ states of each atom, as implemented by the following evolution operator:

$$U_{\sigma R} = \exp\left(it_1^* \sum_{i=1}^{M} (\Omega_1 |R_i\rangle\langle\sigma_i| + \mathrm{H.c.}) \right), \quad (29)$$

where $\sigma = \{1, r\}$ and $t_1^* = |\frac{\pi}{2\Omega_1}|$. Notice that, unlike t^*, the time t_1^* to implement $U_{\sigma R}$ does not take advantage of the collective enhancement resulting from the blockade interaction. As a result, the time to implement $V_{1\mathrm{HE}}$ is constant, assuming that the blockade radius is larger than the system size.

The action of the resulting unitary on the logical subspace can be clearly expressed as

$$V_{1\mathrm{HE}} \equiv U_{1R}U_{0R}U_{1R}^\dagger \approx i(|1\mathrm{HE}\rangle\langle 0|^{\otimes M} + \mathrm{H.c.}) + \Pi_{\neq 1\mathrm{HE},0},$$

where $|1\mathrm{HE}\rangle \equiv \sum_i \alpha_i |1\mathrm{HE}, i\rangle$ and $|1\mathrm{HE}, i\rangle$ denotes the bit string where all qubits except the ith qubit are in the $|0\rangle$ state and the ith qubit is in $|1\rangle$ state. $\Pi_{\neq 1\mathrm{HE},0} = \mathbf{I} - |1\mathrm{HE}\rangle\langle 1\mathrm{HE}| - |0\rangle\langle 0|^{\otimes M}$ is the orthogonal projector whose kernel is spanned by $|0\rangle^{\otimes M}$ and $|1\mathrm{HE}\rangle$. Crucially, assuming perfect blockade, $V_{1\mathrm{HE}}$ results in a trivial evolution of all states other than $|0\rangle^{\otimes M}$ and $|1\mathrm{HE}\rangle$.

Here we do not give a detailed discussion of the errors for implementing the $V_{1\mathrm{HE}}$ gate, as this has been widely discussed in the literature. Instead, we give a brief review of previous results [21,99–101], and provide numerical simulations only for the controlled version of $V_{1\mathrm{HE}}$. Because we have at most one atom in the Rydberg state during the implementation of $V_{1\mathrm{HE}}$, the errors due to the radiative decay mechanism are the same as those associated with a single-qubit gate where the initial $|0\rangle$ state is completely transferred to the $|1\rangle$ state [100].

On the other hand, the nonadiabatic errors resulting from the finite value of the strength J of dipolar interactions grow as $O[(\Omega_0/J)^2]$ [21,99], which only contributes a constant error probability because $O(\Omega_0) = O(1)$, as explained in the previous paragraph. Finally, we emphasize that because we are in the blockade regime, the fluctuations in the dipolar interaction strength between atoms do not have a strong influence on the error probability. Reference [101] experimentally demonstrated the preparation of a symmetric one-hot encoding state consisting of up to about 100 atoms (also referred to as the W state or the one-excitation Dicke state). Although the use of one-hot encoding states for computation requires higher fidelities than reported in these works, recent progress in the control of Rydberg atoms [29,93] gives us confidence that the methods described here will be applicable in near-term quantum systems consisting of trapped neutral atoms.

1. Utilizing k-hot amplitude encoding states through CV_{1HE} gates

As discussed in Sec. V, achieving an error-robust implementation of QSP requires the preparation of address states which are superpositions of products of one-hot bit strings. In Sec. VI A we describe error-robust preparation of such states using error-biased single-qubit controlled-$V_{1\mathrm{HE}}$ (denoted $\mathrm{C}V_{1\mathrm{HE}}$). Here, we provide the details of implementing a single $\mathrm{C}V_{1\mathrm{HE}}$ and report numerical evidence of its biased-error characteristics.

Unlike the situation with the tensor products of Pauli operators, a controlled version of the $V_{1\mathrm{HE}}$ gate is challenging because $V_{1\mathrm{HE}}$ utilizes interactions between the Rydberg states amongst all atoms. Thus, we need to introduce a mechanism to implement $CV_{1\mathrm{HE}}$. Our strategy is to use the interactions between the target atoms to our advantage. To implement a controlled version of $V_{1\mathrm{HE}}$, we consider a situation where the target atoms are all in each other's blockade radius. Moreover, we utilize two types of Rydberg states: (i) the Rydberg state $|R\rangle$ utilized in the implementation of $V_{1\mathrm{HE}}$ in Sec. V D and (ii) an additional Rydberg state $|R_p\rangle$ which is utilized to implement the EIT-based controlled version of $V_{1\mathrm{HE}}$. Importantly, the angular momentum quantum numbers of $|R\rangle$ and $|R_p\rangle$ are different, such that the two states experience different energy shifts resulting from dipolar interactions with the control atom. This allows the Rydberg population of a control atom to disturb the two-photon resonance condition on the target atoms without blocking the preparation of the $|1\mathrm{HE}^{(\mathrm{R})}\rangle$ state.

The implementation of the $CV_{1\mathrm{HE}}$ gate, the dynamics of the target register can be described by a five-level system depicted in Fig. 2. There, the states $|1\mathrm{HE}^{(\eta)}\rangle$ denote one-hot amplitude encoding states with the excited state in the $|\eta\rangle \in \{|1\rangle, |R\rangle, |P\rangle, |R_p\rangle\}$. The gate protocol based on an EIT scheme is similar to the one discussed in Sec. V C, where $|0\rangle^{\otimes n_t}$ and $|1\mathrm{HE}^{(\mathrm{R})}\rangle$ replace the two hyperfine states in the implementation of the EIT-based controlled Pauli gate, and the intermediate state of the EIT scheme is the one-hot encoding state $|1\mathrm{HE}^{(\mathrm{P})}\rangle$. Finally, the state which controls whether the EIT condition is satisfied is $|1\mathrm{HE}^{(\mathrm{R_p})}\rangle$. In short, the $CV_{1\mathrm{HE}}$ is implemented as a transition between $|0\rangle^{\otimes n_t}$ and $|1\mathrm{HE}^{(\mathrm{R})}\rangle$ controlled by the energy shift of $|1\mathrm{HE}^{(\mathrm{R_p})}\rangle$.

Numerical simulations with two target atoms indicate that the $CV_{1\mathrm{HE}}$ gate behaves identically to the EIT-based single-qubit controlled Pauli operation when as long as the collective Rabi frequency between the $|0\rangle^{\otimes n_t}$ and $|1\mathrm{HE}^{(R)}\rangle$ state remains much slower than the interaction strength between the target atoms. Taking the interaction strength between the target Rydberg states equal to that between the target and control Rydberg states (i.e., $J_{ct} = J_{tt} = 2\pi \times 30\,\mathrm{MHz}$), we find that the $CV_{1\mathrm{HE}}$ can be implemented with the same values of Ω_c and Δ for each target atom, if we reduce $\Omega_p \leftarrow \Omega_p/2^{1/4}$. The recalibration of the probe amplitude is necessary because of the $\times\sqrt{2}$ collective enhancement of the two-photon transition between the initial $|00\rangle$ to $\frac{1}{\sqrt{2}}(|0R\rangle + |R0\rangle)$ in the target register. The resulting error-bias parameter $\eta_\epsilon \approx \frac{1}{156}$ is larger than that of the controlled Pauli gate discussed in Sec. V C, because of the larger overlap between the initial state $|00\rangle$ and the bright state $\frac{1}{\sqrt{3}}(\sqrt{2}|00\rangle + \frac{1}{\sqrt{2}}(|0R\rangle + |R0\rangle))$ when the probe field Ω_p is turned off. The error probability when the control condition is satisfied $\epsilon_s = 0.85\%$ is slightly larger than that of the single-qubit controlled Pauli operation because of the nonzero decay rate of the Rydberg states $|R\rangle$. We expect that η_ϵ to grow as we increase the number of target qubits because of the overlap between the initial state $|00\rangle$ and the bright state. Yet, this will result in at most an error-bias parameter twice as large in the limit of large n_t. The most important experimental challenge is to make sure that the $|R\rangle$ states in the target register do not interact strongly with the Rydberg state of the control atom, while $|R_p\rangle$ states do.

E. Error-bounded gate count for the Rydberg platform

In the following, we define the error-bounded gate count (EBGC) as a convenient tool to quantify the error probability associated with the implementations of complex circuits. In particular, EBGC allows us to determine the growth of error probability as a function of scaling variables n_{site} and N, without the need to numerically simulate large systems.

In particular, EBGC (denoted n_U for a unitary operation U) codifies each unitary discussed in the previous subsection by assigning them an error probability that is a simple fraction of the error probability of a single CNOT gate. Thus, as we detail below, EBGC is inevitable based on an idealization of the Rydberg atom gates proposed in this work. Still, together with the subadditivity property of the input biased-error probability (see Sec. II E), the EBGC allows us to *count* the total error probability of a QSP protocol in units of the error probability associated with a single CNOT gate. EBGC also assigns a depth count (denoted d_U for a unitary U) to each implemented gate in units of t_{step}, taken to be the time it takes to achieve a complete state transfer between the hyperfine and Rydberg manifolds.

Three factors determine the EBGC: (i) the rotation angle of single-qubit rotations, (ii) the dimensionality of the local Hilbert space of each Rydberg atom, and (iii) the dependence of the error probability on the state of the control qubit. In the following, we assign an EBGC to each gate discussed in Sec. V based on these three factors.

Single-qubit gates. Our protocols use a continuous family of gates, such as single-qubit rotations by an arbitrary angle.

TABLE I. The EBGCs for the native gates of the Rydberg system that are discussed in Sec. V. All gate counts are normalized by the maximum error probability of a single CNOT gate. The input state of the control and target registers are $|\psi_c\rangle$ and $|\psi_t\rangle$, respectively, and θ is the single-qubit rotation angle. Most importantly, the cost of single-qubit-controlled unitaries depends on the probability that the control condition is satisfied.

	R_θ	$V_{1\text{HE}}$	$CX_1^R \dots X_k^R$	$CV_{1\text{HE}}$	$CU_1 \dots U_k$
EBGC	$\lvert 2\theta/(3\pi)\rvert$	1	$2/3\lvert\langle 1_c\rvert\psi_c\rangle\rvert^2(1+\lvert\langle 1_t\rvert\psi_t\rangle\rvert^2)$	$5/3\ \lvert\langle 1_c\rvert\psi_c\rangle\rvert^2$	$(2+k)/3\lvert\langle 1_c\rvert\psi_c\rangle\rvert^2$
Depth	$\lvert 2\theta/\pi\rvert$	2	4	5	3

Consider the single-qubit rotation

$$R_\theta|0\rangle \equiv \cos(\theta)|0\rangle + \sin(\theta)|1\rangle, \tag{30}$$

the error associated with implementation of R_θ on the Rydberg atom platform is proportional to $|2\theta/\pi|$. More precisely, we assign an EBGC of $|\frac{2\theta}{3\pi}|$ to R_θ. Notice that this rule associates $\frac{1}{3}$ error-bounded gates (in units of the error probability of a CNOT gate) for each single-qubit Pauli operator. On the other hand, the depth of the single-qubit unitary is $2\theta/\pi$, such that a $\pi/2$ rotation has depth 1.

The error-robust protocols discussed in this work take advantage of the fact that each Rydberg atom has more than two long-lived states. A local Hilbert space of more than two dimensions entails that the experimentalist can choose laser pulses which approximately act on a two-dimensional subspace of the local Hilbert space. The EBGC assumes the idealized scenario where this approximation, which is especially valid for weakly driven atomic systems, holds. Hence, EBGC counts errors only when the atom is in a state with a nonzero overlap with the subspace influenced by the laser pulse. Consider as an example a laser pulse sequence implementing the unitary that transfers an atom from the logical hyperfine state $|1\rangle$ to the Rydberg state $|R\rangle$ (the level diagram associated with each atom is discussed in more detail in Sec. V A). Given the initial state $|\psi\rangle = \sqrt{1-|\alpha|^2}|0\rangle + \alpha|1\rangle$, the unitary has an EBGC of $1/3|\alpha|^2$ error-bounded gates.

Controlled Pauli gates. The EBGC assignment of CP_i is assessed in accordance with a physical error model in the limit that the error bias is perfect (i.e., $\eta_\epsilon = 0$). The error probability is the sum of those associated with the control and target registers. For the operation where the input control state is $|\psi_c\rangle = \alpha|1\rangle_c + \sqrt{1-|\alpha|^2}|0\rangle$, then the associated EBGC is $|\alpha|^2$.

The knowledge of the target register's state can also be used to reduce the EBGC of controlled unitaries. For example, consider the implementation of a single-qubit controlled unitary $CX^{(R)}$ which transfers the target atom from $|1\rangle$ to $|R\rangle$ conditioned on the state of a control atom. Given the input state $|\psi_c\rangle = \sqrt{1-|\alpha|^2}|0_c\rangle + \alpha|1_c\rangle$ and $|\psi_t\rangle = \sqrt{1-|\beta|^2}|0_t\rangle + \beta|1_t\rangle$, the EBGC of the controlled unitary is $2/3|\alpha|^2(1+|\beta|^2)$ for a single target qubit. The depth of the implementation is 4 (see Fig. 3 for the pulse sequence).

Extending EBGC for single-control multitarget unitaries of the form $CU_1 \dots U_k \equiv CP_i$ is straightforward. In this case, given $|\psi_c\rangle = \sqrt{1-|\alpha|^2}|0_c\rangle + \alpha|1_c\rangle$ and assuming no knowledge of the state of the target register, the error introduced into the target register is $n_{CP_i} = \frac{2+k}{3}|\alpha|^2$, where the first and the second terms stand for the errors from the control and target atoms, respectively. Finally, considering a multicontrol single-target Pauli operation where the control condition is the all-zeros state, and a control register whose input state has on average k qubits in the $|1\rangle$ state, the associated EBGC is $\frac{1}{3}(1+k)$, assuming that the dipolar interactions between the control atoms can be eliminated. The depth of the implementation is 3. We emphasize again that the multiqubit controlled unitary is not necessary for implementation that is robust to gate-induced errors, but it is helpful in reducing the depth of the implementation. As before, the EBGCs are subject to modification when the state of the *target* register is known.

$V_{1\text{HE}}$. Using the construction of the $V_{1\text{HE}}$ in Sec. V D and considering its action on only one-hot encoding states, the EBGC assignment is 1. Given the EBGC for $V_{1\text{HE}}$, the EBGC of $CV_{1\text{HE}}$ given the control qubit in $|\psi_c\rangle = \sqrt{1-|\alpha|^2}|0\rangle + \alpha|1\rangle$ is $n_{V_{1\text{EH}}} = 5/3|\alpha|^2$. The depth of the implementation is 5, including the two transfer unitaries in Eq. (30).

The gate counts are summarized in Table I, for a given input state $|\psi_c\rangle$ of the control register and the control condition $|1_c\rangle$.

We conclude this section by emphasizing that the EBGC not only assesses an experimental scenario but also guides us to design algorithms with lower EBGC by taking full advantage of the structure of the errors relevant for that experimental scenario. More specifically, EBGC allows us to demonstrate that the structure of the errors relevant to the proposed Rydberg atom gates can be leveraged to design error-robust implementations of quantum algorithms. EBGC is especially convenient when the numerical simulation of multiqubit gates becomes difficult.

VI. ERROR-ROBUST IMPLEMENTATION OF QSP PROTOCOLS

In this section, we describe protocols for error-robust implementations of LCU-based QSP iterates, using the Rydberg atom gates described in Sec. V. In these implementations, the ancillary register uses address states $|x_i\rangle$ (see Sec. IV) that are in the span of product states of k one-hot amplitude encoding states. We refer to these as k-hot encoding states. The resulting implementation of CW has an EBGC scaling as $O(k)$ when the block-encoded operator A is a linear combination of k-local Pauli strings acting on n_{site} qubits. The size ancilla register, on the other hand, grows only linearly with k.

In Sec. VI A, we present the k-hot encoding state preparation unitary based on $CV_{1\text{HE}}$ gates (see Sec. V D 1), which efficiently prepares ancillary states for an error-robust implementation of LCU-based block encoding. In Sec. VI B, we discuss the implementation of $\bar{U}$ that complements the state-preparation protocol in Sec. VI A. Finally, in Sec. VI B, we calculate the EBGC for CW.

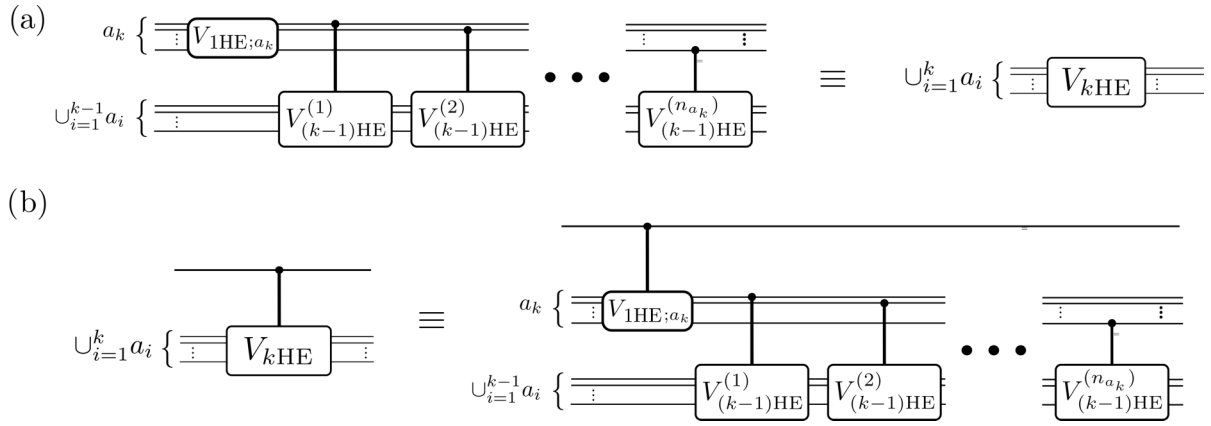

FIG. 6. (a) The recursion relation for constructing the k-hot encoding state-preparation unitary. (b) The building block of the k-hot amplitude encoding state-preparation unitary. At each step of the state preparation only single-qubit controlled one-hot encoding gates $CV_{1\mathrm{HE}}$ are used.

A. Implementation of state-preparation unitary V

We demonstrate that it is possible to implement k-hot encoding state-preparation unitaries with an EBGC that grows logarithmically with the number of address states, using only $V_{1\mathrm{HE}}$ gates and their single-qubit-controlled counterpart $CV_{1\mathrm{HE}}$.

As a first step, we describe a state-preparation protocol that uses 2 ancilla registers a_1 and a_2 of size n_{a_1} and n_{a_2}, respectively; and prepares the following 2-hot encoded state (the associated unitary is denoted as $V_{2\mathrm{HE}}|0\rangle^{\otimes n_{a_1}+n_{a_2}} \equiv |\Psi_{2\mathrm{HE}}\rangle$):

$$|\Psi_{2\mathrm{HE}}\rangle = \sum_{l=1}^{n_{a_1}} \beta_l^{(1)} |1\mathrm{HE}, l\rangle \otimes \left(\sum_{i=1}^{n_{a_2}} \beta_i^{(2;l)} |1\mathrm{HE}, i\rangle \right), \quad (31)$$

where $\beta_i^{n;l}$ is the coefficient of the state $|1\mathrm{HE}, i\rangle$ of the nth ancillary register a_n, conditioned on the $(n-1)$st ancilla register being in the state $|1\mathrm{HE}, l\rangle$. The circuit that implements $V_{2\mathrm{HE}}$ is depicted in Fig. 6. We implement the state-preparation unitary by first applying $V_{1\mathrm{HE},a_1}$ on the first ancilla register. Then, for each $l \in (1, \ldots, n_a)$, we apply $V^{(l)}_{1\mathrm{HE}}$ on the second ancilla register conditional on the lth qubit in a_1 being in state $|1\rangle$ (we denote such an operation as $C_{1;a_1,l} V^{(l)}_{1\mathrm{HE};a_2}$). Here, $V^{(l)}_{1\mathrm{HE}}$ denotes the one-hot encoding unitary associated with the set of probability amplitudes $\{\beta_i^{(2,l)}\}$ for $i = (1, \ldots, n_{a_2})$. The state-preparation protocol requires $n_{\mathrm{tot}} = n_{a_1} + n_{a_2}$ ancillary qubits and has an EBGC of only

$$n_{V_{2\mathrm{HE}}} = \frac{1}{3}\left(3 + 5\sum_{l=1}^{n_{a_1}} \left|\beta_l^{(1)}\right|^2\right) = 8/3.$$

In the calculation of EBGC, the first term is the EBGC of the $V_{1\mathrm{HE},a_1}$, and the second term is that of n_{a_1} controlled one-hot amplitude encoding unitaries. The depth of the protocol is $3 + 5n_{a_1}$ (see Sec. V E) for details.

In order to implement the single-qubit controlled version of $V_{2\mathrm{HE}}$, we use the auxiliary hyperfine state $|r\rangle$ of each atom (see Sec. IV C). In particular, our strategy is to transfer each atom in a_1 from $|1\rangle$ to $|r\rangle$ conditioned on the state of the exit ancilla being in $|0_{\mathrm{ex}}\rangle$. Hence, if the exit ancilla is $|0_{\mathrm{ex}}\rangle$, the control condition is not satisfied for all unitaries $\{C_{1;a_1,l} V^{(l)}_{1\mathrm{HE};a_2}\}$ that make up the state-preparation unitary. In order to avoid the $V_{1\mathrm{HE};a_1}$ to cause any transitions from the all-zeros state to a state with any qubit occupying the $|1\rangle$ state, we also apply $V_{1\mathrm{HE};a_1}$ conditionally on the exit ancilla being in $|1_{\mathrm{ex}}\rangle$. The controlled transfer operation is uncomputed at the end of the protocol such that the resulting state is in the logical subspace. Such an implementation of controlled $V_{2\mathrm{HE}}$ results in an EBGC less than

$$n_{CV_{2\mathrm{HE}}} = n_{V_{2\mathrm{HE}}} + 2/3 + 2 = 16/3,$$

where the additional $\frac{2}{3}$ results from the controlled $V_{1\mathrm{HE};a_1}$ operation and the two controlled transfer operations result in an additional EBGC of 2. The depth of the implementation is $11 + 5n_{a_1}$

The preparation of the 2-hot encoding state clearly exhibits a space-time tradeoff, assuming that the blockade radius remains larger than the size of the ancillary register. When we prepare a state with N address components with $n_{a_1} = 1$, the protocol takes constant time, but the number of ancillae scales as $O(N)$. Increasing n_{a_1} by L results in a protocol that takes $O(L)$ time but the number of ancillae is $O(N/L)$. The space-time tradeoff can be made more advantageous for smaller ancillary registers if we encode the addresses in kHE states. In particular, the protocol for the preparation of the 2HE state above can be concatenated over k ancillary registers (see Fig. 6), of size n_j. The size of the ancillary address register grows linearly with k, while the number of address states grows as $\prod_{j=1}^{k} n_j$. If we set $n_j = n_{\mathrm{site}}$ for a system register of size n_{site}, the concatenated protocol requires $O(kn_{\mathrm{site}})$ ancillae $O(n_{\mathrm{site}}^{k-1})$ time, and encodes $O(n_{\mathrm{site}}^{k})$ amplitudes. More importantly for the discussion of error robustness, the EBGC of the state preparation of kHE states is

$$\begin{aligned} n_{V_{k\mathrm{HE}}} &= \frac{1}{3}\Bigg[3 + 5\sum_{l_{k-1}=1}^{n_{k-1}} \left|\beta_{l_k}^{(k-1)}\right|^2 \\ &\quad \times \left(5 + \sum_{l_{k-2}=1}^{n_{k-2}} \left|\beta_{l_{k-2}}^{(k-2;l_{k-1})}\right|^2 (5 + \overset{k-3 \text{ times}}{\cdots})\right)\Bigg] \\ &= \frac{3 + 5(k-1)}{3} = O(k), \end{aligned} \quad (32)$$

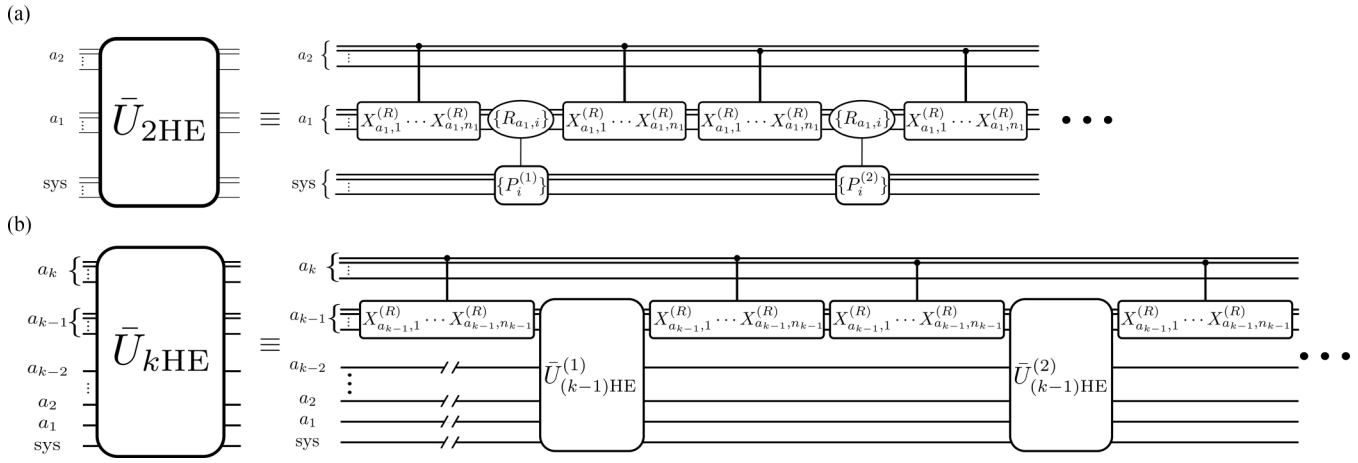

FIG. 7. The circuit diagrams for implementing the unitaries: (a) $\bar{U}_{2\mathrm{HE}}$ and (b) $\bar{U}_{k\mathrm{HE}}$. The ancillary registers are denoted as a_i. In (a), the conditional Pauli operations with the curly brackets indicate a parallelized application. The same building block is repeated n_{a_2} times to complete the application of $\bar{U}_{2\mathrm{HE}}$. In (b), we depict the concatenation of unitaries which results in the application of $\bar{U}_{k\mathrm{HE}}$. Although the circuit suggests that the atoms in a_l remain in the Rydberg manifold as we apply $\bar{U}_{l-1\mathrm{HE}}$, the atoms occupying the Rydberg state should be deexcited to the long-lived $|r'\rangle$ state, to achieve an error-robust implementation.

$$d_{V_{k\mathrm{HE}}} = 3 + 5\prod_{j=1}^{k-1} n_{a_j}, \tag{33}$$

where the depth can be calculated by simply counting the number of controlled $V_{1\mathrm{HE}}$ unitaries.

The prepared state is a product of k one-hot encoding states, each associated with a different ancillary register

$$|\Psi_{k\mathrm{HE}}\rangle = \sum_{l_1=1}^{n_1}\sum_{l_2=1}^{n_2}\cdots\sum_{l_k=1}^{n_k}\beta_{l_1}^{(1)}\beta_{l_2}^{(2;l_1)}\ldots\beta_{l_k}^{(k;l_{k-1})}\bigotimes_{j=1}^{k}|1\mathrm{HE}, l_j\rangle. \tag{34}$$

We emphasize that our protocol allows one to adjust the amplitude associated with each k-hot computational basis state, for instance, by using a regression tree decomposition of the sorted list of coefficients $\{\alpha_i\}$ [102]. The controlled version of $V_{k\mathrm{HE}}$ can be implemented using the same strategy used in the case of $V_{2\mathrm{HE}}$, and the total EBGC is

$$n_{\mathrm{C}V_{k\mathrm{HE}}} = \left(2+\tfrac{5}{3}\right)k = O(k).$$

In the above expression, the first term is the EBGC for the single-qubit controlled transfer operations (assuming that all k target registers encode one-hot encoding states), and we used Eq. (33) to obtain the total EBGC. The depth of the implementation is $d_{\mathrm{C}V_{k\mathrm{HE}}} = d_{V_{k\mathrm{HE}}} + 2 * 3 + 2$.

B. Implementation of $\bar{U}_{k\mathrm{HE}}$

When the control conditions are encoded in k-hot encoding basis states, $\bar{U}_{k\mathrm{HE}}$ can be implemented as a sequence of k-qubit controlled Pauli operations. Here, we give a protocol for an error-robust implementation of $\bar{U}_{k\mathrm{HE}}$ using only error-biased single-qubit controlled unitaries described in Sec. V C. The implementation has an EBGC of only $O(k)$ when the block-encoded operator can be decomposed in terms of k-local Pauli operators.

The unitary $U_{k\mathrm{HE}}$ can be implemented as a series of single-qubit controlled Pauli operations (see Fig. 7). When $k = 2$, $U_{2\mathrm{HE}}$ can be implemented by the following protocol. For each ancillary qubit l in the first ancillary register a_1, do the following:

(1) Apply $C_{a_{1l}}X^{(R)}_{a_{2,1}}\ldots X^{(R)}_{a_{2,n_l}}$ to excite the qubits in the second ancilla register to the Rydberg state conditionally on the state of the lth qubit in a_1 being in state $|1_{a_{1,l}}\rangle$.

(2) Apply $\{C_{R;a_{2,l}}P_i^{(l)}\}$ (in parallel whenever possible).

(3) Apply $C_{a_{1,l}}X^{(R)}_{a_{2,1}}\ldots X^{(R)}_{a_{2,n_l}}$.

Assuming all Pauli operators $P_i^{(l)}$ can be implemented in parallel, the implementation depth of the above protocol is $(2d_{CX^{(R)}}+1)n_{a_1} = 9n_{a_1}$. We note that the second step requires depth 1 as the control register is already excited to the Rydberg manifold. The EBGC is

$$\begin{aligned} n_{\bar{U}_{2\mathrm{HE}}} &= 1/3\sum_{l=1}^{L}\left|\beta_l^{(1)}\right|^2\left\{8+\sum_{i=1}^{n_{a_2}}\left[\left|\beta_i^{(2;l)}\right|^2\mathrm{supp}\left(P_i^{(l)}\right)\right]\right\} \\ &\leqslant \frac{1}{3}(8+k), \end{aligned} \tag{35}$$

where $\mathrm{supp}(P_i^{(l)})$ denotes the weight of the Pauli operator that is loaded in the address $|1\mathrm{HE}, l\rangle \otimes |1\mathrm{HE}, i\rangle$. It is important to emphasize that the EBGC of the two $C_{a_{1l}}X^{(R)}_{a_{2,1}}\ldots X^{(R)}_{a_{2,n_l}}$ operations is only $2\times 4/3$ (first term in curly brackets) because both ancillary registers are in one-hot encoding states (see Sec. V E). Moreover, notice that the probability that the control condition of any $C_{R;a_{2,l}}P_i^l$ is satisfied is multiplied by the probability that the control condition of the $C_{a_{1l}}X^{(R)}_{a_{2,1}}\ldots X^{(R)}_{a_{2,n_l}}$ is satisfied. In order to obtain the last equality, we used the assumption that the Pauli strings $\{P_i^l\}$ are k-local. We emphasize that the EBGC that does not scale with n_{site} or N, but only depends on the maximum weight of the multi-qubit Pauli operators in the decomposition of the block-encoded operator. Note also how we take advantage of the Rydberg state to avoid

introducing new ancillae in the implementation of a two-qubit controlled unitary [39].

As in the case of the controlled version of the state-preparation unitary, a single-qubit controlled version of $\bar{U}_{2\mathrm{HE}}$ can be implemented by simply transferring the ancillary control atoms in the $|1\rangle$ state to an auxiliary $|r\rangle$ state conditionally on the exit ancilla being in $|0_{\mathrm{ex}}\rangle$. Then, Condition 1 is satisfied because none of the control conditions of the controlled unitaries that make up $\bar{U}_{k\mathrm{HE}}$ are satisfied.

The above scheme can be extended to the case of k one-hot encoding ancillary registers [see Eq. (34)] using single-qubit controlled operations. Then the EBGC is increased by an additional factor of $O(k)$. In Fig. 7(b), we depict the circuit identity which recursively implements $\bar{U}_{k\mathrm{HE}}$. Considering a scheme where the atoms in their Rydberg states in the lth register are transferred to an auxiliary $|r'\rangle$ state when they are not needed, EBGC of $\bar{U}_{k\mathrm{HE}}$ conditioned on a kHE state, denoted by $n_{\bar{U}_{k\mathrm{HE}}}$, is given by

$$\frac{1}{3}\sum_{l_k=1}^{n_{a_k}}\left|\beta_{l_k}^{(k)}\right|^2\left(8+\sum_{l_{k-1}=1}^{n_{a_{k-1}}}\left|\beta_{l_{k-1}}^{(k-1;l_k)}\right|^2(8+\overset{k-2\,\text{times}}{\cdots})\right)$$
$$\leqslant \frac{1}{3}[8(k-1)+k)] = O(k), \tag{36}$$

where we again consider k-local Pauli operators. The depth of the above implementation is $9\prod_{j-1}^{k-1} n_{a_j}$.

C. Controlled-W gates

The final piece we need to calculate the EBGC of the CW operation is the single-qubit controlled version of the reflection operator $\mathbf{I}-2\Pi_0$. This operation can be implemented by simply blocking the evolution of the phase ancilla conditionally on the exit ancilla. This can be done by exciting the exit ancilla to the Rydberg state before the application of the $\mathbf{I}-2\Pi_0$ (as described in Sec. V C) and then deexciting the exit ancilla. Hence, when we use kHE address states, the controlled version of $\mathbf{I}-2\Pi_0$ has an EBGC of $\frac{2}{3}+n_{\mathbf{I}-2\Pi_0}$ where the first term is due to the excitation of the exit ancilla. The depth of the implementations is $2+3=5$.

Finally, we can calculate the EBGC of W and CW, using the above implementation of its constituents. For W operation where the block-encoded signal operator is a linear superposition of k-local Pauli operations, we simply add the EBGCs for each $\bar{U}_{k\mathrm{HE}}$, $V_{k\mathrm{HE}}$, and $\mathbf{I}-2\Pi_0$ over k one-hot encoding ancillary register to obtain a total EBGC of

$$n_W \leqslant 2n_{V_{k\mathrm{HE}}}+n_{(\mathbf{I}-2\Pi_0)}+n_{\bar{U}_{k\mathrm{HE}}}$$
$$=\frac{2}{3}(5k-2)+\frac{2+k}{3}+\left(3k-\frac{8}{3}\right)=\frac{20k-10}{3}, \tag{37}$$

$$d_W = 2d_{V_{k\mathrm{HE}}}+d_{(\mathbf{I}-2\Pi_0)}+d_{\bar{U}_{k\mathrm{HE}}} = 11+19\prod_{j=1}^{k-1} n_{a_j}. \tag{38}$$

On the other hand, the single-qubit controlled W operation can be implemented by (i) applying the controlled transfer operations between $|1\rangle$ and $|r\rangle$ before and after the implementation of $V_{k\mathrm{HE}}^{\dagger}\bar{U}_{k\mathrm{HE}}V_{k\mathrm{HE}}$, (ii) implementing a single-qubit controlled version of $V_{1\mathrm{HE}}$ acting on the kth register, and (iii) implementing a single-qubit controlled version of the reflection operation. Hence, the associated EBGC obeys the following inequality:

$$n_{\mathrm{CW}} \leqslant n_W+2k+2*\frac{2}{3}+\frac{2}{3}=\frac{22k-4}{3}, \tag{39}$$

where on the right-hand side of the inequality, the second term is the EBGC of the single-qubit controlled transfer operations, the third term is the EBGC of two single-qubit controlled $V_{1\mathrm{HE}}$ gates, and the last term is the additional EBGC needed to implement a single-qubit controlled $\mathbf{I}-2\Pi_0$. The depth of the implementation is

$$d_{\mathrm{CW}} = d_W+2*d_{\mathrm{CX}^{(R)}}+2*2 = d_W+10.$$

As a result, as long as the EBGC is valid, the total error probability for the proposed implementation of QSP protocols does not scale with the number N of Pauli operations that make up the block-encoded signal operator. Next, we calculate the EBGC of Hamiltonian simulation using QSP and compare it to the EBGC of Hamiltonian simulation implemented through the product formula.

VII. IMPLEMENTATION OF OPTIMAL HAMILTONIAN SIMULATION PROTOCOLS ON THE RYDBERG ATOM PLATFORM

In the previous section, we demonstrated that the implementation of the algorithmic primitives of the QSP framework in Rydberg atoms is error robust. Next, we focus on Hamiltonian simulation as a particular application of QSP. The concrete Hamiltonian simulation task allows us to benchmark the EBGC of the QSP-based implementations of Hamiltonian simulation against that of two other state-of-the-art implementations.

We first give an overview of different approaches to the Hamiltonian simulation problem, including (i) Hamiltonian simulation algorithms based on product formulas, (ii) QSP-based optimal Hamiltonian simulation of generic Hamiltonians, and (iii) optimal simulation algorithm of Ref. [50] for geometrically local Hamiltonians (which we oversimplistically refer to as block-decimated QSP). In Sec. VII B, we compare these three approaches by comparing the EBGC counts and circuit depths for implementations on the Rydberg atom platform. The details of each Hamiltonian simulation algorithm, as well as the explicit calculations of EBGC and circuit depth, are presented in Appendix F. We note that for geometrically local Hamiltonian simulation, the EBGC of QSP-based Hamiltonian simulation scales with the simulated space-time volume. That is, the EBGC of the error-robust implementations has the same scaling as the optimal gate complexity of geometrically local Hamiltonian simulation. We also comment on the main challenges of implementing Hamiltonian simulation with low total error probability, from the perspective of error-robust implementations.

A. Hamiltonian simulation

The use of physical quantum systems to simulate quantum dynamics has a rich tradition. The task of quantum Hamiltonian simulation is simply stated: given any initial state $|\psi_0\rangle$ of n qubits, a Hamiltonian H, and evolution time t, construct a sequence of quantum gates, which approximates the final

state $|\psi_f\rangle = e^{-iHt}|\psi_0\rangle$. In Ref. [55], Lloyd provided the first demonstration that this task is feasible. The strategy of what is now known as product formulas (PF) [39] is to make use of the algebraic structure of the local terms in the expansion $H = \sum_{l=1}^{L} H_l$ through the Baker-Campbell-Haussdorf identity

$$\exp(-iHt) = (e^{-iH_1 t/r} e^{-iH_2 t/r} \dots e^{-iH_N t/r})^r + O\left(\frac{(L\Lambda t)^2}{r}\right),$$

where $\Lambda = \max_l |H_l|$, and r is the number of time slices used in the approximation. For a fixed error tolerance ϵ, and a geometrically local Hamiltonian for which $O(L) = O(n)$ the number of time slices required is quadratic in the simulated space-time volume $r = O[(nt)^2/\epsilon]$. Since each time slice has $O(n)$ operations, the total gate complexity of the PF algorithm is $O(n^3 t^2/\epsilon)$. Higher-order PF exist [103], and at order $2k$ the dependence of the gate complexity on the system size improves to $O(5^{2k} n^2 t/\epsilon^{1/2k})$), although in the limit of large k, the prefactor becomes prohibitive. Recently, Ref. [104] showed that in the case of a one-dimensional system with nearest-neighbor interactions, the gate complexity can be reduced by a factor of n using an integral representation of the Trotterization error. The resulting algorithm has a gate complexity of $O[(nt)^{1+1/2k}/\epsilon^{1/2k}]$, which scales almost linearly in the simulated space-time volume.

The PF algorithm of Ref. [104] for the one-dimensional (1D) system with nearest-neighbor interactions analytically demonstrates the validity of arguments put forward by Jordan, Lee, and Preskill [63] which claimed that the simulation of quantum dynamics generated by geometrically local Hamiltonians requires a gate complexity at least linear in the simulated space-time volume. The more general question, "Can the same gate complexity be obtained for any time-dependent local Hamiltonian?", was answered affirmatively by Haah, Hastings, Kothari, and Low [50]. The gate complexity of their algorithm is $O[nt\,\mathrm{polylog}(nt/\epsilon)]$, which was proved to be optimal even for simulating only local observables. From the perspective of errors, the optimal gate complexity seems to suggest that the error probability for implementing geometrically local Hamiltonian simulation should scale at least linearly with the simulated space-time volume.

At the first sight, the error probability for implementing a QSP-based Hamiltonian simulation algorithm, as described in Ref. [58], does not achieve the optimal scaling discussed above, although the QSP-based algorithm has optimal query complexity. This is because whether the gate complexity of the algorithm is optimal depends on the gate complexity of the QSP walk operator. Considering the implementation of the walk operator described in our work, the gate complexity of implementing the walk operator scales as $O(N) = O(n^k)$ for a k-local Hamiltonian, hence, resulting in a total gate complexity $[O(N^2 t)]$ that is not optimal. However, the proposed error-robust implementation of QSP protocols for k-local block-encoded signal operators has an EBGC of only $O(k)$ for $\eta_\epsilon = 0$. Consequently, the EBGC of QSP-based Hamiltonian simulation algorithm scales linearly with the query complexity of the QSP protocol, which in turn matches the optimal gate complexity.

TABLE II. The EBGCs and the depth associated with the protocols introduced in Sec. VI, for a k-hot encoding ancillary address register.

	$V_{k\mathrm{HE}}$	$\bar{U}_{k\mathrm{HE}}$	$\mathbf{I} - 2\Pi_0$	CW
EBGC	$(5k-2)/3$	$3k-8/3$	$(2+k)/3$	$(22k-4)/3$
Depth	$3 + 5\prod_{j=1}^{k-1} n_{a_j}$	$9\prod_{j=1}^{k-1} n_{a_j}$	5	$21 + 19\prod_{j=1}^{k-1} n_{a_j}$

B. Results

We calculate the EBGC and circuit depth of three Hamiltonian simulation algorithms: (i) QSP-based simulation algorithm of Ref. [58], (ii) block-decimated QSP of Ref. [50], and (iii) fourth-order product formula, for the one-dimensional disordered transverse field Heisenberg model

$$H_{\mathrm{DH}} = \sum_{i}^{n_{\mathrm{site}}-1} \sigma_i \sigma_{i+1} + \sum_{i}^{n_{\mathrm{site}}} h_i \sigma_i^{(z)}, \tag{40}$$

where $\sigma_i\sigma_j = \sigma_i^{(x)}\sigma_j^{(x)} + \sigma_i^{(y)}\sigma_j^{(y)} + \sigma_i^{(z)}\sigma_j^{(z)}$, and n_{site} is the number of sites in the model, and h_i is a random value drawn uniformly from the interval [0,1]. We choose this model in order to compare the cost of our implementation of QSP-based Hamiltonian simulation to previous empirical studies that used product formulas [49,104].

The EBGC of the QSP-based Hamiltonian simulation for the model at hand is simply given by

$$n_{\mathrm{QSP}} = k^*(n_{CW} + 1/3), \tag{41}$$

$$d_{\mathrm{QSP}} = k^*(d_{CW} + 1), \tag{42}$$

where n_{CW} and d_{CW} are as in Table II, and k^* is the number of iterations needed to implement the QSP-based Hamiltonian simulation, which obeys the following inequality [46]:

$$k^* \leqslant e^q ||H|| t + \frac{\ln(1/\epsilon)}{q} = O(t n_{\mathrm{site}}), \quad \forall\, q \in \mathbb{R}_+ \tag{43}$$

where $||H||$ is bounded by the number of Pauli operators $4n_{\mathrm{site}}$. As result, both the EBGC and the circuit depth of the QSP-based simulation algorithm scale with the simulated space-time volume. Hence, both n_{QSP} and d_{QSP} are linearly proportional to the optimal gate complexity of the Hamiltonian simulation problem [50,63].

To calculate the EBGC for the fourth-order product formula, we use a number of iterations r that were numerically estimated in Ref. [104]. For an error threshold $\epsilon = 10^{-3}$ and $t = n_{\mathrm{site}}$ Ref. [104] finds

$$r \approx 4 n_{\mathrm{site}}^{1.555}. \tag{44}$$

Moreover, in the case of the disordered Heisenberg model in Eq. (40), the circuit depth for each iteration can be reduced to constant through massive parallelization because H_{DH} can be decomposed into only seven sets of nonoverlapping gates. Hence, the circuit depth for the fourth-order product formula scales as $O(r)$. In order to calculate the EBGC for implementing each iteration on the Rydberg platform, we follow the proposal of Ref. [30] and apply the EBGC assignments discussed in Sec. V E (see Appendix F 1 for details). We find that the EBGC of each iteration of the first-order product formula

TABLE III. The scaling of the EBGC and the circuit depth for the three Hamiltonian simulation algorithms considered in this work (assuming $\eta_\epsilon = 0$). The expressions for the fourth-order product formula (PF), we assume $t = n_{\text{site}}$ to be able to use the numerical behavior observed in Ref. [49].

	QSP	Block-decimated QSP [50]	Fourth-order PF [49]
EBGC	$O(n_{\text{site}}t)$	$O(n_{\text{site}}t)$	$O(n_{\text{site}}^{2.555})$
Depth	$O(n_{\text{site}}t)$	$O(t)$	$O(n_{\text{site}}^{1.555})$

is about half the number of two-qubit unitaries required for the implementation (see Appendix F 1 for details). As a result, the EBGC for the fourth-order product formula scales as $O(n_{\text{site}}^{2.555})$ given $t = n_{\text{site}}$.

Finally, we calculate the EBGC for the block-decimated QSP-based Hamiltonian simulation algorithm of Ref. [50], using the EBGC assignments in Sec. V E to the steps of the implementation proposed in Ref. [50]. The EBGC for the optimal algorithm in Ref. [50] has a similar form to that in Eq. (42), and results in the same scaling with respect to the simulated space-time volume (see Appendix F 1 a). On the other hand, thanks to the block decimation, the circuit depth of the optimal Hamiltonian simulation algorithm scales linearly with the simulated time, which is quadratically better than the circuit depth of the QSP-based simulation algorithm. A summary of the scaling of EBGC for all three simulation algorithms is given in Table III. We emphasize that because we always use the same EBGC assignments for all three implementations, our calculations result in a faithful comparison between the different implementations.

In order to compare the overheads for EBGC and the circuit depth, we present the results of the EBGC calculations shown in Fig. 8. Most strikingly, for $n_{\text{site}} = 50$, the QSP-based Hamiltonian simulation of Ref. [58] has an EBGC [green in Fig. 8(a)] that is more than an order of magnitude smaller than that of the simulation algorithm based on the fourth-order product formula (in blue). As discussed in the introduction to this section, the block-decimated algorithm of Ref. [50] (in orange), results in an optimal EBGC scaling for local Hamiltonians, but it has an increased overhead compared to the QSP-based algorithm, resulting from the overhead in the query complexity due to the block decimation (see Appendix F 1 a for details).

From the point of view of the circuit depth, the fourth-order product formula results in the shortest circuit depth Hamiltonian simulation for NISQ devices. However, thanks to the long lifetime of the logical hypefine states, the QSP-based Hamiltonian simulation algorithm can be implemented with low error probability for intermediate-size systems. If we estimate the unit of depth as $t_{\text{step}} = 1$ μs and the lifetime of the hyperfine states as 10 s, the Hamiltonian simulation up to $n_{\text{site}} = 200$ may be implemented without the finite lifetime of the hyperfine states becoming detrimental. The block-decimated algorithm of Ref. [50] has a large overhead because of the block decimation (see Appendix F 1 a).

All system sizes considered in Fig. 8 require a total number of qubits that are accessible for current Rydberg atom array experiments. For instance, for the simulation of a system with $n_{\text{site}} = 200$, the number of address states needed is $N = 4 \times n_{\text{site}} = 800$, which can be encoded by 2HE address states with $n_{a_1} = 27$ and $n_{a_2} = 30$ (see Sec. VI A). The sizes of each ancillary register are small enough such that all atoms can be placed in a blockade radius of $R_b = 9$ μm, in a two-dimensional array, if the distance between the atoms is 3 μm. However, we note that increasing n_{a_1} also results in the depth of the implementation (see Table II). For simplicity, we used 2HE address states with $n_{a_1} = 8$ for all system sizes, which requires $n_{a_2} = n_{\text{site}}/2$ atoms to be enclosed within the Rydberg blockade radius. The controlled Pauli operations required to implement $\bar{U}_{k\text{HE}}$ can be implemented in a parallelized way for all atoms in the second ancillary register, using the coherent transport techniques demonstrated in Ref. [29], when needed.

Our results show two main obstacles facing the implementation of the QSP-based Hamiltonian simulation of the

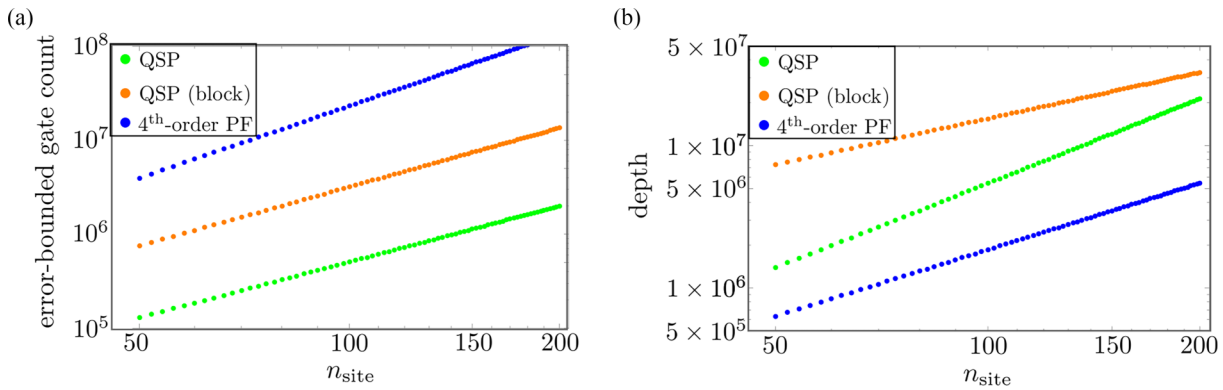

FIG. 8. (a) The EBGCs and (b) the circuit depth of Hamiltonian simulation algorithms (i) based on the fourth-order product formula (blue, Ref. [49]), (ii) QSP-based local Hamiltonian simulation (orange, Ref. [50]) which uses block decimation, and (iii) QSP-based Hamiltonian simulation (green, Ref. [58]). Although from the point of view of depth complexity, the fourth-order product formula is superior in all system sizes considered, the QSP-based Hamiltonian simulation of Ref. [58] exhibits the lowest implementation overhead in terms of EBGCs, achieving more than an order of magnitude reduction compared to the fourth-order product formula. All scalings exhibited in (a) and (b) are in agreement with those tabulated in Table III given $t = n_{\text{site}}$.

disordered Heisenberg model with low total error probability. First is the requirement of an the error-bias parameter η_ϵ that is smaller than numerically calculated in Sec. V C. Even if $\eta_\epsilon = \frac{1}{200}$ is achieved, the resulting input-conditional error probability per QSP iterate will be constant only if $n_{\text{site}} \leqslant 50$ (i.e., $N \leqslant 200$). For all larger systems, the total error probability will scale suboptimally $[n_{\text{QSP}} = O(n_{\text{site}}^2)]$. The second challenge is to further reduce the error probability ϵ_s when the control condition is satisfied (see Sec. V C). In particular, $\epsilon_s \leqslant k^* = O(n_{\text{site}} t)$ is required for the Hamiltonian simulation to be implemented with low error probability, noting that ϵ_s sets the unit of EBGC. Hence, for all results in Fig. 8, an $\epsilon_s = 1\,\%$ will not be sufficient, even if we instead reduce the simulation time by an order of magnitude. That said, we emphasize that even when the input-conditional error probability exceeds 1, error mitigation techniques can be used to further reduce the effect of errors on the expectation values [64].

Although the challenges discussed in the previous paragraph are daunting, it is important to emphasize that the advantage of using error-robust implementations of QSP-based protocol instead of the other methods such as the fourth-order product formula is clear. Generally, the choice of using product formula vs QSP-based Hamiltonian simulation on the Rydberg atom platform depends on the errors relevant to the implementation. If the lifetime of the logical states is the main contributor to the decoherence, then using the product-formula-based Hamiltonian simulation is the most advantageous. On the other hand, if the logical states are long lived and the majority of errors are introduced during gate operations, and it is possible to implement controlled unitaries with biased errors, then QSP-based Hamiltonian simulation has a clear advantage. As we discuss in the next section, the advantage of using error-robust implementations of QSP protocols could be increased by employing them together with other error mitigation and correction techniques.

VIII. CONCLUSIONS AND OUTLOOK

Conclusions. Our work has two main messages. First, it is possible to design implementations of a wide range of quantum protocols where the error probability scales slower than the gate complexity by cotailoring the relevant error model and the circuit that implements the algorithm. Second, the Rydberg atom platform is exceptionally well suited for realizing such error-robust implementations in a hardware-efficient manner.

To design error-robust implementations, we took the structure of two general compilation methods, LCU-based block-encoding unitaries and QSP, as a guide to determining a structured error model, as formalized in the EBGC we introduce in Sec. V E. Aside from being very general and having near-optimal query complexity, the iterative QSP protocols also allowed us to focus solely on an error-robust implementation of a walk operator. On the other hand, the LCU method has two decisive properties that allow for error-robust implementations. The first property is that the occupations of the ancillary address states do not change during the implementation of $\bar{U}$. As a consequence, single-qubit controlled unitary gates which do not accumulate any errors when the control condition is not satisfied can be used to drastically reduce the error probability. Second, LCU allows the address states (see Sec. IV) to be chosen from k-hot encoding bit strings, which drastically reduce the ancillae requirements and allow the use of single-qubit controlled unitaries to distinguish between many control conditions.

Similarly, two observations on the Rydberg atom platform were crucial in achieving an error-robust implementation. The first observation is the availability of error-biased single-qubit controlled Pauli operations using Rydberg atoms. Physically, the protocol for these gates minimizes the laser power that is absorbed by the Rydberg atoms during the implementation, conditionally their input state of the control atom. As a result, the gate-induced errors are only relevant when the control condition is satisfied. The second observation is the availability of a one-hot encoding state preparation using Rydberg atoms. Concatenation of one-hot encoding state-preparation unitaries for k-hot encoding state preparation provides a way to encode many address states for the LCU method without drastically increasing the size of the control register.

We also highlighted the efficacy of the proposed error-robust implementation of QSP-based Hamiltonian simulation in terms of the error-bounded gate complexity, by comparing it to a state-of-the-art implementation of product-formula-based Hamiltonian simulation algorithm. Our results show that the error-robust implementations are advantageous with respect to other state-of-the-art implementations of the Hamiltonian simulation, as the EBGC count is reduced by more than an order of magnitude. On the other hand, the implementation of Hamiltonian simulations for a space-time volume of more than 200 (where the unit of time is given by the time required for a π-phase shift) is difficult for near-term implementation without using additional methods for error mitigation. However, it is likely that this shortcoming will not be overcome before the advent of fault-tolerant quantum processors because the scaling of the EBGC matches the optimal gate complexity for Hamiltonian simulation.

Outlook. Given the generality of QSP and LCU frameworks, and the recent successes of the Rydberg atom platform [15,29], we foresee many promising avenues of research that originate from our work. In this work, we used the EBGC counts of error-robust implementations of the Hamiltonian simulation algorithm as a benchmark. However, using error-robust implementations of QSP protocols for other less demanding quantum information processing tasks, such as state preparation or calculation of Hamiltonian moments for quantum chemistry applications [105], may result in implementations of useful quantum algorithms with low total error probability. Moreover, considering the use of error mitigation techniques [64,106] in the context of error-robust implementations of QSP protocols may also lead to near-term realization of useful quantum algorithms. Overall, we believe that the concept of error-robust implementations will result in fruitful developments in quantum algorithm design.

Our work also provides opportunities to explore important questions for the realization of fault-tolerant quantum computation using Rydberg atoms. In particular, a demonstration of the compatibility of the error-robust implementations presented and the fault-tolerant architecture proposed by

Ref. [32] would greatly ease the resource requirements for realizing FTQC on the Rydberg atom platform. In this respect, it would be interesting to investigate error-correcting codes which allow for transversal CNOT operations, such as the repetition code. While repetition codes cannot correct all possible errors, Ref. [32] has demonstrated the usefulness of repetition codes on the Rydberg atom platform, where many different error channels can be converted to Z errors. Moreover, our results motivate the search for new and more versatile error-biased gate protocols which can further improve error robustness with reduced classical resource requirements. Lastly, the question of whether sparse encodings (e.g., the k-hot encoding address states) are useful in the context of other quantum algorithms, such as variational quantum algorithms, seems to be widely open.

Finally, we emphasize that while our work has focused on the Rydberg atom implementations of QSP protocols, it is possible to use a tool set we introduced to analyze and design error-robust implementations of a broader range of protocols on other platforms. Intuitively, the input-conditional error probability is relevant to virtually all physical platforms simply because the response of the controlled system to external control fields will inevitably depend on the system's state. In this wider context, our work highlights the importance of implementing multiqubit gates in a way that results in minimal interaction between the external control fields and the system if the system is in a state that transforms trivially by the desired gate. From a more practical point of view, the input-conditional error probability enables the analysis of the biases in the gate-induced error probabilities for any given gate implementation, independent of the physical platform in question. Then, by leveraging the biases in implementations of multiqubit gates, we can design circuits that are more robust to gate-induced errors. We expect the study of the input-conditional biases in the gate-induced error processes to be at the heart of the development of useful NISQ devices.

ACKNOWLEDGMENTS

S.Z. and S.S. thank I. Chuang, M. D. Lukin, D. Bluvstein, I. Cong, S. Ebadi, and A. Keesling for insightful comments and helpful discussions. S.Z. acknowledges the financial support from the Swiss National Science Foundation through the Early Postdoc.Mobility grant (Grant No. P2EZP2_184320) and from the Army Research Office, ARO MURI (Grant No. W911NF1910517). S.S. and S.Z. acknowledge NTT Research for their financial and technical support.

APPENDIX A: PROPERTIES OF THE STATE-DEPENDENT ERROR PROBABILITY

1. Relation to trace distance

Consider two pure-state density matrices $\rho_{\rm id} \equiv W|\psi_0\rangle\langle\psi_0|W^\dagger$ and $\rho_{\rm imp} \equiv \tilde{W}|\psi_0\rangle\langle\psi_0|\tilde{W}^\dagger$ resulting from an ideal and imperfect implementation of the desired unitary, respectively. Using the definition of $\tilde{W}$ in Eq. (5), and tracing out the environment, we can write the trace distance $\epsilon_{\rm tr} \equiv \frac{1}{2}{\rm tr}|\bar{\rho}_{\rm id} - \bar{\rho}_{\rm imp}|$ between the associated reduced density matrices $\bar{\rho}_{\rm id} = {\rm tr}_{\rm Env}(\rho_{\rm id})$ and $\bar{\rho}_{\rm imp} = {\rm tr}_{\rm Env}(\rho_{\rm imp})$ as

$$\begin{aligned}\epsilon_{\rm tr} &= \frac{1}{2}{\rm tr}|(1-\alpha^2)|\psi^{\rm sys}\rangle\langle\psi^{\rm sys}| - (1-\alpha^2)\\ &\quad\times\sum_\lambda \lambda^2\big|\bar{\psi}_\lambda^{\rm sys}\big\rangle\big\langle\bar{\psi}_\lambda^{\rm sys}\big|\big|\\ &\leqslant 1-\alpha^2 = \epsilon_{\psi_0},\end{aligned}$$

where, to obtain the inequality, we used the fact that the trace distance is the largest if the space spanned by $|\psi^{\rm sys}\rangle$ is orthogonal to that spanned by $\{|\bar{\psi}^{\rm sys}\rangle\}$, as well as the normalization of the Schmidt coefficients (i.e., $\sum_\lambda \lambda^2 = 1$).

2. Calculating the overall error probability of a quantum circuit

The error probability defined in Eq. (3) can be used to calculate the overall error probability of a quantum protocol given the error probability of each gate acting on an error-free state with no entanglement with the environment. Formally,

$$\epsilon_{C,\phi_0} \leqslant \sum_j^n \epsilon_{j,\phi_{j-1}}, \tag{A1}$$

where $\phi_{j-1} = \prod_{l=1}^{j-1} W_l|\phi_0\rangle$ is a perfect state.

To prove the inequality in the equation above, we simply apply two imperfect unitaries W_1 and W_2 to an initial error-free state $|\phi_0\rangle$. We obtain

$$\begin{aligned}|\phi_0\rangle &\xrightarrow{\tilde{W}_1} \alpha_{1,\phi_0}|\phi_1\rangle + \sqrt{1-\alpha_{1,\phi_0}^2}|E_1\rangle\\ &\xrightarrow{\tilde{W}_2} \alpha_{1,\phi_0}(\alpha_{2,\phi_1}|\phi_2\rangle + \sqrt{1-\alpha_{2,\phi_1}^2}|E_2\rangle)\\ &\quad + \sqrt{1-|\alpha_{1,\phi_0}|^2}|\tilde{E}_1\rangle,\end{aligned} \tag{A2}$$

where $|\tilde{E}_1\rangle = \tilde{W}_2|E_1\rangle$ and $\langle E_2|\tilde{E}_1\rangle = \langle\phi_2|\tilde{E}_1\rangle = 0$ by the assumption that the error processes are incoherent. As a result, the error probability of the circuit $\tilde{C} \equiv \tilde{W}_2\tilde{W}_1$ is

$$\begin{aligned}\epsilon_{C,\phi_0} &= 1 - |\langle\phi_2|\tilde{W}_2\tilde{W}_1|\phi_0\rangle|^2\\ &= 1 - \left(\alpha_{1,\phi_0}\alpha_{2,\phi_1}\right)^2\\ &= 1 - \left(1 - \epsilon_{1,\phi_0} - \epsilon_{2,\phi_1} + \epsilon_{1,\phi_0}\epsilon_{2,\phi_1}\right)\\ &\leqslant \epsilon_{1,\phi_0} + \epsilon_{2,\phi_1}.\end{aligned} \tag{A3}$$

By applying this inequality to each gate in the implementation, we find

$$\epsilon_{C,\phi_0} \leqslant \sum_{j=1}^{n_{\rm gates}}(1 - |\langle\phi_{j-1}|W_j^\dagger\tilde{W}_j|\phi_{j-1}\rangle|^2) \equiv \sum_{j=1}^{n_{\rm gates}}\epsilon_{j,\phi_{j-1}}. \tag{A4}$$

3. Dependence of error probability on the initial state

The most important property of the error probability defined in Eq. (3) is that it takes into account the initial state of the quantum protocol. That is, given the error probabilities ϵ_{W,ψ_j} associated with a basis of states $\{|\psi_j\rangle\}$, we can upper bound the error probability $\epsilon_{W,\psi}$ associated with an initial state $|\psi\rangle = \sum_j a_j|\psi_j\rangle$ as [see Eq. (7)]

$$\epsilon_{W,\psi} \leqslant \sum_j |a_j|^2\epsilon_{W,\psi_j}. \tag{A5}$$

To prove the relation in Eq. (7), consider states $|\phi_a\rangle$ and $|\phi_b\rangle$, with the associated error probabilities defined as

$$\epsilon_{W,\phi_a} \equiv 1 - |\langle\phi_a|W\tilde{W}|\phi_a\rangle|^2 \equiv 1 - \alpha^2_{W,\phi_b},$$
$$\epsilon_{W,\phi_b} \equiv 1 - |\langle\phi_b|W\tilde{W}|\phi_b\rangle|^2 \equiv 1 - \alpha^2_{W,\phi_b}.$$

Now, consider the superposition state $|\psi\rangle = a|\phi_a\rangle + \sqrt{1-|a|^2}|\phi_b\rangle$. The associated error probability is

$$\begin{aligned}\epsilon_{W,\psi} &= 1 - |\langle\psi|W^\dagger\tilde{W}|\psi\rangle|^2 \\ &= 1 - |(\langle\tilde{\phi}_a|a + \langle\tilde{\phi}_b|\sqrt{1-|a|^2})\tilde{W}(\langle\phi_a|a + \langle\phi_b|\sqrt{1-|a|^2})|^2 \\ &= 1 - \left|(\langle\tilde{\phi}_a|a + \langle\tilde{\phi}_b|\sqrt{1-|a|^2})\left(a\alpha_{W,a}|\tilde{\phi}_a\rangle + \sqrt{1-|a|^2}\alpha_{W,b}|\tilde{\phi}_b\rangle + a\sqrt{1-\alpha^2_{W,a}}|E_a\rangle + \sqrt{1-|a|^2}\sqrt{1-\alpha^2_{W,b}}|E_b\rangle\right)\right|^2 \\ &= 1 - ||a|^2\alpha_{W,a} + (1-|a|^2)\alpha_{W,b}|^2, \end{aligned} \tag{A6}$$

where we denote $|\tilde{\phi}_{a/b}\rangle \equiv W|\phi_{a/b}\rangle$, and we grouped together the states describing the coherent and incoherent errors as $|E_{a/b}\rangle$. To obtain the final equality we used the following orthogonality relations:

$$\langle E_{a/b}|\tilde{\phi}_{a/b}\rangle = 0 \quad \text{and} \quad \langle\tilde{\phi}_b|\tilde{\phi}_a\rangle = 0.$$

Using the definitions for in Eq. (A6), we can express $\epsilon_{W,\psi}$ in terms of $\epsilon_{W,a/b}$:

$$\begin{aligned}\epsilon_{W,\psi} =& 2|a|^2(1-|a|^2)\left(1 - \sqrt{(1-\epsilon_{W,\phi_a})(1-\epsilon_{W,\phi_b})}\right) \\ &+ |a|^4\epsilon_{W,\phi_a} + (1-|a|^2)^2\epsilon_{W,\phi_b}. \end{aligned} \tag{A7}$$

In order to show the desired inequality, notice that

$$\begin{aligned}&\left(1 - \sqrt{\left(1-\epsilon_{W,\phi_a}\right)\left(1-\epsilon_{W,\phi_b}\right)}\right) \\ &\quad = \frac{\epsilon_{W,\phi_a} + \epsilon_{W,\phi_b}}{2} + O\left(\max_{k=a,b}\epsilon^2_{W,\phi_k}\right). \end{aligned} \tag{A8}$$

Hence,

$$\begin{aligned}\epsilon_{W,\psi} &\approx |a|^2(1-|a|^2)\left(\epsilon_{W,\phi_a} + \epsilon_{W,\phi_b}\right) \\ &\quad + |a|^4\epsilon_{W,\phi_a} + (1-|a|^2)^2\epsilon_{W,\phi_b} \\ &= |a|^2\epsilon_{W,\phi_a} + (1-|a|^2)\epsilon_{W,\phi_b}. \end{aligned} \tag{A9}$$

By iteratively applying this inequality to a given superposition state $|\psi\rangle = \sum_j a_j|\phi_j\rangle$, we obtain Eq. (7).

4. Calculating the upper bound for $\epsilon_{W,\psi}$ for time-independent and adiabatic control protocols

Here, we show that for time-independent or adiabatic control protocols, the error probability $\epsilon_{W,\psi}$ can be estimated by

$$\epsilon_{j,\phi_0} \leqslant \tau_g \sum_\psi p^{\max}_{\psi,j}\gamma_\psi. \tag{A10}$$

Let us first derive the upper bound for the incoherent errors that result from the interactions between the controlled system and the Markovian environment. To calculate the incoherent error probability, we can use the insights first developed in the field of quantum optics, in particular in the context of the Monte Carlo wave-function simulations [77]. In this setting, the interaction between the system and the environment is described in terms of quantum jumps, which are described by the action of the so-called jump operators $\{C_m\}$ on the reduced density matrix of the controlled system. In the absence of any quantum jumps, the state describing the system evolves under an effective non-Hermitian Hamiltonian

$$H(t) = H_S(t) - \frac{i}{2}\sum_m C_m^\dagger C_m, \tag{A11}$$

where $H_S \equiv \frac{1}{2}(H + H^\dagger)$ is the Hermitian part of the effective Hamiltonian. Using H_S, the desired error-free unitary evolution is given by $W \equiv \mathcal{T}[e^{-i\int_0^{\tau_g} H_S(t)dt}]$, where $\mathcal{T}$ is the time-ordering operator, and τ_g is the time required to implement the desired unitary [78]. Starting from an initial pure state $|\phi_{0,\text{sys}}\rangle$ of the system, the total probability of making no quantum jumps during an evolution time τ is given by $|\mathcal{T}[e^{-i\int_0^\tau H(t)dt}]|\phi_0\rangle|^2$. As a result, the probability that any number of quantum jumps happen is

$$\epsilon_{W,\phi_0} = 1 - \left|\mathcal{T}\left[e^{-i\int_0^\tau H(t)dt}\right]|\phi_0\rangle\right|^2. \tag{A12}$$

That is, in order to calculate the error probability defined in Eq. (3), we need to propagate the initial state $|\phi_0\rangle$ of the system with the evolution generated by the non-Hermitian effective Hamiltonian.

The normalization constant of the initial state evolved by $\mathcal{T}[e^{-i\int_0^\tau H(t)dt}]$ can be easily lower bounded when $H_S(t)$ is time independent or adiabatically varying, the situations that are relevant for the proposed implementation. Our starting point is the Schrödinger equation

$$d t|\phi_0(t)\rangle = -i\left(H_S(t) - \frac{i}{2}\sum_m C_m^\dagger C_m\right)|\phi_0(t)\rangle, \tag{A13}$$

to which the time-ordered integral is the formal solution.

Time-independent case. Consider the case that H_S is time independent during the gate implementation. This is the situation as we are implementing the single-qubit unitaries as well as the three unitaries that make up V_{1HE} in Sec. V D. In order to lower bound the normalization constant, we go to the interaction picture with respect to the system Hamiltonian H_S [75]. The Schrödinger equation that governs the evolution of $|\phi_0^I\rangle \equiv e^{iH_S t}|\phi_0(t)\rangle$ is

$$d t\left|\phi_0^I(t)\right\rangle = -\frac{1}{2}\sum_m e^{iH_S t}C_m^\dagger C_m e^{-iH_S t}\left|\phi_0^I(t)\right\rangle \equiv -iH_{\text{diss}}(t)\left|\phi_0^I\right\rangle. \tag{A14}$$

The solution to the Schrödinger equation in the interaction picture can again be expressed as a time-ordered integral

$$\left|\phi_0^I(t)\right\rangle = \mathcal{T}\left(e^{-i\int_0^t H_{\rm diss}(t)}\right)\left|\phi_0^I(0)\right\rangle. \tag{A15}$$

Because we are considering the situation where the time evolution due to the $H_{\rm diss}(t)$ for time τ only results in a small perturbation to the initial state, we can use the Dyson expansion of the time-ordered integral [75]. Hence, the state at the end of the implemented unitary can be approximated by

$$\left|\phi_0^I(\tau)\right\rangle = \left|\phi_0^I(0)\right\rangle - i\int_0^\tau dt\, H_{\rm diss}(t)\left|\phi_0^I(0)\right\rangle + O[(-iH_{\rm diss})^2]. \tag{A16}$$

Therefore, the square of the desired normalization constant is approximated up to second order in $H_{\rm diss}$ as

$$\begin{aligned}&\left|\left\langle\phi_0^I(0)\middle|\phi_0^I(\tau)\right\rangle\right|^2\\ &\approx \left|1-\frac{1}{2}\int_0^\tau dt\sum_m \left\langle\phi_0^I(0)\middle|e^{iH_St}C_m^\dagger C_m e^{-iH_St}\middle|\phi_0^I(0)\right\rangle\right|^2\\ &\geqslant 1-\int_0^\tau dt\sum_m\left\langle\phi_0^I(t)\middle|C_m^\dagger C_m\middle|\phi_0^I(t)\right\rangle,\end{aligned} \tag{A17}$$

where to obtain the last inequality, we used the fact that the eigenvalues of $H_{\rm diss}^2$ are positive semidefinite, assuming that the controlled system is stable [107]. The term $\int_0^\tau dt\sum_m\langle\phi_0^I(t)|C_m^\dagger C_m|\phi_0^I(t)\rangle$ can be further upper bounded by realizing that the integrand is simply the decay rate of the instantaneous state $|\phi_0^I(t)\rangle$. Hence, expanding this state in the eigenbases $\{|\psi\rangle\}$ of $\sum_m C_m^\dagger C_m$, we obtain

$$\int_0^\tau dt\sum_m\left\langle\phi_0^I(t)\middle|C_m^\dagger C_m\middle|\phi_0^I(t)\right\rangle \leqslant \tau\left(\sum_\psi p_\psi^{\max}\gamma_\psi\right), \tag{A18}$$

where $p_\psi^{\max} = \max_{t\in(0,\tau]}|\langle\psi|\phi_0^I(t)\rangle|^2$ and $\sum_m C_m^\dagger C_m|\psi\rangle = \gamma_\psi|\psi\rangle$. Inserting the inequality in (A18) into Eq. (A17), we find

$$\epsilon_{W,\phi_0} \leqslant \tau\left(\sum_\psi p_\psi^{\max}\gamma_\psi\right), \tag{A19}$$

with $W = e^{-iH_St}$.

Adiabatic case. The proof of the inequality in Eq. (9) is similar to the one for the time-independent Hamiltonian, but instead of considering the interaction picture with respect to the time-evolution operator $e^{-iH_S(t)}$, we consider the Schrödinger equation describing the evolution of the initial state propagated with the unitary describing the adiabatic evolution $U_{\rm ad}(t)$. By the adiabatic theorem, the action of $U_{\rm ad}(t)$ on an initial state $|\phi_0\rangle$, which is an eigenstate of the time-dependent Hamiltonian at $t=0$, is given by

$$U_{\rm ad}(t)|\phi_0\rangle = e^{-i\phi(t)}|\tilde{\phi}_0(t)\rangle, \tag{A20}$$

where $|\tilde{\phi}_0(t)\rangle$ is the instantaneous eigenstate of the time-dependent Hamiltonian $H_S(t)$ and $\phi(t)$ is the accumulated phase which is the sum of the dynamical phase and the Berry phase associated with the adiabatic evolution [108]. The Schrödinger equation which describes the evolution of $|\phi_0^{\rm ad}(t)\rangle \equiv U_{\rm ad}^\dagger(t)|\phi_0(t)\rangle$ is simply

$$dt\left|\phi_0^{\rm ad}(t)\right\rangle = -\sum_m U_{\rm ad}(t)^\dagger C_m^\dagger C_m U_{\rm ad}(t)\left|\phi_0^{\rm ad}(t)\right\rangle. \tag{A21}$$

Evoking the Dyson series as before, the desired overlap is

$$\begin{aligned}\left|\left\langle\phi_0^{\rm ad}(t)\middle|\phi_0^{\rm ad}(t)\right\rangle\right|^2 &\geqslant 1-\int_0^\tau\sum_m\left\langle\phi_0^{\rm ad}(t)\middle|C_m^\dagger C_m\middle|\phi_0^{\rm ad}(t)\right\rangle\\ &\geqslant 1-\tau\sum_\psi p_\psi^{\rm ad,max}\gamma_\psi,\end{aligned} \tag{A22}$$

where $\{|\psi\rangle\}$ are the eigenvectors of $\sum_m C_m^\dagger C_m$ with eigenvalues γ_ψ and

$$p_\psi^{\rm ad,max} \equiv \max_{t\in(0,\tau]}\left|\left\langle\psi\middle|\phi_0^{\rm ad}(t)\right\rangle\right|^2.$$

APPENDIX B: MODEL AND ANALYSIS OF THE EIT-BASED SINGLE-QUBIT CONTROLLED PAULI OPERATION

1. Energy-level diagram

In order to analyze the controlled Pauli operation a model of the target atom is sufficient. The conditional dynamics of the target atom can be studied by turning dipolar interactions on and off.

The Hamiltonian of the target atom during the implementation of the Pauli is ($\hbar = 1$)

$$\begin{aligned}H(t) =& \omega_1|1\rangle\langle 1| + (\omega_R + J)|R\rangle\langle R| + \omega_P|P\rangle\langle P|\\ &+\left[\left(\frac{\Omega_c}{2}e^{-i\omega_c t}|R\rangle\langle P| + \text{H.c.}\right)\right.\\ &\left.\times\left(\frac{\Omega_p}{2}(e^{-i\omega_{P1}t}|P\rangle\langle 1| + e^{-i\omega_{P0}t}|P\rangle\langle 0|) + \text{H.c.}\right)\right],\end{aligned} \tag{B1}$$

where $\omega_j > 0$ with $j = \{1, R, P\}$ is the energy of the atomic state $|j\rangle$, and the energy ω_0 is taken to be zero. The frequencies ω_{P0} and ω_{P1} are the frequencies of the probe laser that couples the logical subspace to $|P\rangle$. Lastly, ω_c is the frequency of the control laser coupling $|P\rangle$ and $|R\rangle$.

Next, we go to the rotating frame generated using the unitary transformation $U_1(t) \equiv e^{-iH_1 t}$:

$$H_1 \equiv \omega_1|1\rangle\langle 1| + \omega_R|R\rangle\langle R| + \omega_P|P\rangle\langle P|. \tag{B2}$$

The effective Hamiltonian in the rotating frame is

$$\begin{aligned}\tilde{H} &= U_1^\dagger H U_1 + i[\partial_t U_1^\dagger]U_1\\ &= J|R\rangle\langle R| + \left\{\left(\frac{\Omega_c}{2}e^{-i(\omega_c-\omega_R+\omega_P)t}|R\rangle\langle P| + \text{H.c.}\right)\right.\\ &\quad+\left[\frac{\Omega_p}{2}(e^{-i(\omega_{P1}-\omega_P+\omega_1)}|P\rangle\langle 1|\right.\\ &\quad\left.\left.+ e^{-i(\omega_{P0}-\omega_P)}|P\rangle\langle 0|) + \text{H.c.}\right]\right\}.\end{aligned}$$

Notice that if we go to another rotating frame generated by $H_2 \equiv \Delta|P\rangle\langle P|$, where we chose Δ, ω_{P1}, and Ω_{P0} such that

$$\Delta = \omega_{P0} - \omega_P = (\omega_{P1} + \omega_1) - \omega_P = \omega_R - \omega_P - \omega_c > 0. \tag{B3}$$

Then, we obtain the Hamiltonian

$$\begin{aligned}\bar{H} &= U_2^\dagger \tilde{H} U_2 + i[\partial_t U_2^\dagger] U_2 \\ &= J|R\rangle\langle R| - \Delta|P\rangle\langle P| + \tfrac{1}{2}[\Omega_c|R\rangle + \sqrt{2}\Omega_p|+_L\rangle]\langle P|,\end{aligned}$$

where $|-_L\rangle \equiv \frac{1}{\sqrt{2}}(|0\rangle + |1\rangle)$. Physically this choice $\Delta, \omega_{P1}, \omega_{P0}$ corresponds to a blue-detuned probe laser drive between the logical qubit states and $|P\rangle$, and a control laser frequency ω_c which ensures two-photon resonance between $|R\rangle$ and the logical subspace when $J = 0$.

2. Electromagnetically induced transparency

Indeed, when $J = 0$, it is convenient to express the Hamiltonian as a simple two level-system

$$\bar{H}^0 \equiv -\Delta|P\rangle\langle P| + \left(\frac{\tilde{\Omega}}{2}|\psi_{\rm br}\rangle\langle P| + \text{H.c.}\right), \tag{B4}$$

where $\tilde{\Omega} \equiv \sqrt{\Omega_c^2 + 2\Omega_p^2} \in \mathbf{R}_{0^+}$, and $|\psi_{\rm br}\rangle \equiv \frac{1}{\tilde{\Omega}}(\Omega_c|R\rangle + \sqrt{2}\Omega_p|+_L\rangle)$ refers to a zero-energy bright state which couples only to $|P\rangle$. This is in contrast to the so-called dark state $|\psi_{\rm d}\rangle \equiv \frac{1}{\tilde{\Omega}}(\Omega_c|+_L\rangle - \sqrt{2}\Omega_p|R\rangle)$, which has trivial dynamics under $\bar{H}^0$. Moreover, $|\psi_{\rm d}\rangle \to |\psi_{+_L}\rangle$ as $\Omega_p \to 0$. As a result, when $J = 0$, any initial state $|\psi_L\rangle \equiv \alpha|0\rangle + \sqrt{1-|\alpha|^2}|1\rangle$ returns back to itself as long as $\Omega_p(t)$ is varied adiabatically. As discussed in Sec. II E, the error probability can be bounded by considering the largest occupation of the Rydberg state, given by x^2. Hence, the error probability due to the decay rate of the Rydberg state is

$$\epsilon_v \leqslant \tau_g \bar{\gamma}_R |x|^2. \tag{B5}$$

In the above contribution to the error probability, the decoherence rate $\bar{\gamma}$ includes all decoherence processes that affect the Rydberg state.

Coherent diabatic errors. One may be worried that because $\tilde{\Omega}$ is a time-dependent control field, the diabatic processes during the gate implementation will result in transitions from $|\psi_{\rm d}\rangle$ to $|\psi_{\rm br}\rangle$. Such processes are strongly suppressed thanks to the AC Stark shift due to the laser amplitude Ω_c. To see this, we diagonalize $\bar{H}^0$. The eigenvalues are

$$E_\pm^0 = \frac{1}{2}(-\Delta \pm \sqrt{\Delta^2 + \tilde{\Omega}^2}), \tag{B6}$$

while the energy of $|\psi_{\rm d}\rangle$ remains zero during the gate duration. In the absence of resonances, diabatic error probability ϵ_d to lowest order can be estimated by [109]

$$\epsilon_d = O\left(\left|\frac{\langle P|\partial_t \bar{H}^0|\psi_d\rangle}{\left(E_{+,\min}^0\right)^2}\right|^2\right), \tag{B7}$$

where $E_{+,\min}^0 \approx \frac{\Omega_c^2}{4\Delta}$ for $\Delta \gg \Omega_c$, and we take $|P\rangle$ as an approximate eigenstate when $\Omega_c \ll \Delta$. Intuitively, $\frac{\Omega_c^2}{4\Delta}$ is exactly the value of the AC Stark shift induced by the strong off-resonant control field Ω_c [39]. On the other hand, the maximum derivative of the effective drive strength $\tilde{\Omega}$ can be approximated by assuming that the pulse shape for the probe laser field is a Gaussian of width σ

$$\Omega_p(t) \equiv \Omega_{p,\max} e^{-\frac{(t-t_0)^2}{2\sigma^2}} \to \partial_t \Omega_p(t) = \Omega_{p,\max} \frac{|t-t_0|}{\sigma^2} e^{-\frac{(t-t_0)^2}{2\sigma^2}}. \tag{B8}$$

The maximum of the derivative occurs at $|t - t_0| = \sigma$. Hence, the diabatic errors scale as

$$\epsilon_d = O\left(\left[\frac{\Omega_{p,\max}^3 \Delta}{\Omega_c^3 \tilde{\Omega}}\right]^2\right), \tag{B9}$$

where we used the fact that $\sigma = O(\Delta/\Omega_{p,\max}^2)$ in our gate implementation. Finally, using the bias factor $x \equiv \sqrt{2}\Omega_{p,\max}/\Omega_c$, we obtain

$$\epsilon_d = O(x^6). \tag{B10}$$

Another consequence of this scaling is that the probability of incoherent errors due to the finite lifetime of the $|P\rangle$ state also scales as $O(x^6)$.

3. Errors due to small frequency shifts

The EIT scheme discussed above relies on the probe and control lasers to satisfy the two-photon resonance condition in Eq. (B3). Hence, it is important to understand the effect of fluctuations that result in a configuration that does not satisfy Eq. (B3). The most important source of such fluctuations is energy shifts of the Rydberg state $|R\rangle$ which are especially susceptible to the stray electric fields as well as the Rydberg state occupation of the surrounding atoms. This should be compared to the relative robustness of the transitions to the intermediate state $|P\rangle$ which has a much shorter lifetime.

Let us then consider a small perturbation $H_{\rm pert} \equiv \delta J|R\rangle\langle R|$. There are two effects to consider. First, using zeroth-order perturbation theory, we find that the energy of the dark state $|\psi_{\rm d}\rangle$ is nonzero:

$$E_{\rm dr} \approx \delta J \langle\psi_{\rm d}|R\rangle\langle R|\psi_{\rm d}\rangle = \delta J \frac{2\Omega_p^2}{\Omega_c^2 + 2\Omega_p^2} \leqslant \delta J \frac{x^2}{1-x^2}. \tag{B11}$$

This energy shift results in an unwanted phase accumulation of $|\psi_{\rm d}\rangle$ compared to the other dark state $|-_L\rangle$. Notice that because the timescale of the gate implementation is $O(\Delta/\Omega_{p,\max}^2) = O[\Delta/(\Omega_c x)^2]$, for small bias parameters x, the undesired phase is $\phi_{\rm dr} = O(\frac{\delta J \Delta}{\Omega_c^2})$. Starting from the $|1\rangle = \frac{1}{\sqrt{2}}(|+\rangle - |-\rangle)$ state, this small phase accumulation would cause an error of $1 - \frac{1}{4}|1 + e^{i\phi_{\rm dr}}|^2 \sim (\delta J/E_+^0)^2$. As a result, the EIT scheme can be made more robust against fluctuations in the energy of the Rydberg state by increasing the AC Stark shift $E_{+,\min}$.

Second, when δJ is nonzero, the dark state $|\psi_{\rm d}\rangle$ acquires a contribution from the intermediate state $|P\rangle$ and hence becomes bright. In particular, given the short lifetime of the $|P\rangle$, we may worry that the evolution for a small δJ may be error prone. Again, we can calculate the contribution from the $|P\rangle$ state up to the lowest order in δJ using perturbation theory.

The eigenvectors of $\bar{H}^0$ are $(|-_L\rangle, |\psi_{\rm d}\rangle, |+_{RP}\rangle, |-_{RP}\rangle)$, where we define

$$|+_{RP}\rangle \equiv \cos(\theta/2)|\psi_{\rm br}\rangle + \sin(\theta/2)|P\rangle, \tag{B12}$$

$$|-_{RP}\rangle \equiv -\sin(\theta/2)|\psi_{\rm br}\rangle + \cos(\theta/2)|P\rangle, \tag{B13}$$

whose eigenvalues are given by $E^0_\pm$ in Eq. (B6), respectively. The coefficients in Eq. (B13) are parametrized using the mixing angle defined as $\theta = \arctan(-\tilde{\Omega}/\Delta)$. The nonzero matrix elements of $J|R\rangle\langle R|$ in this basis are

$$\delta J\langle +_{RP}|R\rangle\langle R|\psi_{\rm d}\rangle = -\delta J\frac{\sqrt{2}\Omega_p}{\sqrt{\Omega_c^2+2\Omega_p}}\cos(\theta/2) \equiv \delta\tilde{J}_+, \tag{B14}$$

$$\delta J\langle -_{RP}|R\rangle\langle R|\psi_{\rm d}\rangle = \delta J\frac{\sqrt{2}\Omega_p^2}{\sqrt{\Omega_c^2+2\Omega_p^2}}\sin(\theta/2) \equiv \delta\tilde{J}_-. \tag{B15}$$

Therefore, the eigenstate of the system with $\delta J \neq 0$ up to the first order of perturbation theory is

$$\left|\tilde{\psi}_{\rm d}\right\rangle = |\psi_{\rm d}\rangle - \left(\frac{\delta\tilde{J}_-}{E^0_-}|-_{RP}\rangle + \frac{\delta\tilde{J}_+}{E^0_+}|+_{RP}\rangle\right) + O(\delta J^2), \tag{B16}$$

which is a good approximation when $\delta J/E^0_{+,\min} \ll 1$. As a result, contribution to $|\tilde{\psi}_{\rm d}\rangle$ from the $|P\rangle$ state is given to lowest order by

$$\begin{aligned}\langle P|\tilde{\psi}_{\rm d}\rangle &= -\left(\frac{\delta\tilde{J}_-}{E^0_-}\langle P|-_{RP}\rangle + \frac{\delta\tilde{J}_+}{E^0_+}\langle P|+_{RP}\rangle\right) + O(\delta J^2)\\ &= -\left(\frac{\delta\tilde{J}_-\cos(\theta/2)}{E^0_-} + \frac{\delta\tilde{J}_+\sin(\theta/2)}{E^0_+}\right) + O(\delta J^2)\\ &= -\delta J\frac{\sqrt{2}\Omega_p}{\sqrt{\Omega_c^2+2\Omega_p^2}}\frac{\sin(\theta)}{2}\left(\frac{1}{E^0_-}+\frac{1}{E^0_+}\right) + O(\delta J^2)\\ &= \delta J\frac{\sqrt{2}\Omega_p}{\sqrt{\Omega_c^2+2\Omega_p^2}}\frac{\sin(\theta)}{2}\left(\frac{4\Delta}{\Omega_c^2}\right) + O(\delta J^2)\\ &\approx \frac{2\delta J}{\Omega_c}x.\end{aligned} \tag{B17}$$

Hence, the error probability due to the dissipative dynamics of the $|P\rangle$ state also scales as $(\frac{\delta J}{\Omega_c})^2x^2$.

4. Dynamics when the control condition is satisfied

We analyze the dynamics of the target atom when the control condition is satisfied and the Rydberg state of the target atom is shifted by $J \ll \frac{\Omega_c^2}{4\Delta}$. To this end, we first diagonalize the Hamiltonian $\bar{H}$ with respect to $J|R\rangle\langle R|$, and then use perturbation theory in Ω_p to determine the effective dynamics.

We can diagonalize $\bar{H}$ with respect to terms proportional to J and Ω_c since both terms only act on the two-dimensional subspace spanned by $|R\rangle$ and $|P\rangle$. We obtain

$$\begin{aligned}\bar{H} =& E^J_+\left|+^J_{RP}\right\rangle\left\langle+^J_{RP}\right| + E^J_-\left|-^J_{RP}\right\rangle\left\langle+^J_{RP}\right|\\ &+\left[\frac{\Omega_p}{\sqrt{2}}|+_L\rangle\left(\left\langle+^J_{RP}\right|\sin(\theta^J/2) + \left\langle-^J_{RP}\right|\cos(\theta^J/2)\right)\right.\\ &\left.+\text{H.c.}\right],\end{aligned} \tag{B18}$$

where

$$\begin{aligned}E^J_\pm &\equiv \frac{1}{2}\left[(-\Delta+J) \pm \sqrt{(\Delta+J)^2+\Omega_c^2}\right],\\ \left|+^J_{RP}\right\rangle &\equiv \cos(\theta^J/2)|R\rangle + \sin(\theta^J/2)|P\rangle,\\ \left|-^J_{RP}\right\rangle &\equiv -\sin(\theta^J/2)|R\rangle + \cos(\theta^J/2)|P\rangle,\\ \theta^J &\equiv \arctan\left(\frac{\Omega_c}{-\Delta+J}\right)\end{aligned} \tag{B19}$$

and we expressed $|P\rangle = |+^J_{RP}\rangle\sin(\theta^J/2) + |-^J_{RP}\rangle\cos(\theta^J/2)$. The first-order perturbation theory on $|+_L\rangle$ results in the following approximation to the eigenstate of $\bar{H}$:

$$\begin{aligned}|\tilde{+}_L\rangle =& |+_L\rangle - \frac{\sqrt{2}\Omega_p\sin(\theta^J/2)}{2E_+}|+_{RP}\rangle\\ &-\frac{\sqrt{2}\Omega_p\cos(\theta^J/2)}{2E_-}|-_{RP}\rangle + O\left(\Omega_p^2\right).\end{aligned} \tag{B20}$$

In the limit that $\Delta \gg \Omega_c, J$, the following approximations are useful:

$$E^J_+ \approx J \quad E^J_- \approx -\Delta, \tag{B21}$$

$$\cos(\theta^J) \approx 1 - \frac{\Omega_c^2}{2\Delta^2}; \quad \sin(\theta^J) \approx -\frac{\Omega_c}{\Delta}. \tag{B22}$$

The perturbed state is not a dark state because it has a contribution from $|P\rangle$:

$$\begin{aligned}\langle P|\tilde{+}_L\rangle &= -\frac{\sqrt{2}\Omega_p}{2}\left(\frac{\sin(\theta^J/2)^2}{E^J_+} + \frac{\cos(\theta^J/2)^2}{E^J_-}\right)\\ &= -\frac{\sqrt{2}\Omega_p}{4}\left[\left(\frac{1}{E^J_+}+\frac{1}{E^J_-}\right) + \left(\frac{1}{E^J_-}-\frac{1}{E^J_+}\right)\cos(\theta^J)\right]\\ &\approx \frac{\sqrt{2}\Omega_p}{2\Delta}\left(1-\frac{\Omega_c^2}{4\Delta J}\right).\end{aligned} \tag{B23}$$

On the other hand, the occupation probability of the target Rydberg state gives us the probability of double occupation

$$\begin{aligned}\langle R|\tilde{+}_L\rangle &= \frac{\sqrt{2}\Omega_p}{2}\left(\frac{\sin(\theta^J/2)\cos(\theta^J/2)}{E^J_+}\right.\\ &\quad\left.-\frac{\cos(\theta^J/2)\sin(\theta^J/2)}{E^J_-}\right)\\ &= \frac{\sqrt{2}\Omega_p}{4}\sin(\theta^J)\left(\frac{1}{E^J_+}-\frac{1}{E^J_-}\right)\\ &\approx -\frac{\sqrt{2}\Omega_p\Omega_c}{4J\Delta},\end{aligned} \tag{B24}$$

where in the final approximation, we used $J \ll \Delta$.

The eigenenergy of $|\tilde{+}_L\rangle$ is approximated up to first order in perturbation theory by

$$\tilde{E}^J_{+_L} = \frac{\Omega_p^2}{2}\left(\frac{\sin(\theta^J/2)^2}{E^J_+} + \frac{\cos(\theta^J/2)^2}{E^J_-}\right) \approx \frac{\Omega_p^2}{2\Delta}\left(1 - \frac{\Omega_c^2}{4\Delta J}\right), \tag{B25}$$

where the approximation in the second line is obtained by assuming $\frac{\Omega_c}{4\Delta}^2 \ll 1$. Then, a π pulse between the $|+_L\rangle$ and $|-_L\rangle$ can be implemented provided that the drive pulse satisfies

$$\int_0^{\tau_g} dt\, \frac{\Omega_p(t)^2}{2\Delta} = \pi. \tag{B26}$$

Notice that, intuitively, the approximation above in Eq. (B25) means that when the AC Stark shift is comparable to the dipolar interaction strength J, then the length of the probe pulse to implement the conditional Pauli gate depends on the strength of the dipolar interaction.

APPENDIX C: QUANTUM SIGNAL PROCESSING

We begin our discussion with the quantum control theory of a single qubit. The pioneering work of Ref. [45] asked the following question. Given two unitary operations on a single qubit $G(\phi) = e^{i\phi\sigma_z}$, and $R(\theta) = -ie^{i\pi/4\sigma_z}e^{i\theta\sigma_x}e^{-i\pi/4\sigma_z}$, with Pauli operators $\sigma_{i=x,y,z}$, what single-qubit transformations can we design by the following sequence of gates

$$G(\phi_k)R(\theta)G(\phi_{k-1})R(\theta)\ldots G(\phi_1)R(\theta)G(\phi_0) \tag{C1}$$

alternating between $G(\phi)$ and $R(\theta)$ while keeping θ constant and varying ϕ_i between each iteration.

The concept of signal processing is established by considering $\cos(\theta) = x$ as the signal encoded in the signal unitary

$$R(\theta) = \begin{pmatrix} x & \sqrt{1-x^2} \\ \sqrt{1-x^2} & -x \end{pmatrix}, \tag{C2}$$

which is to be processed by the control angles $\{\phi_i\}$. We emphasize that the single-qubit rotation $R(\theta)$ can be interpreted as a block encoding of the signal x since $\langle 0|R(\theta)|0\rangle = x$. Reference [58] showed that the first diagonal matrix element of the unitary resulting from a k-fold iteration of $G(\phi_i)R(\theta)$ can be designed to be *any* degree-k complex-valued fixed-parity polynomial $P(x)$ via a judicious choice of the angles ϕ_i. Formally,

$$\mathcal{U}_s \equiv \left[\prod_{i=1}^{k} G(\phi_i)R(\theta)\right]G(\phi_0) = \begin{pmatrix} P(x) & iQ(x)\sqrt{1-x^2} \\ iQ^*(x)\sqrt{1-x^2} & P(x)^* \end{pmatrix}, \tag{C3}$$

where $Q(x) \in \mathbf{C}$ is a degree-$(k-1)$ polynomial whose parity is opposite to that of $P(x)$. Unitarity introduces the constraint $|P(x)|^2 + (1-x^2)|Q(x)|^2 = 1$ for $x \in [0, 1]$.

While the above scheme seems to block encode only fixed-parity polynomial $P(x)$, it is straightforward to block encode an arbitrary-parity polynomial if we notice

$$\begin{pmatrix} P(x) & iQ(x)\sqrt{1-x^2} \\ iQ^*(x)\sqrt{1-x^2} & P(x)^* \end{pmatrix} = A(x)\mathbf{1} + iB(x)\sigma_z + iC(x)\sigma_x + iD(x)\sigma_y, \tag{C4}$$

where all coefficients are polynomials of fixed parity, with $A(x)$ and $B(x)$ having degree k, while $C(x)$ and $D(x)$ having degree $k-1$ (see Ref. [110] for a full characterization). Hence, we can obtain block encodings of arbitrary parity polynomials by a simple rotation of the qubit. To summarize, interweaving single-qubit rotations $G(\phi_i)$ and $R(\theta)$ allows one to construct a block-encoding of an arbitrary-parity polynomial of a block-encoded signal x given a suitable set of phases $\{\phi_i\}$. We note that determining the desired set of phases $\{\phi_i\}$ is not a trivial task. For instance, see Ref. [47] for concrete procedures for various examples and its Appendix for numerically optimized phase angles.

Reference [45] further showed that the signal processing of scalar x can be extended to processing of multidimensional operators using only a single additional ancilla qubit, which we will call the "exit" ancilla in the following. Intuitively, by applying a conditional block encoding of the block-encoded operator H, we can elevate the eigenvalues λ_i of A (e.g., $A|\lambda\rangle = \lambda|\lambda\rangle$) to rotation angles θ_i for the exit ancilla.

Formally, given that the block-encoding unitary is Hermitian $U^2 = \mathbf{1}$, we can introduce an iterate $W \equiv [2(|0\rangle\langle 0|)^{\otimes n_a} - \mathbf{1}]U$, which can be written as a direct sum over SU(2)-invariant subspaces associated with each eigenvalue of H:

$$W = \bigoplus_\lambda \begin{pmatrix} \lambda & -\sqrt{1-\lambda^2} \\ \sqrt{1-\lambda^2} & \lambda \end{pmatrix}_\lambda, \tag{C5}$$

where the subscript λ means that the matrix representation is written in the basis

$$|G_\lambda\rangle = |0\rangle^{\otimes n_a}|\lambda\rangle, \quad \left|G_\lambda^\perp\right\rangle = \frac{\lambda|G_\lambda\rangle - U|G_\lambda\rangle}{\sqrt{1-\lambda^2}}. \tag{C6}$$

Hence, the eigenvectors of W are given by

$$\left|G_{\lambda_\pm}\right\rangle = \frac{1}{\sqrt{2}}(|G_\lambda\rangle \pm |G_\lambda^\perp\rangle), \tag{C7}$$

with associated eigenvalues $e^{\pm i\theta_\lambda}$, where $\theta_\lambda \equiv \arccos(\lambda)$.

Reference [45] showed that using a controlled version of W with the exit ancilla as the control, it is possible to implement the unitary,

$$U_\phi = \sum_{\lambda,\eta=\pm} R_\phi(\theta_\lambda) \otimes |G_{\lambda\eta}\rangle\langle G_{\lambda\eta}|, \tag{C8}$$

which rotates the exit ancilla along a fixed axis on the x-y plane as determined by ϕ and by an angle determined by the phase of the eigenvalue $e^{i\theta_\lambda}$. The decomposition of U_ϕ in terms of a controlled version of W and single-qubit rotations of the exit ancilla is the following:

$$\begin{aligned} U_\phi &= \left(e^{-i\phi\sigma_z^{(\mathrm{ex})}/2} \otimes \mathbf{1}\right)U_0\left(e^{-i\phi\sigma_z^{(\mathrm{ex})}/2} \otimes \mathbf{1}\right), \\ U_0 &\equiv |+\rangle_{\mathrm{ex}}\langle +| \otimes \mathbf{1} + |-\rangle_{\mathrm{ex}}\langle -| \otimes W \\ &= \sum_{\lambda,\eta=\pm} e^{i\eta\theta_\lambda/2} R_{\mathrm{ex}}(\eta\theta_\lambda) \otimes |G_{\lambda\eta}\rangle\langle G_{\lambda\eta}|, \end{aligned} \tag{C9}$$

and $\sigma_z^{(\mathrm{ex})}$ is a Pauli operator acting on the exit ancilla.

Noting that the eigenvectors of W satisfy

$$\langle 0^{\otimes n_a}| \otimes \mathbf{1}_{\mathrm{sys}})|G_{\lambda\pm}\rangle = \sqrt{\frac{1}{2}}|\lambda\rangle, \tag{C10}$$

an arbitrary-parity polynomial of a Hermitian block-encoded operator can be block encoded. That is,

$$\langle +|_{\mathrm{ex}}\langle 0|^{\otimes n_a} \prod_{j=1}^{k/2} U_{\phi_{2j}} U^{\dagger}_{\phi_{2j+1}+\pi}|0\rangle^{\otimes n_a}|+\rangle_{\mathrm{ex}} \tag{C11}$$

$$= \sum_{\lambda} \tilde{P}(\lambda)|\lambda\rangle\langle\lambda|, \tag{C12}$$

where $\tilde{P}(x)$ is an arbitrary parity polynomial of degree k. As a result, QSP provides an indispensable tool for processing block-encoded signal operators. Most importantly, for the following discussion on Hamiltonian simulation we would like to implement $\tilde{P}(\lambda) \approx e^{i\lambda t}$.

APPENDIX D: QSP-BASED OPTIMAL HAMILTONIAN SIMULATION

The Hamiltonian simulation algorithm based on the QSP framework uses the block encoding of the Hamiltonian H to construct a polynomial approximation of $P(H) \approx e^{-iHt}$. Reference [58] proved that this method results in an optimal query complexity, which is

$$k^* = O\left(\alpha t + \frac{\log(1/\epsilon)}{\log\log(1/\epsilon)}\right), \tag{D1}$$

where we define $\alpha \equiv ||H|| = O(N)$ for a Hamiltonian composed of N Pauli strings. The linear scaling of k^* with respect to the spectral norm of the Hamiltonian is due to the unitarity block encoding utilized by QSP. We also emphasize that the scaling of the query complexity with respect to error tolerance ϵ is exponentially improved compared to the Trotterization-based simulation algorithms [49]. Moreover, it is possible to show that the number of queries k can be bound by the following inequality [46]:

$$k^* \leqslant e^q \alpha t + \frac{\ln(1/\epsilon)}{q} \quad \forall\, q \in \mathbf{R}. \tag{D2}$$

The query complexity of the QSP-based Hamiltonian simulation can be related to the time and error-bounded gate complexities, given a specific implementation of the query. We emphasize that even if the time required to implement the query is constant, the time complexity of Hamiltonian simulation of a system of size n_{site} for a time $t = n_{\mathrm{site}}$ results in an implementation time of $O(n_{\mathrm{site}}^2)$, which is suboptimal. On the other hand, implementing the query (i.e., the walk operator) with constant EBGC implies an implementation optimal with respect to errors. In Appendix F, we demonstrate that this optimal error complexity is achieved for our proposal for k-local Hamiltonians.

APPENDIX E: OPTIMAL QUANTUM HAMILTONIAN SIMULATION OF LOCAL HAMILTONIANS

Since Ref. [63] argued that the optimal gate complexity of an algorithm simulating local Hamiltonian simulations should scale roughly as the simulated space-time volume, there has been a renewed interest in finding rigorous tight bounds for optimal simulation of local Hamiltonians [50,104]. In 2018, Haah *et al.* [50] constructed an algorithm with linear gate complexity in the simulated $(d+1)$-dimensional space-time volume $O[nt\,\mathrm{polylog}(n^{1/d}t/\epsilon)]$, where ϵ is the total error tolerance of the Hamiltonian simulation, and proved the optimality of this bound. In this Appendix, we give a brief review of this work to motivate the constructions in Appendix F.

From a bird's eye view, the algorithm in Ref. [50] uses a block decimation of the unitary time evolution e^{-iHt} that guarantees that the error due to the decomposition is bound by the Lieb-Robinson (LR) theorems [111,112]. LR theorems formalize the intuition that for local Hamiltonians, the maximum speed that information can travel is a well-defined constant, called the Lieb-Robinson velocity v. The overall structure of the algorithm in Ref. [50] is depicted in Fig. 9 for the case of a one-dimensional system, which we consider for the sake of simplicity. Any block decimation of the evolution operator introduces local errors at each boundary. These errors can be described as the omission of Hamiltonian terms H_{bd} at the boundaries of neighboring blocks. Upon time evolution by a local Hamiltonian, it is possible to ensure that these errors propagate only within the associated light cones (depicted as yellow and blue triangles in Fig. 9) up to exponentially small corrections. The knowledge of the local spread of such errors allows one to design a spin-echo-like algorithm that reverses the spread of the errors, leaving behind only the exponentially small corrections. Formally, one can show that for a given block decimation of the sites $X = A \bigcup B \bigcup C$, a constant $\mu = O(1)$, Lieb-Robinson velocity v, and $vt \ll l = \mathrm{dist}(B)$

$$|U_t - e^{-iH_{A\cup B}t} e^{iH_B t} e^{-iH_{B\cup C}t}| < O[|H_{bd}|\exp(-\mu l)], \tag{E1}$$

where H_X denotes the sum of Hamiltonian terms that have a support on a region X. Longer times can be simulated by applying the same decimated evolution operator repeatedly t times to obtain an error linearly increasing with t.

Given the above discussion, the choice of the smallest dimensions of each block denoted l on the space axis and $t_\square$ in the time axis, is determined by (i) the tolerance ϵ_{LR} for errors resulting from block determination, (ii) the tolerance $\epsilon_\square$ for errors due to the approximate Hamiltonian simulation based on QSP of each block, and (iii) the number of blocks $m = O(nt/lt_\square)$. In particular, given a total error tolerance ϵ, we would like the error associated with each block to be $\epsilon_\square + \epsilon_{\mathrm{LR}} = O(\epsilon/m)$ [39,74]. In the following, we assume $\epsilon_\square = \epsilon_{\mathrm{LR}}$. Given Eq. (E1), we have $\epsilon_{\mathrm{LR}} = O(e^{-\mu l})$, and the spatial dimension of each block is $l = O[\log(nt/t_\square\epsilon))]$. We are then left with the challenge of realizing the Hamiltonian simulation of a system of size $O[\log(nt/t_\square\epsilon)]$, with error tolerance $\epsilon_\square = O(\epsilon\frac{lt_\square}{nT})$ using only $O[\mathrm{polylog}(nt/t_\square\epsilon)]$ gates. Fortunately, the QSP-based Hamiltonian simulation algorithm discussed in Appendix D has a query complexity that scales logarithmically with $\epsilon_\square^{-1}$, resulting in a gate complexity that scales almost linearly with

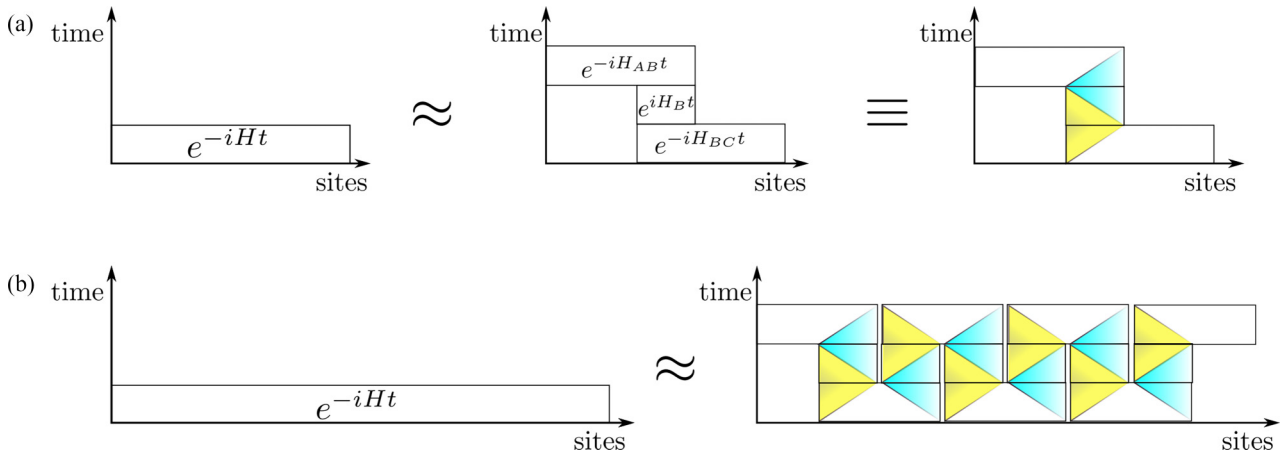

FIG. 9. Overview of the algorithm in Ref. [50]. (a) The first approximation depicts the principal relation between the initial and decimated circuits for Hamiltonian simulation. On the other hand, the equivalence relation depicts the spread and reversal of errors originating from the left (yellow) and right (blue) edges of each block. In the first time step, the error due to the left edge of a block simulating $e^{-iH_{BC}t}$ spreads within the light cone depicted in yellow. In the second step, the evolution operator e^{iH_Bt} fixes this error but it also introduces new errors due to the right boundary of the block. The final evolution by $e^{-iH_{AB}t}$ reverses the error introduced by e^{iH_Bt}, and the approximation error is bounded by the exponentially small error outside of the light cone given the intermediate block is large enough to contain the light cone. (b) Demonstration of how the block-decimation operator can be repeated in space and the pattern of errors induced.

the simulated space-time volume

$$O[nt\ \mathrm{polylog}(nt/t_{\square}\epsilon)]. \tag{E2}$$

In summary, the optimal quantum Hamiltonian simulation algorithm by Haah *et al.* uses the QSP-based query optimal Hamiltonian simulation algorithm in combination with a clever block decimation of the space-time evolution to obtain a near-optimal gate count for the Hamiltonian simulation algorithm for local Hamiltonians.

We emphasize that the aforementioned optimal gate count is different from EBGC in Sec. V E, as it does not take into account the specific error model of the implementation. Moreover, the near-optimal gate count of the algorithm in Ref. [50] comes at a price of a high implementation overhead [49], which makes it less efficient than the product-formula algorithms for Hamiltonian simulation on near-term intermediate-scale quantum (NISQ) processors. In the next Appendix, we calculate the overhead associated with the Rydberg platform implementations of both the product formula and the QSP-based Hamiltonian simulation protocols. While the overhead of the algorithm in Ref. [50] makes it undesirable for NISQ devices, we find that the EBGC of QSP-based Hamiltonian simulation of Ref. [58] has orders of magnitude of smaller overhead for gate errors compared to its competitors.

APPENDIX F: CONCRETE CIRCUITS AND GATE COUNTS

Here, we use the results of Sec. VI to analyze the resource requirements for the implementation of QSP-based and Hamiltonian simulation algorithms on the Rydberg atom platform and compare them to those needed to implement Hamiltonian simulation based on product formula. To this end, we briefly discuss the implementation of product-formula-based Hamiltonian simulation algorithms on the Rydberg platform and calculate the associated EBGCs.

1. Hamiltonian simulation

Here, we explicitly calculate the resources needed for implementing algorithms in the framework of QSP, using LCU-based block encoding. In particular, for a system of n_{site} qubits, we consider the number of error-bounded gates, the run time, and the number of ancillae required to implement (i) QSP-based Hamiltonian simulation, (ii) optimal simulation of local Hamiltonians in Ref. [50], and finally (iii) Hamiltonian simulation using fourth-order product formula. We note that in all of the calculations in this section, we assume that the blockade radius is as large as the required system size.

a. Implementing Haah's optimal Hamiltonian simulation (Ref. [50])

To facilitate the calculation of resources needed for Hamiltonian simulation, it is necessary to choose an explicit Hamiltonian to be simulated. Here, we chose a one-dimensional disordered Heisenberg Hamiltonian H_{DH} as our target system

$$H_{\mathrm{DH}} = \sum_{i}^{n_{\mathrm{site}}-1} \sigma_i\sigma_{i+1} + \sum_{i}^{n_{\mathrm{site}}} h_i\sigma_i^{(z)}. \tag{F1}$$

The choice of the disordered Heisenberg Hamiltonian as our target allows us to directly compare the cost of our implementation of QSP-based Hamiltonian simulation to that implied by the previous empirical studies that use product formulas [49,104].

Our first task is to find the dimensions of each block in the decimation given the parameters n_{site}, t, and the error tolerance ϵ.

In one dimension, the number of blocks is

$$m = 4\left(\frac{2tn_{\mathrm{site}}}{t_{\square}l}\right), \tag{F2}$$

where l and $t_{\square}$ are the shortest dimensions of each block along space and time coordinates (see Fig. 10), respectively. Hence,

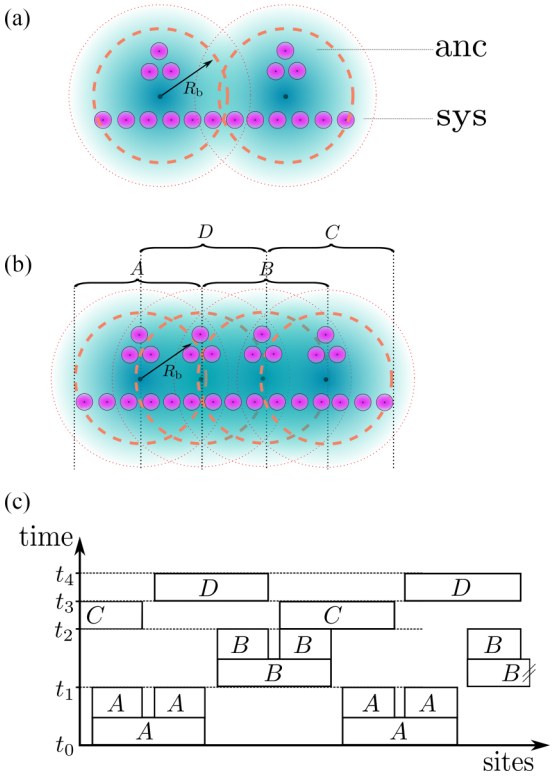

FIG. 10. The overall schematic for the parallelized implementation of the optimal Hamiltonian simulation of [50] on the Rydberg platform. (a) A depiction of the sources of cross-talk errors due to the algebraic decay of the interaction potential, which makes the definition of Rydberg blockade radius R_b fuzzy. The two system atoms at the boundary between the two blockade volumes introduce errors due to unwanted blockade interactions. (b) The experimental configuration for the parallelized application of the algorithm in Ref. [50]. We use twice as many overlapping simulation regions (i.e., A, B, C, and D) as depicted in Fig. 9 to reduce the errors due to the algebraic decay of the dipolar interactions. (c) The schedule for applying the QSP-based Hamiltonian simulation algorithm on four different simulation regions to reduce the cross-talk errors. The cross-talk errors can be reduced arbitrarily at the expense of an increase in the circuit depth.

we have $m/2$ blocks of length l and $m/2$ blocks of length $2l$, and the overall factor of 4 in Eq. (F2) is due to the normalization of the Hamiltonian for each site (i.e., $H_{i,i+1} \leqslant 1$). For a given spatial extent l of each block, the parameter $t_\square$ can be determined by studying the scaling of the errors due to the decimation as a function of time for a single block. This was done in Ref. [50] for the disordered Heisenberg model and the following relation was found:

$$0.175\left(\frac{7.9t_\square}{l+0.95}\right)^{l+0.95} = \frac{\epsilon}{3m} \equiv \epsilon_{\rm LR}. \tag{F3}$$

For the data presented here, we set $t = 4n_{\rm site}$ and $m\epsilon_\square = m\epsilon_{LR} = 10^{-3}/2$. For the calculations presented here we choose $l = 9$.

Once the parameters l and $t_\square$ are determined, we can also calculate the order $k_\square$ of the polynomial approximation to the Hamiltonian evolution associated with each block using Eq. (43). For the smaller blocks of spatial size l, we get

$$k_\square(l) = \min_q \left[e^q t_\square l + \frac{\ln(1/\epsilon_\square)}{q}\right], \tag{F4}$$

while for blocks of spatial size $2l$, we replace $l \to 2l$.

The simultaneous implementation of Hamiltonian simulation in each block may introduce unwanted cross-talk errors due to the algebraic decay of the dipolar interactions, even if the blockade radii of adjacent blocks do not overlap [see Fig. 10(a)]. We circumvent this problem by doubling the implementation time required to simulate evolution for a time $t_\square$. The scheme is depicted in Fig. 10 for a one-dimensional system. For each time step, we require that the blockade radii associated with different spatial blocks have negligible overlap. We also note that, in principle, the block encoding and the QSP-based Hamiltonian simulation algorithms have the flexibility to implement the simulation of Hamiltonians with different boundary terms are omitted at each step (see Fig. 9), as well as changing the overall sign of the Hamiltonian $H \to -H$.

The EBGC for an error-robust implementation of the local Hamiltonian simulation algorithm of Ref. [50] is

$$\begin{aligned} d_{\rm BQSP} &= 2\frac{t}{t_\square}[k_\square(l) + 2k_\square(2l)](d_{\rm CW}+1), \\ n_{\rm BQSP} &= \frac{m}{2}k_\square(2l)[n_{\rm CW}+1/3]. \end{aligned} \tag{F5}$$

Notice that the overall factor of 2 in the depth of implementation comes from our method of reducing the cross talk between the blocks (see Fig. 10). The number of ancillae is increased by an additional $O(\frac{n_{\rm site}}{l})$ ancillae compared to the requirements for QSP-based Hamiltonian simulation in order to facilitate the parallelization by the block decimation.

b. Comparison to Hamiltonian simulation with product formulas

Here, we compare the resource requirements for our implementation of the QSP-based Hamiltonian simulation algorithm on the Rydberg platform to those of Hamiltonian simulation using product formulas [49,104]. In order to have a fair comparison for the disordered Heisenberg model, we consider the ordering structure of the product formula proposed by Ref. [104]. In particular, we focus on the types of Hamiltonians that can be written in the form

$$H = \sum_i^{n_{\rm site}-1} H_{i,i+1}, \tag{F6}$$

where the terms $H_{i,i+1}$ can be decomposed into Pauli operators which act nontrivially only on sites i and $i+1$. Then the first-order product formula has the form

$$\begin{aligned} e^{-iH\delta t} \approx \rho_1(\delta t) &= \prod_{k=1}^{n/2-1} e^{-i\delta t H_{2k,2k+1}} \prod_{l=1}^{n/2} e^{-i\delta t H_{2k-1,2k}} \\ &= e^{-i\delta t H_{\rm even}} e^{-i\delta t H_{\rm odd}}. \end{aligned} \tag{F7}$$

Moreover, the higher-order product formulas can be constructed as the following [104]:

$$\rho_2(\delta t) = e^{-i\frac{\delta t}{2}H_{\rm even}} e^{-i\delta t H_{\rm odd}} e^{-i\frac{\delta t}{2}H_{\rm even}}, \tag{F8}$$

$$\rho_{2k}(\delta t) = \rho_{2k-2}(p_k\delta t)^2 \rho_{2k-2}[(1-4p_k)\delta t]\rho_{2k-2}(p_k\delta t)^2, \tag{F9}$$

where $p_k = 1/4 - 4^{\frac{1}{2k-1}}$. In the following, we will only focus on the fourth-order product formula algorithm as it results in the best conventional gate counts in Ref. [49]. The errors induced by the fourth-order product formula approximation to the evolution operator $e^{-iH_{H1D}\delta t}$ scale as $O[n(\delta t)^5]$ for small δt [104]. In order to simulate larger times, one conducts the simulation in $r = t/\delta t$ segments. Reference [104] utilized a numerical optimization algorithm which determined that the number of segments r for an error threshold $\epsilon = 10^{-3}$ and fourth-order product formula

$$r_4 \approx 4n_{\text{site}}^{1.555}. \tag{F10}$$

In order to calculate the resource costs of implementing product formulas on the Rydberg atom platform, we consider the specific protocols proposed in Ref. [30]. This proposal is based on an implementation of the exponential of a Pauli term in the Hamiltonian (i.e., $e^{-i\alpha_j P_j}$) using a single ancilla a. In particular, the scheme uses the following gate sequence (with the ancilla initialized in the $|0_a\rangle$ state):

$$e^{-i\alpha_j P_j} = G^\dagger e^{i\alpha_j \sigma_z^a} G, \tag{F11}$$

where

$$G = e^{-i\pi/4\sigma_x^{(a)}} U_j e^{i\pi/4\sigma_x^{(a)}}, \tag{F12}$$

and $U_j = |1\rangle_a\langle 1| \otimes P_j + (\mathbf{I} - |0\rangle_a\langle 0|) \otimes \mathbf{I}$. Intuitively, the transformation G maps the eigenstates of the Pauli operator P_j with eigenvalues ± 1 onto the $|\frac{1\pm 1}{2}\rangle_{\text{anc}}$ states of the ancilla qubit. The two eigenstates acquire phases with opposite signs using the single-qubit phase rotation $e^{i\alpha_j\sigma_z^a}$. The implementation of G has the following EBGC:

$$n_G = \frac{1}{3}\left[2 + \frac{\text{supp}(P_j)}{2}\right], \tag{F13}$$

$$d_G = 4. \tag{F14}$$

We remind the reader that the ancilla is initialized in the $|0_a\rangle$ state. The exponentiation requires 1 ancilla per two-qubit Pauli operator and can be implemented in depth $8 + \alpha_j/\pi$. The EBGC of the exponentiation step is (see Table I)

$$\frac{1}{3}\left[2n_G + \frac{2\alpha_j}{\pi}\right]. \tag{F15}$$

Thus, the exponentiation of each two-qubit Pauli takes $2 + \alpha_j/(3\pi)$ error-bounded gates.

The resources needed for the simulation of the 1D disordered Heisenberg model using first-order product formula for a single segment [49] that implements a time evolution for δt can be calculated by assigning 3 two-qubit and 1 single-qubit Pauli terms to each site:

$$d_{1\text{PF}} = 2 * 3 * (8 + \delta t/\pi) + \delta t/\pi = 48 + 7\delta t/\pi,$$
$$n_{1\text{PF}} = n_{\text{site}}\left[3\left(2 + \frac{\delta t}{3\pi}\right) + \frac{\delta t}{3\pi}\right] = n_{\text{site}}\left(6 + \frac{4\delta t}{3\pi}\right),$$

where we note the factors of 2 in the calculation of d_{PF} arise from the serial application of evolution by H_{even} and H_{odd}, and we assume that the local random field can be implemented using 1 single-qubit rotation without any need for ancillas. Note that the number of two-qubit gates required to implement one iteration of the first-order product formula is $n_{\text{site}}(3 * 2 * 2) = n_{\text{site}} * 12$ if we require 2 two-qubit gates to implement U_j in Eq. (F12). Hence, using biased-error unitaries, the error probability is half the number of two-qubit gates.

Here, we compare the QSP-based Hamiltonian simulation to the fourth-order product formula according to Eq. (F9), as it results in the lowest gate counts in Ref. [49]. In our calculations, the EBGC of implementing the second-order product formula is 1.5 times that of implementing the first-order product formula. To calculate the resources for longer time evolution, the above expressions should be multiplied by r_4 in Eq. (F10).

[1] G. K. Brennen, C. M. Caves, P. S. Jessen, and I. H. Deutsch, Quantum logic gates in optical lattices, Phys. Rev. Lett. **82**, 1060 (1999).

[2] H.-J. Briegel, T. Calarco, D. Jaksch, J. I. Cirac, and P. Zoller, Quantum computing with neutral atoms, J. Mod. Opt. **47**, 415 (2000).

[3] D. Jaksch, J. I. Cirac, P. Zoller, S. L. Rolston, R. Côté, and M. D. Lukin, Fast quantum gates for neutral atoms, Phys. Rev. Lett. **85**, 2208 (2000).

[4] E. Brion, K. Mølmer, and M. Saffman, Quantum computing with collective ensembles of multilevel systems, Phys. Rev. Lett. **99**, 260501 (2007).

[5] K. Mølmer, L. Isenhower, and M. Saffman, Efficient grover search with rydberg blockade, J. Phys. B: At., Mol. Opt. Phys. **44**, 184016 (2011).

[6] M. Saffman, Quantum computing with atomic qubits and rydberg interactions: progress and challenges, J. Phys. B: At., Mol. Opt. Phys. **49**, 202001 (2016).

[7] D. S. Weiss and M. Saffman, Quantum computing with neutral atoms, Phys. Today **70**(7), 44 (2017).

[8] C. S. Adams, J. D. Pritchard, and J. P. Shaffer, Rydberg atom quantum technologies, J. Phys. B: At., Mol. Opt. Phys. **53**, 012002 (2019).

[9] L. Henriet, L. Beguin, A. Signoles, T. Lahaye, A. Browaeys, G.-O. Reymond, and C. Jurczak, Quantum computing with neutral atoms, Quantum **4**, 327 (2020).

[10] H. Bernien, S. Schwartz, A. Keesling, H. Levine, A. Omran, H. Pichler, S. Choi, A. S. Zibrov, M. Endres, M. Greiner *et al.*, Probing many-body dynamics on a 51-atom quantum simulator, Nature (London) **551**, 579 (2017).

[11] A. Browaeys and T. Lahaye, Many-body physics with individually controlled rydberg atoms, Nat. Phys. **16**, 132 (2020).

[12] A. Omran, H. Levine, A. Keesling, G. Semeghini, T. T. Wang, S. Ebadi, H. Bernien, A. S. Zibrov, H. Pichler, S. Choi *et al.*, Generation and manipulation of schrödinger cat states in rydberg atom arrays, Science **365**, 570 (2019).

[13] R. Samajdar, W. W. Ho, H. Pichler, M. D. Lukin, and S. Sachdev, Quantum phases of rydberg atoms on a kagome lattice, Proc. Natl. Acad. Sci. USA **118**, e2015785118 (2021).

[14] R. Verresen, M. D. Lukin, and A. Vishwanath, Prediction of toric code topological order from Rydberg blockade, Phys. Rev. X **11**, 031005 (2021).
[15] G. Semeghini, H. Levine, A. Keesling, S. Ebadi, T. T. Wang, D. Bluvstein, R. Verresen, H. Pichler, M. Kalinowski, R. Samajdar *et al.*, Probing topological spin liquids on a programmable quantum simulator, Science **374**, 1242 (2021).
[16] M. D. Lukin, S. F. Yelin, M. Fleischhauer, and M. O. Scully, Quantum interference effects induced by interacting dark resonances, Phys. Rev. A **60**, 3225 (1999).
[17] M. D. Lukin, S. F. Yelin, and M. Fleischhauer, Entanglement of atomic ensembles by trapping correlated photon states, Phys. Rev. Lett. **84**, 4232 (2000).
[18] M. Bajcsy, A. S. Zibrov, and M. D. Lukin, Stationary pulses of light in an atomic medium, Nature (London) **426**, 638 (2003).
[19] K. S. Choi, H. Deng, J. Laurat, and H. Kimble, Mapping photonic entanglement into and out of a quantum memory, Nature (London) **452**, 67 (2008).
[20] E. Urban, T. A. Johnson, T. Henage, L. Isenhower, D. Yavuz, T. Walker, and M. Saffman, Observation of rydberg blockade between two atoms, Nat. Phys. **5**, 110 (2009).
[21] M. D. Lukin, M. Fleischhauer, R. Cote, L. M. Duan, D. Jaksch, J. I. Cirac, and P. Zoller, Dipole blockade and quantum information processing in mesoscopic atomic ensembles, Phys. Rev. Lett. **87**, 037901 (2001).
[22] I. S. Madjarov, J. P. Covey, A. L. Shaw, J. Choi, A. Kale, A. Cooper, H. Pichler, V. Schkolnik, J. R. Williams, and M. Endres, High-fidelity entanglement and detection of alkaline-earth rydberg atoms, Nat. Phys. **16**, 857 (2020).
[23] J. T. Wilson, S. Saskin, Y. Meng, S. Ma, R. Dilip, A. P. Burgers, and J. D. Thompson, Trapping alkaline earth rydberg atoms optical tweezer arrays, Phys. Rev. Lett. **128**, 033201 (2022).
[24] S. Ma, A. P. Burgers, G. Liu, J. Wilson, B. Zhang, and J. D. Thompson, Universal gate operations on nuclear spin qubits in an optical tweezer array of ^{171}Yb atoms, Phys. Rev. X **12**, 021028 (2022).
[25] H. Haffner, C. F. Roos, and R. Blatt, Quantum computing with trapped ions, Phys. Rep. **469**, 155 (2008).
[26] J. P. Home, D. Hanneke, J. D. Jost, J. M. Amini, D. Leibfried, and D. J. Wineland, Complete methods set for scalable ion trap quantum information processing, Science **325**, 1227 (2009).
[27] A. Wallraff, D. I. Schuster, A. Blais, L. Frunzio, R.-S. Huang, J. Majer, S. Kumar, S. M. Girvin, and R. J. Schoelkopf, Strong coupling of a single photon to a superconducting qubit using circuit quantum electrodynamics, Nature (London) **431**, 162 (2004).
[28] A. Blais, A. L. Grimsmo, S. M. Girvin, and A. Wallraff, Circuit quantum electrodynamics, Rev. Mod. Phys. **93**, 025005 (2021).
[29] D. Bluvstein, H. Levine, G. Semeghini, T. T. Wang, S. Ebadi, M. Kalinowski, A. Keesling, N. Maskara, H. Pichler, M. Greiner *et al.*, A quantum processor based on coherent transport of entangled atom arrays, Nature (London) **604**, 451 (2022).
[30] H. Weimer, M. Müller, I. Lesanovsky, P. Zoller, and H. P. Büchler, A rydberg quantum simulator, Nat. Phys. **6**, 382 (2010).
[31] K. Barnes, P. Battaglino, B. J. Bloom, K. Cassella, R. Coxe, N. Crisosto, J. P. King, S. S. Kondov, K. Kotru, S. C. Larsen *et al.*, Assembly and coherent control of a register of nuclear spin qubits, Nat. Commun. **13**, 2779 (2022).
[32] I. Cong, H. Levine, A. Keesling, D. Bluvstein, S.-T. Wang, and M. D. Lukin, Hardware-efficient, fault-tolerant quantum computation with rydberg atoms, Phys. Rev. X **12**, 021049 (2022).
[33] Y. Zhou, E. M. Stoudenmire, and X. Waintal, What limits the simulation of quantum computers?, Phys. Rev. X **10**, 041038 (2020).
[34] C. Oh, K. Noh, B. Fefferman, and L. Jiang, Classical simulation of lossy boson sampling using matrix product operators, Phys. Rev. A **104**, 022407 (2021).
[35] F. Pan, K. Chen, and P. Zhang, Solving the sampling problem of the sycamore quantum circuits, Phys. Rev. Lett. **129**, 090502 (2022).
[36] D. Aharonov and M. Ben-Or, Fault-tolerant quantum computation with constant error, in *Proceedings of the Twenty-Ninth Annual ACM Symposium on Theory of Computing* (ACM, New York, 1997), pp. 176–188.
[37] J. Preskill, Reliable quantum computers, Proc. R. Soc. London A **454**, 385 (1998).
[38] E. Knill, Quantum computing with realistically noisy devices, Nature (London) **434**, 39 (2005).
[39] M. A. Nielsen and I. Chuang, *Quantum Computation and Quantum Information* (American Association of Physics Teachers, College Park, MD, 2002).
[40] D. Daems, A. Ruschhaupt, D. Sugny, and S. Guerin, Robust quantum control by a single-shot shaped pulse, Phys. Rev. Lett. **111**, 050404 (2013).
[41] A. R. R. Carvalho, H. Ball, M. J. Biercuk, M. R. Hush, and F. Thomsen, Error-robust quantum logic optimization using a cloud quantum computer interface, Phys. Rev. Appl. **15**, 064054 (2021).
[42] Y. Baum, M. Amico, S. Howell, M. Hush, M. Liuzzi, P. Mundada, T. Merkh, A. R. Carvalho, and M. J. Biercuk, Experimental deep reinforcement learning for error-robust gate-set design on a superconducting quantum computer, PRX Quantum **2**, 040324 (2021).
[43] D. Aharonov, A. Kitaev, and N. Nisan, Quantum circuits with mixed states, in *Proceedings of the Thirtieth Annual ACM Symposium on Theory of Computing* (ACM, New York, 1998), pp. 20–30.
[44] A. Gilchrist, N. K. Langford, and M. A. Nielsen, Distance measures to compare real and ideal quantum processes, Phys. Rev. A **71**, 062310 (2005).
[45] G. H. Low, Quantum signal processing by single-qubit dynamics, Ph.D. thesis, Massachusetts Institute of Technology, 2017.
[46] A. Gilyén, Y. Su, G. H. Low, and N. Wiebe, Quantum singular value transformation and beyond: exponential improvements for quantum matrix arithmetics, in *Proceedings of the 51st Annual ACM SIGACT Symposium on Theory of Computing* (ACM, New York, 2019), pp. 193–204.
[47] J. M. Martyn, Z. M. Rossi, A. K. Tan, and I. L. Chuang, Grand unification of quantum algorithms, PRX Quantum **2**, 040203 (2021).
[48] H. Levine, A. Keesling, G. Semeghini, A. Omran, T. T. Wang, S. Ebadi, H. Bernien, M. Greiner, V. Vuletić, H. Pichler, and M. D. Lukin, Parallel implementation of high-fidelity multiqubit gates with neutral atoms, Phys. Rev. Lett. **123**, 170503 (2019).

[49] A. M. Childs, D. Maslov, Y. Nam, N. J. Ross, and Y. Su, Toward the first quantum simulation with quantum speedup, Proc. Natl. Acad. Sci. USA **115**, 9456 (2018).

[50] J. Haah, M. B. Hastings, R. Kothari, and G. H. Low, Quantum algorithm for simulating real time evolution of lattice Hamiltonians, SIAM J. Comput. FOCS18 (2021).

[51] M. Saffman and T. G. Walker, Analysis of a quantum logic device based on dipole-dipole interactions of optically trapped rydberg atoms, Phys. Rev. A **72**, 022347 (2005).

[52] X. L. Zhang, A. T. Gill, L. Isenhower, T. G. Walker, and M. Saffman, Fidelity of a Rydberg-blockade quantum gate from simulated quantum process tomography, Phys. Rev. A **85**, 042310 (2012).

[53] A. M. Childs and N. Wiebe, Hamiltonian simulation using linear combinations of unitary operations, Quantum Inf. Comput. **12**, 901 (2012).

[54] S. Chakraborty, A. Gilyén, and S. Jeffery, The power of Block-Encoded matrix powers: Improved regression techniques via faster Hamiltonian simulation, in *46th International Colloquium on Automata, Languages, and Programming (ICALP 2019)*, Leibniz International Proceedings in Informatics (LIPIcs), Vol. 132, edited by C. Baier, I. Chatzigiannakis, P. Flocchini, and S. Leonardi (Schloss Dagstuhl–Leibniz-Zentrum fuer Informatik, Dagstuhl, Germany, 2019), pp. 33:1–33:14.

[55] S. Lloyd, Universal quantum simulators, Science **273**, 1073 (1996).

[56] A. W. Harrow, A. Hassidim, and S. Lloyd, Quantum algorithm for linear systems of equations, Phys. Rev. Lett. **103**, 150502 (2009).

[57] K. R. Brown, A. W. Harrow, and I. L. Chuang, Arbitrarily accurate composite pulse sequences, Phys. Rev. A **70**, 052318 (2004).

[58] G. H. Low and I. L. Chuang, Hamiltonian simulation by qubitization, Quantum **3**, 163 (2019).

[59] Y. Dong, X. Meng, K. B. Whaley, and L. Lin, Efficient phase-factor evaluation in quantum signal processing, Phys. Rev. A **103**, 042419 (2021).

[60] M. Müller, I. Lesanovsky, H. Weimer, H. P. Büchler, and P. Zoller, Mesoscopic rydberg gate based on electromagnetically induced transparency, Phys. Rev. Lett. **102**, 170502 (2009).

[61] K.-J. Boller, A. Imamoğlu, and S. E. Harris, Observation of electromagnetically induced transparency, Phys. Rev. Lett. **66**, 2593 (1991).

[62] M. D. Lukin and A. Imamoğlu, Nonlinear optics and quantum entanglement of ultraslow single photons, Phys. Rev. Lett. **84**, 1419 (2000).

[63] S. P. Jordan, K. S. M. Lee, and J. Preskill, Quantum algorithms for quantum field theories, Science **336**, 1130 (2012).

[64] K. Temme, S. Bravyi, and J. M. Gambetta, Error mitigation for short-depth quantum circuits, Phys. Rev. Lett. **119**, 180509 (2017).

[65] C. Brif, R. Chakrabarti, and H. Rabitz, Control of quantum phenomena: past, present and future, New J. Phys. **12**, 075008 (2010).

[66] S. J. Glaser, U. Boscain, T. Calarco, C. P. Koch, W. Köckenberger, R. Kosloff, I. Kuprov, B. Luy, S. Schirmer, T. Schulte-Herbrüggen *et al.*, Training schrödingers cat: Quantum optimal control: Strategic report on current status, visions and goals for research in europe, Eur. Phys. J. D **69**, 279 (2015).

[67] F. Motzoi, J. M. Gambetta, P. Rebentrost, and F. K. Wilhelm, Simple pulses for elimination of leakage in weakly nonlinear qubits, Phys. Rev. Lett. **103**, 110501 (2009).

[68] P. Zanardi, Symmetrizing evolutions, Phys. Lett. A **258**, 77 (1999).

[69] L. Viola, E. Knill, and S. Lloyd, Dynamical decoupling of open quantum systems, Phys. Rev. Lett. **82**, 2417 (1999).

[70] K. Khodjasteh and D. A. Lidar, Fault-tolerant quantum dynamical decoupling, Phys. Rev. Lett. **95**, 180501 (2005).

[71] V. Giovannetti, S. Lloyd, and L. Maccone, Quantum random access memory, Phys. Rev. Lett. **100**, 160501 (2008).

[72] V. Giovannetti, S. Lloyd, and L. Maccone, Architectures for a quantum random access memory, Phys. Rev. A **78**, 052310 (2008).

[73] C. T. Hann, G. Lee, S. M. Girvin, and L. Jiang, Resilience of quantum random access memory to generic noise, PRX Quantum **2**, 020311 (2021).

[74] A. M. Childs, Lecture notes on quantum algorithms, Lecture notes at University of Maryland, 2017 (unpublished).

[75] J. J. Sakurai and E. D. Commins, *Modern Quantum Mechanics*, revised edition (Addison Wesley, Boston, 1995).

[76] D. A. Steck, Lecture notes "Quantum and atom optics" (unpublished).

[77] J. Dalibard, Y. Castin, and K. Mølmer, Wave-function approach to dissipative processes in quantum optics, Phys. Rev. Lett. **68**, 580 (1992).

[78] S. Reynaud, E. Giacobino, and J. Zinn-Justin, *Quantum Fluctuations*, Volume 63 of École d'Été de Physique Théorique Les Houches: Session (Elsevier Science, 1997).

[79] P. Rebentrost, M. Mohseni, and S. Lloyd, Quantum support vector machine for big data classification, Phys. Rev. Lett. **113**, 130503 (2014).

[80] A. Prakash, *Quantum Algorithms for Linear Algebra and Machine Learning* (University of California Press, Berkeley, 2014).

[81] R. Löw, H. Weimer, J. Nipper, J. B. Balewski, B. Butscher, H. P. Büchler, and T. Pfau, An experimental and theoretical guide to strongly interacting rydberg gases, J. Phys. B: At., Mol. Opt. Phys. **45**, 113001 (2012).

[82] M. Morgado and S. Whitlock, Quantum simulation and computing with rydberg-interacting qubits, AVS Quantum Science **3**, 023501 (2021).

[83] N. Šibalić, J. D. Pritchard, C. S. Adams, and K. J. Weatherill, Arc: An open-source library for calculating properties of alkali rydberg atoms, Comput. Phys. Commun. **220**, 319 (2017).

[84] S. Ravets, H. Labuhn, D. Barredo, L. Béguin, T. Lahaye, and A. Browaeys, Coherent dipole–dipole coupling between two single rydberg atoms at an electrically-tuned förster resonance, Nat. Phys. **10**, 914 (2014).

[85] D. D. Yavuz, P. B. Kulatunga, E. Urban, T. A. Johnson, N. Proite, T. Henage, T. G. Walker, and M. Saffman, Fast ground state manipulation of neutral atoms in microscopic optical traps, Phys. Rev. Lett. **96**, 063001 (2006).

[86] M. Saffman, T. G. Walker, and K. Mølmer, Quantum information with rydberg atoms, Rev. Mod. Phys. **82**, 2313 (2010).

[87] Y. O. Dudin, L. Li, and A. Kuzmich, Light storage on the time scale of a minute, Phys. Rev. A **87**, 031801 (2013).

[88] J. Ye, H. Kimble, and H. Katori, Quantum state engineering and precision metrology using state-insensitive light traps, Science **320**, 1734 (2008).

[89] M. Archimi, C. Simonelli, L. Di Virgilio, A. Greco, M. Ceccanti, E. Arimondo, D. Ciampini, I. I. Ryabtsev, I. I. Beterov, and O. Morsch, Measurements of single-state and state-ensemble lifetimes of high-lying rb rydberg levels, Phys. Rev. A **100**, 030501(R) (2019).

[90] D. Petrosyan, F. Motzoi, M. Saffman, and K. Mølmer, High-fidelity rydberg quantum gate via a two-atom dark state, Phys. Rev. A **96**, 042306 (2017).

[91] J. D. Thompson, T. G. Tiecke, A. S. Zibrov, V. Vuletić, and M. D. Lukin, Coherence and raman sideband cooling of a single atom in an optical tweezer, Phys. Rev. Lett. **110**, 133001 (2013).

[92] A. M. Kaufman, B. J. Lester, and C. A. Regal, Cooling a single atom in an optical tweezer to its quantum ground state, Phys. Rev. X **2**, 041014 (2012).

[93] Y. Chew, T. Tomita, T. P. Mahesh, S. Sugawa, S. de Léséleuc, and K. Ohmori, Ultrafast energy exchange between two single rydberg atoms on a nanosecond timescale, Nat. Photonics **16**, 724 (2022).

[94] J. T. Young, P. Bienias, R. Belyansky, A. M. Kaufman, and A. V. Gorshkov, Asymmetric blockade and multi-qubit gates via dipole-dipole interactions, Phys. Rev. Lett. **127**, 120501 (2021).

[95] P. Meystre and M. Sargent, *Elements of Quantum Optics* (Springer, Berlin, 2007).

[96] K. McDonnell, L. F. Keary, and J. D. Pritchard, Demonstration of a quantum gate using electromagnetically induced transparency, Phys. Rev. Lett. **129**, 200501 (2022).

[97] L. Isenhower, M. Saffman, and K. Mølmer, Multibit C_k NOT quantum gates via Rydberg blockade, Quantum Inf. Proc. **10**, 755 (2011).

[98] R. G. Unanyan and M. Fleischhauer, Efficient and robust entanglement generation in a many-particle system with resonant dipole-dipole interactions, Phys. Rev. A **66**, 032109 (2002).

[99] M. Saffman and K. Mølmer, Efficient multiparticle entanglement via asymmetric Rydberg blockade, Phys. Rev. Lett. **102**, 240502 (2009).

[100] M. Ebert, M. Kwon, T. G. Walker, and M. Saffman, Coherence and Rydberg blockade of atomic ensemble qubits, Phys. Rev. Lett. **115**, 093601 (2015).

[101] J. Zeiher, P. Schauß, S. Hild, T. Macrì, I. Bloch, and C. Gross, Microscopic characterization of scalable coherent Rydberg superatoms, Phys. Rev. X **5**, 031015 (2015).

[102] G. James, D. Witten, T. Hastie, and R. Tibshirani, *An Introduction to Statistical Learning*, Vol. 112 (Springer, Berlin, 2013).

[103] M. Suzuki, General theory of fractal path integrals with applications to many-body theories and statistical physics, J. Math. Phys. **32**, 400 (1991).

[104] A. M. Childs and Y. Su, Nearly optimal lattice simulation by product formulas, Phys. Rev. Lett. **123**, 050503 (2019).

[105] J. C. Aulicino, T. Keen, and B. Peng, State preparation and evolution in quantum computing: A perspective from hamiltonian moments, Int. J. Quantum Chem. **122**, e26853 (2022).

[106] Y. Kim, A. Eddins, S. Anand, K. X. Wei, E. Van Den Berg, S. Rosenblatt, H. Nayfeh, Y. Wu, M. Zaletel, K. Temme *et al.*, Evidence for the utility of quantum computing before fault tolerance, Nature (London) **618**, 500 (2023).

[107] H.-P. Breuer and F. Petruccione, *The Theory of Open Quantum Systems* (Oxford University Press, New York, 2002).

[108] M. V. Berry, Quantal phase factors accompanying adiabatic changes, Proc. R. Soc. London A **392**, 45 (1984).

[109] M. H. S. Amin, Consistency of the adiabatic theorem, Phys. Rev. Lett. **102**, 220401 (2009).

[110] G. H. Low, T. J. Yoder, and I. L. Chuang, Methodology of resonant equiangular composite quantum gates, Phys. Rev. X **6**, 041067 (2016).

[111] E. H. Lieb and D. W. Robinson, The finite group velocity of quantum spin systems, in *Statistical Mechanics* (Springer, Berlin, 1972), pp. 425–431.

[112] M. B. Hastings, Locality in quantum systems, Quantum Theory Small, Large Scales **95**, 171 (2010).